THE UNIVERSITY OF QUEENSLAND
AUSTRALIA

Design, Construction, and Performance
towards
A Versatile ^{87}Rb & ^{41}K BEC Apparatus

Nicholas McKay Parry
BSc (Hons)

A thesis submitted for the degree of Master of Philosophy at
The University of Queensland in 2015.
School of Mathematics and Physics
ARC Centre of Excellence for Engineered Quantum Systems

Abstract

The possibility to mould and control pure quantum systems has been offered by the experimental observation of Bose-Einstein condensation, a unique phase of matter when macroscopic quantities of a gas occupy the lowest quantum state. Techniques for creating these degenerate gases vary from laboratory to laboratory; each offers an unique test bed for studying quantum physics on a macroscopic scale. This thesis reports on the experimental design, construction and performance of an apparatus to create two-component ^{87}Rb and ^{41}K condensates for studies of non-equilibrium dynamics.

This thesis is broken down as follows. In Chapter 1, a brief overview of the history and status of Bose Einstein condensates is presented, to affirm the motivation behind our work. Chapter 2 then presents the fundamental theory and background information to understand how and why our experiment was built.

Chapter 3 describes the bulk of the work undertaken at the beginning of this thesis. In particular it describes the design choices, construction and performance of the vacuum, and laser and magnetic coil systems that are the key structural elements of the apparatus. In particular the vacuum system is a two-component differentially pumped system designed to optimise the number and lifetime of trapped atoms. Another integral element of the vacuum chamber is the science cell that enables high optical access, and close physical, access to an atomic cloud. As a result, high resolution imaging, $\simeq$ 980 nm resolution at 780 nm is expected with a commercial microscope objective lens. The laser system is carefully designed to best combine and deliver the seven different optical frequencies required to simultaneously trap and manipulate ^{87}Rb and ^{41}K atoms. The magnetic coil system also represents an integral component of the apparatus, responsible for trapping and transferring atoms in a quadrupole field. One pair of coils is able to have their current direction reversed in order to generate bias fields. This allows access to Feshbach resonances between the two species, once they have been condensed.

The second part of this thesis, Chapter 4, describes the performance of the apparatus when used to simultaneously trap ^{41}K and ^{87}Rb in the 3D magneto-optical trap (MOT) and produce a condensate of ^{87}Rb atoms. In particular 1×10^9 rubidium atoms are routinely trapped in the 3D-MOT and transferred to the science chamber. In the hybrid trap the atoms are evaporatively cooled via microwave radiation, later to be used to sympathetically cool ^{41}K, and loaded into a hybrid optical dipole and magnetic trap. At this stage $\simeq 5 \times 10^6$ atoms are evaporatively cooled, by lowering the trap depth of the optical dipole beam, until a condensate of ^{87}Rb is formed, containing 1.5×10^5 atoms. Additionally we are able to produce 3D MOTs of ^{41}K simultaneously with the ^{87}Rb 3D MOTs.

Declaration by author

This thesis is composed of my original work, and contains no material previously published or written by another person except where due reference has been made in the text. I have clearly stated the contribution by others to jointly-authored works that I have included in my thesis.

I have clearly stated the contribution of others to my thesis as a whole, including statistical assistance, survey design, data analysis, significant technical procedures, professional editorial advice, and any other original research work used or reported in my thesis. The content of my thesis is the result of work I have carried out since the commencement of my research higher degree candidature and does not include a substantial part of work that has been submitted to qualify for the award of any other degree or diploma in any university or other tertiary institution. I have clearly stated which parts of my thesis, if any, have been submitted to qualify for another award.

I acknowledge that an electronic copy of my thesis must be lodged with the University Library and, subject to the policy and procedures of The University of Queensland, thesis be made available for research and study in accordance with the Copyright Act 1968 unless a period of embargo has been approved by the Dean of the Graduate School.

I acknowledge that copyright of all material contained in my thesis resides with the copyright holder(s) of that material. Where appropriate I have obtained copyright permission from the copyright holder to reproduce material in this thesis.

Publications during candidature

Parry, N. M., Baker, M., Neely, T., Carey, T., Bell, T., & Rubinsztein-Dunlop, H. (2014). Note: High turn density magnetic coils with improved low pressure water cooling for use in atom optics. *Review of Scientific Instruments*, 85(8), 086103.

Publications included in this thesis

No publications included.

Contributions by others to this thesis

Dr. Tyler Neely contributed significantly to conception and key design elements of the experiment. Mr. Isaac Lenton contributed significantly with the design and testing of DMD and high-resolution imaging system. Mr. Tom Carey significant contributions are a variety of electronic control boxes used on the system.

Statement of parts of thesis submitted to qualify for the award of another degree

None.

Acknowledgements

I am very grateful for the opportunities and support of many people during my time at UQ. I would like to thank my supervisory duo, Dr. Tyler Neely and Prof. Halina Rubinsztein-Dunlop. Tyler has been an exceptional supervisor, making sure the experiment was on track. Similarly, despite her busy schedule, Halina was always willing to help and provide advice.

Additionally, I am grateful for the other experimentalists in the laboratory. Tom Carey, for doing all the electrical projects that I didn't, Isaac Lenton for being the whizz kid. Similarly, I would like to thank the guys on the other side of the lab, Dr. Mark Baker, Tom Bell and Jake Glidden for continual advice and discussion. Also a special appreciation goes out to the guys in the workshop.

Further appreciation goes to theoretical crew at UQ. Dr. Stuart Szigeti, Dr. Simon Haine, Jim Mills and Dr. Robert Lewis-Swan amongst the others I've missed.

Lastly the admin staff including Danette Peachy, Jo Hughes, Emma Linnell, Angela White, and Ruth Forest were amazing at chasing up my paperwork and forms. I would also like to sincerely thank Murray Kane, while we didn't interact much; his sheer willingness to listen and help was appreciated.

Lastly I would like to thank my partner, Britney Thompson, for her continued support throughout.

Keywords

Bose-Einstein condensate, Potassium, Rubidium, DMD, dual species, differential pumping, Feshbach resonance.

Australian and New Zealand Standard Research Classifications (ANZSRC)

ANZSRC code: 020601, Degenerate Quantum Gases and Atom Optics

Fields of Research (FOR) Classification

FoR code: 0206, Quantum Physics, 100%

Contents

Chapter 1

Introduction

The distinction between bosons and fermions requires little retelling. Fermions, particles with half-integer spin, are prohibited from occupying the same quantum state simultaneously. Bosons, which have integer spin, are freely able to occupy the same ground state. Here we are particularly interested, experimentally, of what occurs when a bosonic ensemble's constituents begin to occupy the same ground state of a confining potential. As atoms begging to accumulate in this state, the system will undergo a phase transition as the wave-like nature, of matter, begins to dominate. This accumulation of particles in the ground state is known as a Bose-Einstein condensate (BEC). Bose-Einstein condensation was proposed as an explanation for the properties of Superfluid ^{4}He [1, 2], and has now been observed in diverse systems including micro cavity polaritons [3]. The most striking and relevant example of these phenomena, is the ability to observe the transition directly as a group of atomic bosons transition to a Bose Einstein condensate.

The concept of a Bose-Einstein condensate emerged from Einstein's foundational theories of photon statistics in combinations with de Broglie's conjecture that particles also possess a wave nature. A consequence of these statistics is that at very low temperatures an atomic gas of bosons will begin to have a large portion of atoms reside in the lowest energy quantum state. For a single particle they are expected to exhibit quantum dynamics once their kinetic energy is less than the spacing between energy levels in a harmonic trap, $\mathrm{k}_B T < \hbar\omega_{ho}$, while a sample of N bosons has a significant fraction of particles in the ground state when $\mathrm{k}_B T < N^{1/3}\hbar\omega_{ho}$. As a result, a macroscopic number of particles can exhibit quantum behaviour. This property forms the basis of the allure and celebration of BECs. The first experimental observation of Bose-Einstein condensation, in 1995 [4, 5], has allowed experimentalists since to observe and study quantum phenomena on a macroscopic scale. The significance of this achievement is encapsulated in 2001 by the awarding of the Nobel Prize in Physics [6, 7].

This present potential and ability of BEC experiments, has been brought about by the progress made in exploiting the quantum nature of a Bose-Einstein condensate and building upon the history of experimental techniques. Seminal examples of early BEC research, which form the backbone of modern experiments, are the demonstration of interference between two condensates [8], investigations into long-range phase coherence [9], and observation of quantised vortices [10].

One application of the phase coherence of BECs is matter-wave interferometry, the measuring of phase shifts using the interference of two or more waves, has long been a technique of central importance in physics. Such techniques have enabled some of the most precise measurement devices known. With the development of quantum mechanics it was shortly realised that the wave-like nature of particles could provide sensitivity and precision well below the standard classical limit. BECs represent a strong basis for measuring quantities via interferometry such as acceleration, rotation, frequency, and gravity [11, 12, 13, 14]. A recent example of using the interfering properties of matter waves, used approximately 30 BECs, comprising of 300 to 600 ^{87}Rb atoms each, and made use of atomic squeezing to demonstrate quantum enhanced magnetometry down to 310(47) pT [15]. Using similar techniques it is expected that these systems may be used to reach down to Heisenberg limit [16]. The progress in moving from the general observation of matter wave interference to the precision measurements is a direct consequence of improvements in instrumentation and control afforded to experimentalists.

Instrumentation improvements in ultra cold atom experiments are well encapsulated through descriptions of recent atomic lattice experiments. Creating an optical lattice (alternating bright and dark regions of an optical field) has recently come to the forefront as a confining potential for quantum emulation of many-body systems [17]. In particular the observation of a superfluid, where the atomic ensemble acts as a single coherent matter wave permeating the entire lattice, to a Mott insulator, where each lattice site has a discrete number of atoms per site, has enabled enhanced studies into quantum dynamics on the macroscopic scale while observing individual particles. These systems offer wealth of control, which is well poised for studying and emulating a variety of many-body systems [17]. State of the art experiments have adapted high resolution absorption and fluorescence imaging system into BEC experiments, enabling high-precision and in-situ knowledge of atom number distributions throughout the lattice [18, 19]. The absorption scheme of the Oberthaler lab [20] has demonstrated a resolution down to 3.7 atoms, while fluorescence schemes have been shown to resolve single atoms [21]. Experimentally, this has enabled the emulation of a host of 'solvable' systems, representing the first steps towards emulation of more complex systems. In particular recent experiments have observed the quantum dynamics of a mobile spin impurity [22] before subsequently expanding towards the emulation of magnon bound state dynamics [23]. The latter experiment maps the Hamiltonian of a one-dimensional array of bosonic atoms to that of ferromagnetic spin-1/2 Heisenberg chain in order to observe two magnon bound states. Such states were predicted to exist in one-dimensional quantum magnets some 80 years ago [24]. Similar experiments include the simulation of antiferromagnetic spin chains [25] and direct measurement of two-site correlation functions of electron-hole pairs [26].

The technical progress of these systems thus facilitates applications to a wealth of processes that have intersection and overlap between many different research fields, ranging from quantum optics to solid-state physics [17]. Examples include the use of degenerate gases to connect neutral atom condensates to the quantum Hall effect [27, 28]. Similarly, the sub-field of atomtronics has emerged for the creation of new quantum devices [29, 30, 31]. Investigations into one-dimensional quantum system and the role of quantum fluctuations [32, 33], Hubbard and spin models, which are 'reasonable representations' of real system may be perfectly modelled with ultra cold atoms [34, 35], disordered systems and localisation [36], and superchemistry to study chemical reactions in a controlled way [37] are all examples of research areas ultra cold atoms intersect.

This list is by no means exhaustive, but aids in illustrating the breadth and depth degenerate ultra-cold gases afford to physicists. More recently, degenerate quantum gases have shown promise as a system that can be easily driven out of equilibrium, and thus have emerged as a promising system for the study of non-equilibrium dynamics in a closed quantum system.

1.1 Non-Equilibrium Dynamics and Ultra-cold Gases

The motivation behind using degenerate gases for the study of non-equilibrium dynamics is presented in this (non-exhaustive) overview of recent relevant experiments. Here we attempt to demonstrate how the intrinsic properties of a Bose-Einstein condensate, as well as advances in experimental tools and techniques, provide a well suited test-bed for studying non-equilibrium dynamics in a closed interacting quantum system, motivating the apparatus constructed during the time of this thesis.

Typically, equilibrium systems may often be understood using combinations of mean-field theory, renormalisation groups, and universality allowing an understanding of a great deal of rather complex many-body system from simple models. As a system moves away from equilibrium the situation becomes clouded, and it remains unclear whether simplified models accurately describe experiments of more complex systems [38]. In addition, tools to study these systems have been few and far between. More recently, the increasing amount of control afforded by ultra cold atomic gas experiments, has provided a landscape well suited for studies of systems away from equilibrium. In general, non-equilibrium dynamics is a pressing and important area of research due to the broad scope of the field. These include open problems in cosmology [39, 40] and condensed matter [17, 41]. As there are many ways to move a system away from equilibrium, such as applying a small driving field, or pumping energy or particles through reservoirs in transport problems, we focus here on a simplified system. As such we limit the scope to closed interacting quantum systems following sudden parameter quenches. A quench refers to a non-adiabatic change to the system parameters, particular interesting when observing what occurs when quenching a system through phase transition.

As mentioned, a key challenge in studying non-equilibrium systems is the limited number of test beds available in which their dynamical evolution is feasibly observable, while having sufficient tuneability. In order to satisfy these requirements any experiment should be well isolated (closed) while being physically accessible to interact with. Generally speaking, a pre-requisite in creating robust and reliable ultra cold atomic gases is a high degree of isolation, the vacuum chamber, from external influences. Accessibility, for control and observation, is generally determined by the design of the vacuum apparatus and other elements of infrastructure required. Similarly external infrastructure determines the confining potential of an atomic cloud, which may be generated by either, or a combination of, magnetic and optical fields [42, 43]. Historically, early experiments were resigned to rather simple harmonic trapping potentials. Today much more exotic and arbitrary trapping schemes have been developed. Movement towards homogenous, in terms of density, systems in two and three-dimensional boxes and ring traps [44, 45, 46] have become prevalent. In particular the homogenous cylindrical system of 2×10^5 ^{87}Rb atoms of the Hadzibabic group, Fig 1.1.1 (left), has gained particular attention for exploring a variety of systems including an analogue of an unstable vacuum to emulate the early universe [47]. The homogeneity is somewhat unique in ultra cold atoms, which are normally harmonically confined, linking more readily to models and systems that are not.

Trapping potentials are further tailorable, using micro-fabricated atom-chips [48], or through the use of interfering laser beams to create optical lattice. Such techniques continue to demon-

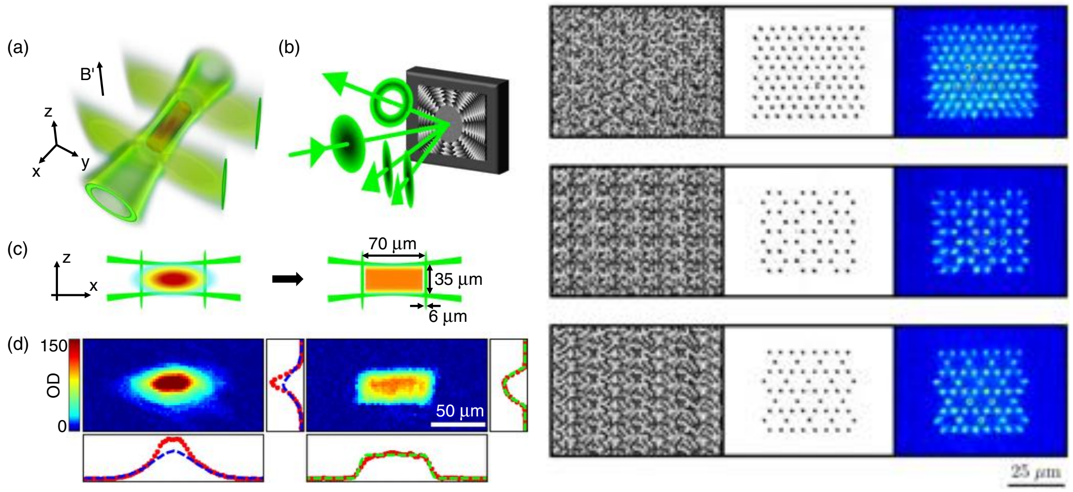

Figure 1.1.1: (left) Cylindrical box trap used for creating homogenous condensates. (a) The optical box trap formed from one hollow and two sheet beams created from a single SLM (b). (c) and (d) show the cloud distribution just before loading into the box trap and after, taken from [46]. (Right) Variety of 2D lattice potentials created from an SLM and loaded with atoms in the third box, taken from [55]

strate a great variety of different structures and dimensionality [49, 50, 51, 52, 53]. In particular, these references demonstrate the use of triangular, hexagonal, superlattice, and Kagomé lattice types. Systems with reduced dimensionality are also gaining traction, with improvements in spatial light modulator technology enabling arbitrary confining potentials to be made [54]. The ability of spatial light modulators is well demonstrated in [55] where arbitrary two-dimensional arrays of micro traps were created to trap single ^{87}Rb atoms as shown in Fig, 1.1.1 (right).

In short, the technical advances in trapping potentials enable an almost limitless supply and variety of confining potentials yielding a great deal of control over the environment atoms may reside within. Further, these elements may be dynamic and used to move a system from equilibrium as required.

In addition, to control the trapping potential landscape, it is important to be able to observe the dynamical evolution of a system following a quench. Generally, this refers to the ability to observe the relevant energy scales of temperature, kinetic and/or interaction energy that are of the order of milliseconds [56], much shorter than the average lifetime and coherence of the condensate, lasting many seconds. As such it is possible to follow the intrinsic quantum dynamics of ultra cold gases for very long timescales. An example of this is the seminal work conducted by Greiner et al. [57] that followed the unitary evolution of a quantum many-body system. This was

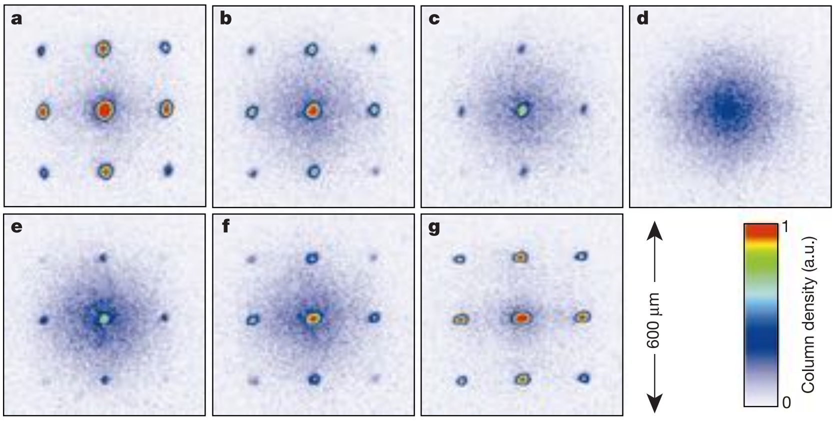

Figure 1.1.2: Dynamical evolution of rephasing dynamics as an atomic cloud of ^{87}Rb is quenched across the superfluid to Mott insulator transition and lattice depth brought down. These continue to oscillate in and out of phase with time as the matter wave evolves image from [57]

done by looking at coherence reconstruction following a quench of atoms confined to an optical lattice. In particular a ^{87}Rb degenerate ensemble was removed from equilibrium (superfluid regime) by quenching the depth of the lattice potential towards the Mott insulator regime. As the depth was subsequently dropped the rephasing dynamics were observed, and the extent to which coherence was restored across the cloud observed for different quench times, Fig. 1.1.2. Similar experiments by Weiler et al. [58] and Lamporesi et al. [59] monitored the formation of defects as ^{87}Rb atoms were quenched across the Bose Einstein condensate transition. They studied this with different transition rates revealing the formation of defects that would alter with different speeds. Non-equilibrium dynamics are also known to persist when observing long-lived pre-thermalisation states on integrable systems. Kinoshita et al. [33] showed this with a 1D out-of-equilibrium ^{87}Rb gas. After being hit with an optical phase grating, momenta space oscillations occurred (similar to an idealised Newton's cradle) and did not equilibrate, even after thousands of elastic collisions between the particles.

One of the most significant elements of modern BEC experiments is the adaptation of high resolution imaging into cold atom experiments. The complexity of these experiments has increased from looking at generalised atom tunnelling dynamics [21] to observation of spin correlation decay in an emulation of ferromagnetic Heisenberg quantum magnets far from equilibrium [60]. The work of Cheneau et al. used high resolution imaging to observe the finite velocity of propagating correlations in a 1D array of cold atoms as the system was quenched [61]. This study was related to investigating Lieb-Robinson bounds, finite spreading of correlations in a finite many-body system, which have been well studied theoretically but not observed directly [61].

More recently, work undertaken by Braun et al. (in the same research group) has explored how a system moves across the Mott-Insulator transition, rather than the consequences after the fact [62]. These dynamics pose one of the more challenging aspects of many body physics. Here they studied the emergence of coherence when crossing the superfluid Mott insulator regime. First they compared the experimental results, of the quench of one-dimensional arrays of ultra-cold ^{39}K atoms (spaced 736 nm) apart to that predicted by theory. In doing so they found remarkable agreement, indicating that system could be used to explore similar quench dynamics on domains, which cannot efficiently be simulated. The dynamics of the quench were then studied for higher dimensional lattices (2D and 3D) where no classical simulations are available. Further, universality is not observed in the coherence length under certain conditions. This is a remarkable study that demonstrates how 'ideal' an experimental landscape the ultra cold atom systems can be. This is particularly demonstrated by the ability to study dynamics away from equilibrium even when simulations are not available.

Additional freedom and control, in ultra cold atoms, is afforded with the existence of internal atomic states. Depending on what is required, these may be controllable using (in combination or alone) optical, microwave, radio-frequency or magnetic fields. Additionally, by varying how strongly particles interact, their temperature, density or trap dimensionality may control motional degrees of freedom. Of particular significance is the ability to tune interaction strength between atoms, using what is known as a Feshbach resonance [63], discussed in detail in section 2.7. Generally this resonance can be used to tune interactions from being positive (repulsive) to negative (attractive). Switching of magnetic fields is often on the order of 100 μs, faster than the cloud can track, meaning Feshbach resonances may be quenched across for interesting studies. For example, the work done by Hung et al placed 2×10^4 ^{133}Cs atoms into a two-dimensional 'pancake trap'. By quickly altering the scattering interaction strength, the emergence of density fluctuations and movement towards homogenous, or smooth, density distributions were observed. Other examples of using Feshbach resonances are the dynamics of a one-dimensional Ising spin chain [64], superheating [65] and atom interferometry experiments [66].

In summary, technical and analytical innovations, for use in ultra-cold atom experiments, have provided a strong experimental landscape for the study of non-equilibrium dynamics in closed, interacting many-body quantum systems. In particular, the ability to create configurable trapping potentials of almost any size, shape, dimensionality, and strength, and the inherent isolation and time-scales of ultra cold atom experiments make them well suited for these studies.

Another layer of complexity, control, and opportunity is afforded to experimentalists when more then one atomic species is added to the mix. This is the basis of the work contained within this thesis. More precisely, we set out to construct an apparatus with similar capabilities to the state of the art systems, while introducing a second atomic species for an enhanced parameter space.

1.2 Motivation

As mentioned, when an atomic ensemble contains more then one type of atom a layer of complexity is added. In particular the atoms now have interactions, not only with their own type, but also with the other atomic species. This interaction, quantified and described by the scattering length a_{ij}, may also exhibit a Feshbach resonance that can be readily controlled. As such the two atomic species may be readily repelled or attracted to another. These types of systems can display a phase transition from the miscible to immiscible regime depending on how they interact [67]. In the miscible regime, an equal density distribution of each atomic species is expected across the trapping region while in the immiscible segregation of the two atomic species is expected. While a relatively simple concept, this property of atomic mixtures provides rich topological potential as one moves along the miscibility spectrum.

Initially, ultra-cold atomic mixtures were Fermi-Bose mixtures focussed on achieving degenerate Fermi gases while using the Bose component to sympathetically cool the Fermi gas. However the Bose-Bose mixtures have gained traction as of late. A decade ago only double species experiments existed, ^{41}K-^{87}Rb [68], ^{39}K-^{87}Rb [69], ^{174}Yb-^{176}Yb [70] being the pioneering mixture experiments. Today many more exist, developed with specific research goals in mind. A number of ^{85}Rb-^{87}Rb apparatus exist that are geared towards improvements in atom interferometry [66], and their usage as a space-based interferometer [71]. Similarly more exotic mixtures are regularly demonstrated. This includes the work towards a dual species dysprosium condensate (^{160}Dy-^{162}Dy), useful for ultra cold dipolar physics [72].

Here we are interested in the usage of the dynamics of a quench across a Feshbach resonance to induce the transition from miscible to immiscible phase. Such a system does not instantaneously separate into two distinct atomic regions, but rather undergoes a more complex dynamical trajectory [73, 74]. Recent theoretical work from Hofman et al. [75] and Karl [76] has explored these dynamics and examined their non-trivial behaviour. Interestingly, this system is expected to exhibit self-similar behaviour at different time scales of the dynamics. In essence, the system dynamics are independent of the microscopic dynamics, and time evolution of any ensemble quantity is captured in the rescaling of a characteristic length scale. In domain dynamics this refers to region size growth with time. Thermalization of this experiment occurs when only two macroscopic domains of each species remains but the emergence of long-lived non-equilibrium states have been predicted [76]. Exploration of dual species condensates and their associated superfluid to Mott insulator transition, on a variety of lattice geometries, is also of future interest.

The experimental apparatus, discussed in this thesis, was thus constructed to create a dual-component condensate of ^{87}Rb and ^{41}K. This particular mixture was chosen as potassium and rubidium mixtures are relatively well established in the field [77, 78, 79, 80]. As a result it was anticipated that construction, development and optimising time could be reduced significantly if instead another, less known, mixture was attempted. ^{87}Rb may be used as a thermal reservoir to efficiently cool ^{41}K to aid in reducing it to degeneracy. Most importantly, however, is that two broad, magnetic Feshbach resonances between the two species. These exist at experimentally accessible magnetic fields allowing good control over the interaction strength between the two types of atoms.

The design, construction and initial performance of the experimental apparatus that will produce ^{87}Rb and ^{41}K condensates are the culmination of my Masters work. Chapter 2 of this thesis is devoted to an overview of theoretical foundations required to create a degenerate atomic gas. Chapter 3 will discuss the design and construction of the major infrastructure elements required to begin the pathway to condensation while Chapter 4 describes technical details on the experiments performance thus far, including the achievement of a ^{87}Rb BEC. Lastly Chapter 5 will discuss the future plans for the experiment before presenting an overview on the research activity undertaken during the previous two years.

Chapter 2

Laser Cooling, Magnetic Trapping and Evaporation

This chapter contains theoretical basis of techniques used to cool, trap and condense atoms in our apparatus. The order of material is presented to correspond to the progression of the experimental procedures, currently in place and those to be implemented, used to create cold and degenerate gasses in the laboratory. Theory to be discussed is the (a) principles behind laser cooling and trapping in a magneto-optical trap, (b) magnetic trapping, (c) evaporative cooling, (d) optical dipole traps, (e) imaging and analysis techniques and (f) theory of Bose-Einstein condensates.

2.1 Laser Cooling and Trapping

The use of laser light for the cooling and trapping of atoms is the starting point of virtually all ultra cold atom experiments. It enjoys a rich history that culminated in the 1997 Nobel Prize in Physics award [81, 82, 83] for development of the experimental methods and theoretical understanding of the phenomena, given to W. Phillips, C. Cohen-Tannoudji and S. Chu. However, the history of atom light interactions is older by several centuries, dating back to Kepler in his 1619 treatise 'De cometis' [84]. This hypothesised radiation pressure, proposed on the observation of comet tails pointing away from the sun [84]. A greater understanding was achieved in the 19th century through Maxwell's equations and a similar expression derived by Bartoli in 1876 [85, 86]. Despite this progress, it was several decades before the first experimental measurement of radiation pressure took place, undertaken by Lebedev [87] and then Nichols and Hill [88, 89]. This force was experimentally quantified by allowing light to fall upon a delicately poised vane of metal in a torsion-balanced Crookes apparatus with variable internal pressure. Subsequently, in 1917, Einstein introduced the concept of a photon to describe the energy exchange that occurs between fields and particles [90]. Following these experiments, interest in radiative forces grew quickly as a potential tool for the investigation of emerging relativistic [91] and quantum theories [92].

Formal laser cooling and trapping began in the '70*s* when Hänsch & Schawlow [93] and Wineland & Dehmelt [94] independently proposed using laser light for the cooling of neutral atoms. Stable trapping configurations, however, were not proposed until 1978 by Ashkin [87] and realised for neutral atoms in 1981/2 for sodium [97]. The significance of laser cooling is now celebrated universally, not only by the award of the 1997 Nobel prize 'for the development of methods to cool and trap atoms with laser light', but due to the widespread use of these pioneering techniques as the basis for almost all cold atom experiments.

2.1.1 Atom-Light Interactions

The starting point for the preparation towards quantum degeneracy is the cooling and trapping of atoms with light. Here a brief derivation of the interaction is presented and the interested reader is referred to more comprehensive texts [96] and review articles [42].

An atom experiences a net force in the atom-light interaction as a result of several distinct processes taking place. These are photon absorption, spontaneous emission, and dipole forces. While all contribute to a single interaction, typically one dominates the other, playing very distinct roles in the cooling and manipulation of trapped atoms. Experimentally, cooling of atomic clouds generally depends primarily on the scattering force (absorption and emission), while the optical dipole force is mostly used for trapping and control. This is because it presents a nearly conservative trapping potential. Furthermore, the optical dipole force is only dependent on intensity gradients in a light field and thus can create a variety of trapping potentials.

That light has any effect on an atom is a result of the dipole moment, $\mathbf{p}$, which may be induced on an atom in the presence of an external electromagnetic field $\mathbf{E}$. In the absence of saturation effects, the dipole density $\hat{\mathbf{p}}$ can be linearly related to the electric field;

$$\langle \Psi | \mathbf{p} | \Psi \rangle = \alpha(\omega) \mathbf{E}. \tag{2.1.1}$$

Where $\alpha(\omega)$ is the complex polarisability of the atom, dependent on the laser frequency, ω. The imaginary part of the polarisability is related to absorption, appearing in the standard Lambert-Beer law, while the real part is associated with the reactive, or dipole, force. Polarisability is an integral component of the two forces associated with the atom-light interaction and a large amount of information may be gained from knowledge on its functional form. To find $\alpha(\omega)$ we consider an atom exposed to an external electric field, $\mathbf{E}$. For an isolated atom perturbed by the radiation, the total Hamiltonian becomes $\hat{\mathbf{H}} = \hat{\mathbf{H}}_0 + \hat{\mathbf{H}}_{dip}$, with $\hat{\mathbf{H}}_0$ the Hamiltonian in the absence of the field, and the perturbing dipole interaction given by:

$$\hat{\mathbf{H}}_{dip} = -\mathbf{p} \cdot \mathbf{E}. \tag{2.1.2}$$

To find the polarisability we need to find a solution to the time-dependent Schrödinger equation. This is done by considering the wave function, Ψ, to be a superposition of the eigenstates of the unperturbed system. Also note that $\mathbf{p} = -e\mathbf{r}$, where $\mathbf{r}$ is the coordinate of the electron and e the election charge. Assuming a two level system with ground state Ψ_1 and excited state Ψ_2 we may write,

$$\Psi(\mathbf{r}, t) = \rho_1(t)\Psi_1(\mathbf{r}, t) + \rho_2(t)\Psi_2(\mathbf{r}, t). \tag{2.1.3}$$

Where $\rho_1(t)^2 + \rho_2(t)^2 = 1$ and $|\rho_i(t)|^2$ are the state amplitudes. We assume separability and consider,

$$\Psi_i(\mathbf{r}, t) = e^{-\frac{i}{\hbar}E_i t}\phi_i(\mathbf{r}). \tag{2.1.4}$$

Here E_i are the energy eigenvalues of the unperturbed Hamiltonian. Assuming a classical laser field, $\mathbf{E}(t) = \mathbf{E}_0 cos(\omega t)$, and that the spatial variation of the field amplitude is insignificant compared to the length scale of the atom the time-dependent Schrödinger equation may be used to show,

$$\dot{\rho}_1(t) = \frac{i}{\hbar}\rho_2(t)\mathbf{p}_{12} \cdot \mathbf{E}_0 cos(\omega t) e^{-\frac{i}{\hbar}(E_2 - E_1)t}, \tag{2.1.5}$$

$$\dot{\rho}_2(t) = \frac{i}{\hbar}\rho_1(t)\mathbf{p}_{21} \cdot \mathbf{E}_0 cos(\omega t) e^{\frac{i}{\hbar}(E_2 - E_1)t}. \tag{2.1.6}$$

Here we have introduced the dipole matrix elements,

$$\mathbf{p}_{ij} = \langle i|\mathbf{p}|j\rangle = \int \phi_i^*(\mathbf{r})\mathbf{p}(\mathbf{r})\phi_j(\mathbf{r})dV. \tag{2.1.7}$$

These define the coupling between the two states due to the oscillatory field. The strength of this coupling is measured by the Rabi frequency, Ω, given by

$$\Omega = \frac{|\mathbf{p}_{12} \cdot \mathbf{E}|}{\hbar} = \frac{|\mathbf{p}_{21} \cdot \mathbf{E}|}{\hbar}. \tag{2.1.8}$$

This expression accurately describes the population exchange between the ground and excited state when exposed to an external field but does not account for spontaneous emission from the upper state. This is an integral element of the atom-light interaction. This may be introduced via the on resonance dampening term $\Gamma_{\omega_0} = \Gamma_w = \Gamma$ that acts to deplete the upper state. Defining the transition energy between the states as $\omega_0 = (E_2 - E_1)/\hbar$, eqn. (2.1.5) & (2.1.6) may be re-written as:

$$\dot{\rho}_1(t) - \frac{\Gamma_{\omega_0}}{2}\rho_2(t) = i\rho_2(t)\Omega cos(\omega t)e^{-i\omega_0 t} \tag{2.1.9}$$

$$\dot{\rho}_2(t) + \frac{\Gamma_{\omega_0}}{2}\rho_2(t) = i\rho_1(t)\Omega cos(\omega t)e^{i\omega_0 t}. \tag{2.1.10}$$

Where, for red detuned beams, $\Gamma_{\omega_0} = (\omega^2/\omega_0^2)\Gamma$ are the on resonant damping coefficients, and Γ the natural line width. By looking at the steady-state solution in the presence of an electric field, i.e. the case where the state populations are constant, $\alpha(\omega)$, may be found. Steady state occurs when.

$$\frac{d}{dt}|\rho_i(t)^2| = 0. \tag{2.1.11}$$

Further,

$$\langle \Psi|\mathbf{p}|\Psi\rangle = \int \Psi^* \mathbf{p} \Psi dV = \rho_1^* \rho_2 \mathbf{p}_{12} e^{-i\omega_0 t} + \rho_1 \rho_2^* \mathbf{p}_{21} e^{i\omega_0 t} = \alpha \mathbf{E}_0 cos(\omega t). \tag{2.1.12}$$

After some rearrangement and simplifications the atomic polarisability may then be given by,

$$\alpha(\omega) = 6\pi\epsilon_0 c^3 \frac{\Gamma/\omega_0^2}{\omega_0^2 - \omega^2 - i(\omega^3/\omega_0^2)\Gamma}. \tag{2.1.13}$$

Where the natural linewidth Γ is calculated by evaluating the dipole matrix element,

$$\Gamma = \frac{\omega_0^3}{3\pi\epsilon_0 \hbar c^3}|\langle \Psi_2|\mathbf{p}|\Psi_1\rangle|^2. \tag{2.1.14}$$

With this expression, for the atomic polarisability, the dipole potential and scattering rates may be found. Recalling that these are the two forces arising in the atom-light interaction related to the real and imaginary component of the complex polarisability. The dipole interaction potential of the induced dipole is given by:

$$U_{dip} = \frac{1}{2}\langle \mathbf{p} \cdot \mathbf{E} \rangle = -\frac{1}{2\epsilon_0 c}\mathrm{Re}(\alpha) I(\mathbf{r}). \tag{2.1.15}$$

Where the brackets denote the time average over the rapid oscillating terms, and the spatially varying field intensity is given by $I(\mathbf{r})$. The dipole force is the gradient of the interaction potential such that;

$$\mathbf{F}_{dip} = -\nabla U_{dip} = \frac{1}{2\epsilon_0 c}\mathrm{Re}(\alpha)\nabla I(\mathbf{r}). \tag{2.1.16}$$

Similarly the scattering force is derived from the imaginary, out of phase, component of the dipole oscillation that may be interpreted in terms of the photon scattering in cycles of absorption and subsequent spontaneous re-emission processes. The corresponding scattering rate is given by:

$$\Gamma_{sc} = \frac{P_{abs}}{\hbar\omega} = \frac{1}{\hbar\epsilon_0 c}\mathrm{Im}(\alpha) I(\mathbf{r}), \tag{2.1.17}$$

where P_{abs} is the absolute power at the atom location.

In most experiments the laser frequency is tuned sufficiently far from ω_0 such that nonlinear contributions are negligible but close enough that the detuning is much smaller than the resonant frequency, i.e. $|\delta| << \omega_0$. In this situation the rotating wave approximation holds and the following useful expressions for the dipole potential and scattering rate may be found:

$$U_{dip}(\mathbf{r}) = \frac{3\pi c^2}{2\omega_0^3}\frac{\Gamma}{\delta} I(\mathbf{r}), \tag{2.1.18}$$

$$\Gamma_{sc}(\mathbf{r}) = \frac{3\pi c^2}{2\hbar\omega_0^3}\left(\frac{\Gamma}{\delta}\right)^2 I(\mathbf{r}). \tag{2.1.19}$$

These expressions not only quantitatively describe the atom-light interaction for small detunings but also convert valuable information for designing experiments. Firstly, the dependence of the dipole force on intensity gradients, $\nabla I(\mathbf{r})$ is discussed. This is significant as having a non-uniform light field may create a confining potential. Additional, for the dipole force, we can understand how the sign of the detuning determines whether the light field has an attractive or repulsive character. In the case of red detunings, $\delta < 0$, the intensity maximum represents the minimum of the potential, and atoms will accumulate in these areas. Conversely, for blue detunings, $\delta > 0$, intensity minima are the minimum of the potential and atoms will be repulsed by intensity maxima. Each type of trapping landscape holds its own advantage and disadvantages, which must be considered when designing trapping potentials.

Lastly the scaling of the dipole potential and scattering force is of interest. The dipole force scales as I/δ while the scattering scales as I/δ^2. At sufficiently large detunings the scattering force becomes small and a dipole field may be considered nearly conservative. It is not advisable to have dipole traps with comparable reactive and scattering rates, as their shallow depth means that even a few scattering events may cause heating and rapid depletion of atoms. The fine points of the scattering rate equation, and its implications, will be discussed in depth later.

The treatment of a two-level system represents a simplification of real atoms. In order to calculate the actual dipole potential of multilevel alkali atoms, such as ^{87}Rb and ^{41}K, a common detuning over the relevant transition cannot always be assumed. When substates and multiplicity are taken into account, a more accurate description of the potential is given by:

$$U_{dip}(\mathbf{r}) = \frac{\pi c^2 \Gamma}{2\omega_0^3}\left(\frac{2 + P_{g_F m_F}}{\Delta_{2,F}} + \frac{1 - P_{g_F m_F}}{\Delta_{1,F}}\right). \tag{2.1.20}$$

Here $P_{g_F m_F}$ is a polarization-dependent factor, equal to $0, \mp 1$ for linear and $\sigma^{\pm}$ polarization respectively. $\Delta_{1,F}$, $\Delta_{2,F}$ are detunings of the D_1 and D_2 lines respectively. This assumes all optical detunings are large compared with the excited state hyperfine splitting.

The dissipative component of the atom-light interaction, arising from scattering events, may be used to determine the scattering force. Given each scattering event has a non-zero interaction time, there exists some light intensity at which the upper state becomes saturated. This saturation intensity, I_{s}, is given by,

$$\frac{I}{I_{\mathrm{s}}} = \frac{2\Omega^2}{\Gamma^2}. \tag{2.1.21}$$

Using the expression for the scattering rate in Eqn 2.1.17 and the complex atomic polarisability, the scattering force is given by the time averaged scattering events and momentum kick due to a photon interaction,

$$F_{sc} = \hbar \mathbf{k} \Gamma_{sc} = \hbar \mathbf{k} \frac{\Gamma}{2} \frac{I/I_{sat}}{1 + (2\delta/\Gamma)^2 + I/I_{sat}}. \tag{2.1.22}$$

This dissipative force is used in the early stages of most experiments to cool atoms down to

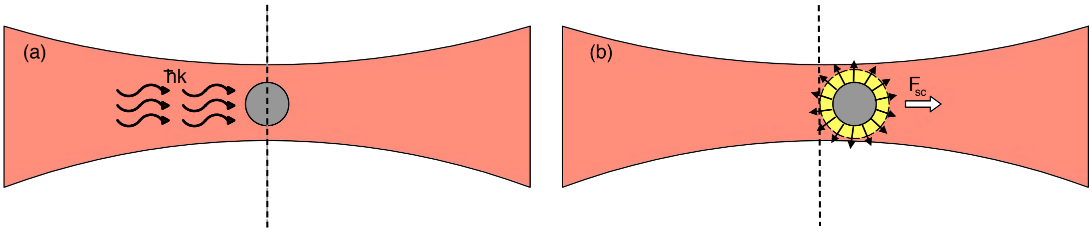

Figure 2.1.1: Basic depiction of Doppler cooling via the scattering force F_{sc}. (a) Photons incident on a particle are absorbed as it is excited to an intermediate state before spontaneous emission results in decay to the ground level. The absorption cycle results in a momentum kick in the direction of the photon before a similar, randomly orientated, kick occurs in spontaneous emission. However as the emission, averaged over many cycles, is isotropic the net result is that the F_{sc} may be used to slow atoms.

a low temperature in additional to confining them to a small volume.

2.1.2 Doppler Cooling

Laser cooling relies on the dissipative force of the atom-light interaction that can be used to slow atoms. This dissipative force is related to the absorption and spontaneous re-emission of photons, known as scattering events. For a two-level atom, the absorption of photon results in energy being transferred to the internal state as it is excited to some state. Conservation laws require that the atoms centre of mass recoils in the direction of the photons wave vector. Following this, the atom spontaneously decays back to the ground state emitting a photon in some random direction resulting in a secondary momentum kick. As the re-emitted photon is scattered in some random direction, over a large number of absorption cycles the net force from spontaneous decay becomes isotropic, Fig (2.1.1). The result is that the atom experiences a net overall acceleration in the direction of the photons. This is the basis for the vast majority of common laser cooling techniques.

This is the basic mechanism for using the scattering force for cooling atoms, which was known for quite some time. Despite this, it took several years before a stable experimental method, for using the scattering force to contain atoms was found. However, stable trapping was observed early for the dipole force [97]. However, many obstacles were encountered when trying to create an environment where the scattering force could be used [98]. In particular it was realised that, due to an optical analogy of the Earnshaw Theorem, configurations of 3D trapping, using the dissipative force, were limited. This is similar to how a charged particle cannot be placed in a stable orientation in a distribution of static charges. Once this was determined it became apparent that stable configurations could exist, yet the optical Earnshaw Theorem restricted what could be used [99, 100]. These configurations take advantage of the atoms possessing complex internal degrees of freedom. In particular, phenomena such as Doppler and Zeeman shifts make atomic cooling and trapping possible.

The first proposal of a technique to effectively and isotropically cool atoms with the scattering force was made in 1975 by two separate groups [93, 94]. This method, known today as optical molasses, consist of three counter propagating beam pairs along orthogonal axis with an atomic vapour about their intersection volume. By appropriately setting the detuning of the beam such that it is red-detuned from the stationary resonance, an effective cooling force may arise. At first glance this may not seem possible as the symmetrical arrangement has no net effect on the atom due to equal and opposite scattering events occurring from each axis. This is only true, however, for stationary atoms. An atomic vapour at a finite temperature has a Maxwell-Boltzmann distribution of velocities. As such, the effect of Doppler shifts leads to an imbalance of forces along the velocity axis.

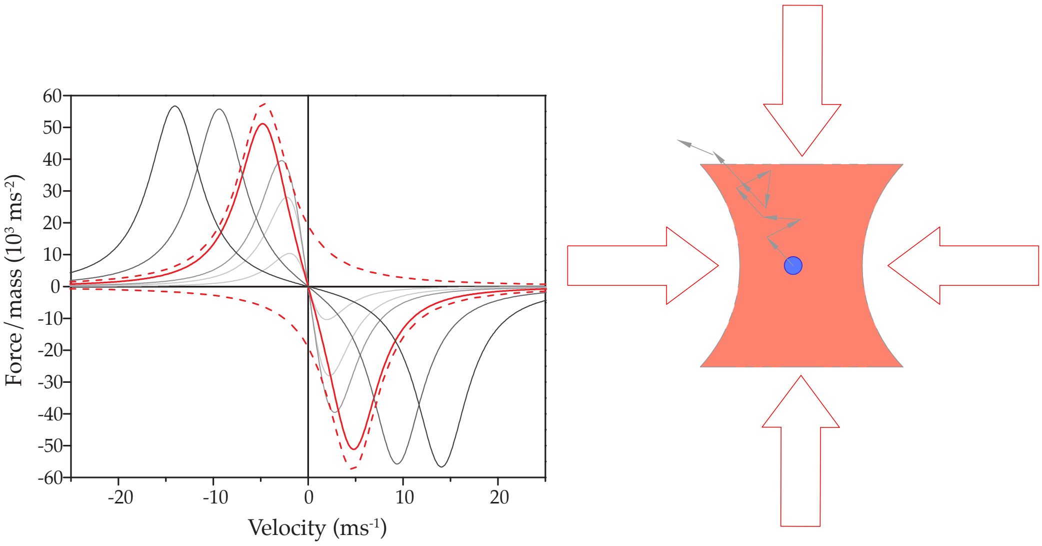

Figure 2.1.2: (a) Illustration of the velocity dependent force in a one-dimensional optical molasses. These curves are plotted for ^{87}Rb at saturation intensity, for a variety of different detunings. The dashed lines show the components from each beam in the 1D molasses. Image from [80]. (b) Diffusive nature of an atom in a 2D-optical molasses caused by the recoil of an atom from each spontaneous emission cycle. This sets a minimum in attainable temperature for the atoms while also preventing the technique to be utilised for trapping purposes.

To illustrate how Doppler shifts allow for cooling we consider a simplified one-dimensional molasses with two counter-propagating, red detuned beams along the z-axis. Due to the Doppler effect atoms approaching a 'red' detuned beam will see the frequency shift towards resonance while those moving away will be more detuned. As such the effective detuning, Δ_e, of a beam is altered by a factor $\pm\Delta_\pm$ depending on whether it is approaching or moving away from a beam. As a result the effective, velocity dependant, detuning becomes,

$$\Delta_e = \Delta + \Delta_\pm, \tag{2.1.23}$$

$$\Delta_\pm = \mp k v_z, \tag{2.1.24}$$

where v_z the velocity of the atom and k the wave vector of light. As a result, as an atom approaches a red-detuned beam the frequency moves closer to resonance increasing the chance of a scattering event. Conversely, the co-propagating beam will be blue shifted and therefore less scattering events will occur. As a result a recoil scattering imbalance occurs and more momentum kicks given opposite to the atoms direction, trying to oppose its motion. Given this is a force opposing the motion it can be considered a frictional force, F_r, given by the sum of the contributions from the two beams. Further by assuming kv is small compared with δ we can show:

$$F_r = F_+ + F_- = F_{sc}(\Delta - kv_z) - F_{sc}(\Delta + kv_z) = -2\frac{\delta F_{sc}}{\delta\omega} kv_z = -\alpha v_z. \tag{2.1.25}$$

The new force opposes the motion of the atom, such as movement through a viscous fluid (e.g. molasses). The dampening coefficient α, using Eqn. (2.1.22), is also given by,

$$\alpha = -4\hbar k^2 \frac{(I/I_s)(2\Delta/\Gamma)}{\left(1 + 2I/I_s + (2\Delta/\Gamma)^2\right)^2}. \tag{2.1.26}$$

Overall the net force, shown for various atomic velocities v_z in Fig 2.1.2 (a), will cool moving atoms that subsequently accumulate towards the centre of the trap. Unfortunately this mechanism is not confining, as in addition to the dissipative force, the stochastic nature of the photon absorption and emission cycles becomes significant. In particular it culminates in momentum fluctuations that limit the lowest obtainable temperature due to the manifestation of a random walk. This momentum diffusion continues until atoms leave the molasses volume, Fig 2.1.2 (b). This limit in achievable temperature is discussed before a brief on the modifications to the basic molasses technique required to create spatial confinement.

Doppler Limit and Sub-Doppler cooling

The one-dimensional example, presented above, may be expanded to practicality in the laboratory by the addition of two further pairs of counter-propagating beams. This provides interactions with the atomic ensemble in each direction of motion, allowing isotropic cooling. The cooling itself is provided by the absorption-reemission cycle, previously discussed. Each remission results in a equal but opposite momentum kick to the atom, with a recoil velocity of $v_r = \hbar k/m$ that limits the lowest obtainable temperature, known as the Doppler limit and is given by,

$$\mathrm{k}_B T_D = \frac{\hbar\Gamma}{2}. \tag{2.1.27}$$

For ^{87}Rb, one of the atomic species used in our experiment, this limit is $T_D \approx 144\ \mu$K. Interestingly, while this was presumed to be the lowest obtainable temperature achievable in an optical molasses cooled cloud, early experimental results were at odds demonstrating clouds with temperatures below the Doppler limit [96, 101, 102, 103]. This is a direct consequence of the multiplicity of sub-levels of real atoms and their interaction with polarisation gradients of an optical field. This multiplicity can be exploited, through a range of techniques, to routinely create sub-Doppler cooled atomic clouds.

A brief overview of the most well known sub-Doppler cooling mechanism is presented for a general understanding of what is achievable. This is known as Sisyphus cooling, illustrated in Fig 2.1.3. Consider an atom, with two fine structure separated states, $J = 1/2$ and $J' = 3/2$, in two counter propagating beams with orthogonal polarisation. This will cause a periodic rotation of polarisation. This will cause atoms in each state to experience equal but opposite energy shifts, resulting in an out-of-phase energy level field. As a result atoms in either state routinely move up through the potential hill before undergoing an absorption cycle into the excited manifold. The subsequent decay goes to the lowest energy level, resulting in spontaneous emission of a higher energy photon than that absorbed. A small overall loss of energy, and thus decrease in temperature ensues. The effect becomes cyclic as the atom continually moves through the periodic polarisation gradient.

Remarkably, the limit of the cooling process allows the atom to cool to the recoil limit when the energy loss being transferred to the potential minimum is balanced by the emission process. This is the recoil energy given by

$$T_{rec} = \frac{(\hbar k)^2}{2m\mathrm{k}_B}. \tag{2.1.28}$$

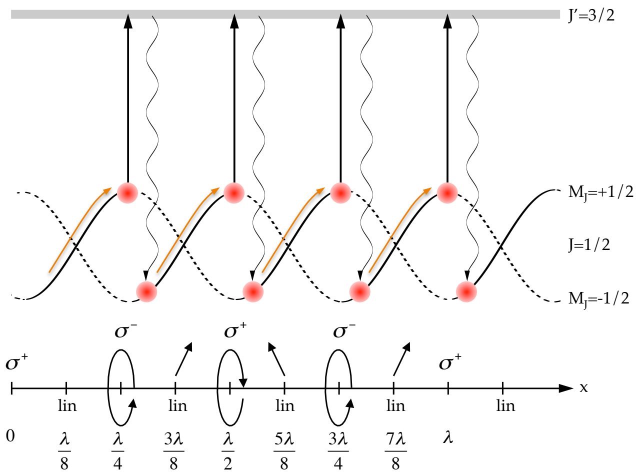

Figure 2.1.3: Left - Illustration of the Sisyphus sub-Doppler cooling mechanism. As an atom in the $M_J = 1/2$ state moves along the potential curve it experiences a periodic shift in its energy level reaching a maximum when light is $\sigma-$ polarised. At this point the atom is excited into the $J' = 3/2$ state before spontaneous decay into the $m_J = -1/2$ state, preferentially. This state lays at a lower energy and subsequently the atom must loss some kinetic energy to emit the photon. This process become cyclic as the atom climbs to a maxima at $\sigma+$ polarised light before the absorption-emission process puts it back into the $m_J = 1/2$ state. Image taken from [80].

Similar mechanisms exist for other polarisation combinations and the interested reader is directed to Ref [96].

2.1.3 Magneto-Optical Trap

While the optical molasses technique is capable of cooling an atomic cloud, the stochastic nature of the method allows them to leave the beam intersection volume. As a result three orthogonal beam pairs do not constitute a trap. Confinement is obtained by creating a spatially-dependant restoration force that continues to force atoms to the centre. This may be done by application of a spatially varying magnetic field and appropriately configuring the polarisation of the optical molasses beams, exploiting Zeeman shifts of atomic sub levels. In doing so we can create a magneto-optical trap (MOT), a technique developed in 1987 [104], a staple for modern cold atom experiments. The simplest MOT is formed by the overlap of a spherical magnetic quadrupole field with the molasses field. This provides a linearly increasing magnetic field extending from the centre of cooling region to the edge of the coils. This may be provided by a single pair of coils with counter-propagating currents, shown in Fig (2.1.4). The difference between the pure optical molasses is that the application of a magnetic field enables spatial confinement due to the exploitation of Zeeman shifts of an atoms magnetic sub levels, section 2.3.

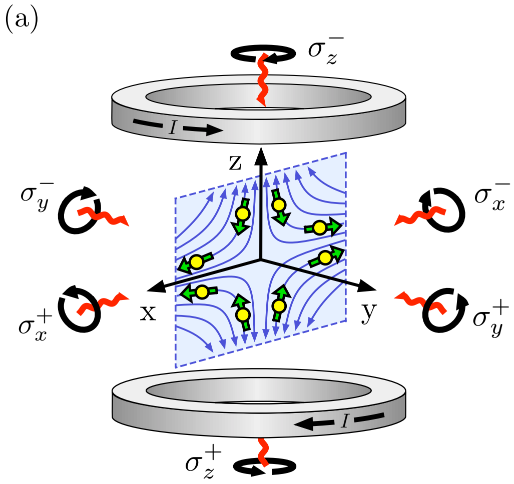

Figure 2.1.4: Illustration of a magneto-optical trap with anti-Helmholtz configuration coils. This results in a spherical quadrupole, producing a linear splitting of Zeeman sub levels used to confine atoms to the molasses volume. Via the appropriate polarisation of the incident beams the atoms may be trapped at the centre. Image reproduced from [116]

Considering, once again for simplicity, the one-dimensional case, with the upper energy manifold split into three Zeeman sub-levels, $m_F = -1, 0, +1$, by application of the magnetic field. As atoms move from the centre of the trap the $m_F = \pm 1$ is brought closer to resonance, as the Zeeman field shift increases with increasing magnetic field. Optical transition laws dictate that atoms from the lower manifold, $m_F = 0$, may only make transitions $m_F = \pm 1$ contingent on the interacting beams polarisation $\sigma^{\pm}$. As a result of the Zeeman shift, and its spatial dependence, atoms then exhibit a spatial dependence on the likelihood of an absorption event occurring that serves to localise a vapour towards the centre. This is to say; atoms further from the centre of the trap preferentially absorb photons compared to those, which are localised about this centre, resulting in a spatial restoring force. This trapping configuration is common for ultra cold atomic gases as it may readily create large MOTs, with $> 10^9$ atoms [105, 106, 107], at low temperatures. When considering real atoms the existence of multiplicity, of the atomic sub-levels, brings other considerations when trying to trap and cool atomic gases.

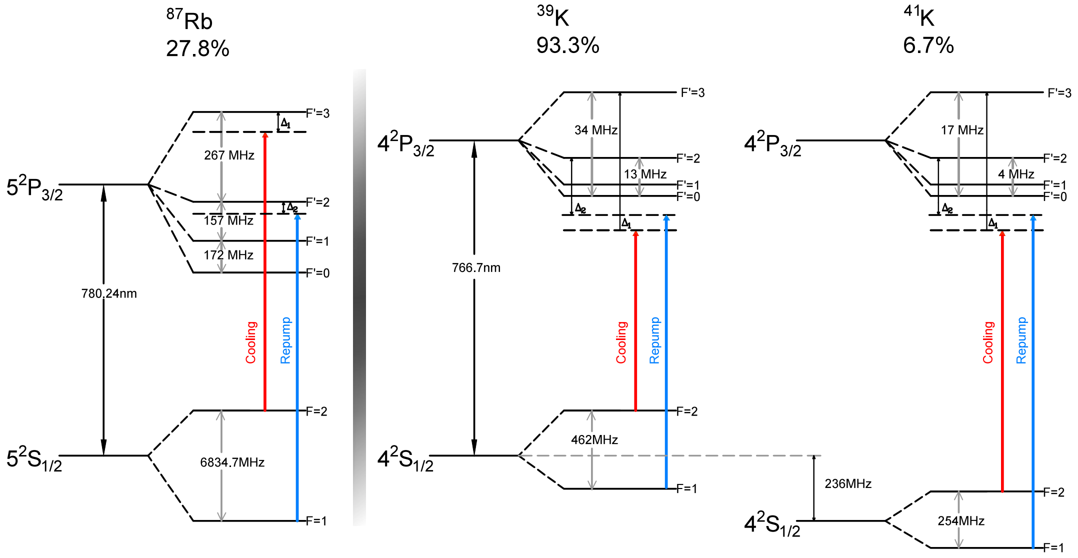

Figure 2.2.1: Atomic level diagrams for ^{87}Rb and the stable bosonic isotopes of potassium. Abundances are listed below the isotope name and Δ_1 and Δ_2 are the frequency detunings for the repumping and cooling transition respectively. The energy level gaps are not to scale and exacerbated for clarity.

2.2 ^{87}Rb and ^{41}K

While the previous section allows for a good qualitative analysis, and proposal, for the basis of laser cooling and trapping techniques, real atoms possesses much more complicated electronic level structures, consisting of multiple ground and excited states as well as decay paths. Application of the general principles of dissipative cooling, presented here is complicated by this fact. Fortunately the alkali atoms of interest, ^{87}Rb and ^{41}K, have a single valence electron that allows the cooling process, reliant on the continuation of absorption-reemission cycles, to be simplified. In this section a description of the multi-level structure of the two atoms is presented to elucidate the operating principles of the 3D MOT.

Here we are concerned with the electronic level structure, which defines the laser frequency requirements of our system, the bosonic isotope of rubidium, ^{87}Rb, and potassium, ^{41}K, respectively. Both these atoms possess suitable transitions for cooling and trapping in the D_2 level structure. With regards to rubidium this is between the $5^2S_{1/2}$ ground state and $5^2P_{3/2}$ excited state, while for potassium it is the $4^2S_{1/2}$ and $4^2P_{3/2}$ Fig 2.2.1 shows that the level structure for the two elements are similar, due to the fact they both have nuclear spin $I = 3/2$. The D_2

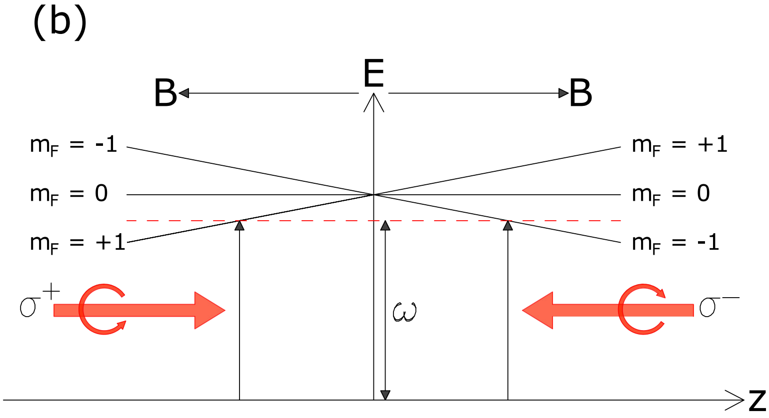

Figure 2.2.2: Illustration of the trapping mechanism for a MOT. As atoms move from the trap centre in the $z = \pm$ direction the $m_F = \pm$ energy levels shift due to the Zeeman effect. As such atoms that move from the trap centre preferentially absorb photons from the counter-propagating beam that enable only a transition to the closer on-resonance sub-level. The net result is a spatial active restoring force from the optical molasses.

line links four hyperfine P states to two low-lying S states. The selection rules lead to the same allowed hyperfine transitions for both atoms. The natural linewidth is $\Gamma = 6.0$ MHz for ^{87}Rb and 6.2 MHz for ^{41}K.

The cooling transition for both atoms is the $|F = 2\rangle$ to $|F' = 3\rangle$, being the only, nearly, closed transition in the D_2 structure. This constitutes the cycling transition used in laser cooling, with saturation intensities of $\simeq 1.7$ mW cm^{-2} [108]. Nevertheless, the presence of additional states in the lower fine structure manifold disrupts the possibility of cooling and trapping with a single frequency source. The existence of off-resonance contributions, from the $|F = 2\rangle$ to $|F' = 2\rangle$ and $|F = 2\rangle$ to $|F' = 1\rangle$, acts to readily deplete the starting $|F = 2\rangle$ level, filling the $|F = 1\rangle$ level. This may be mitigated through the use of what is known as repumping light. A beam red detuned of the $|F = 1\rangle$ to $|F' = 2\rangle$ transition, may irradiate the atoms causing those that fall into the $|F = 1\rangle$ state to be re-pumped back onto the cooling transition. Usually, for alkali atoms such as rubidium, these off-resonance effects are minimal and only a small amount of power is required for the repumping beam. Unfortunately this is not the case for bosonic potassium, where the tight hyperfine $4^2P_{3/2}$ level spacing is comparable to the natural linewidth, $\Gamma = 6.2$ MHz. The cooling transition, $|F = 2\rangle$ to $F' = 3\rangle$ is not closed and excites into the $|F' = 1, 2\rangle$ states with similar probability. Thus a repump power comparable to the cooling is required else fast depletion of the $|F = 2\rangle$ ground state, towards the $|F = 1\rangle$, ensues. Given the comparability of the transitions the distinction between cooling and repumping beams is mostly semantic, but is kept for clarity when discussing the laser sources for cooling and trapping the atoms. The repump and cooling transitions are shown by red and blue arrows in Fig. 2.2.1 respectively. Furthermore in order to do any quantitative analysis an imaging beam is required. This is achieved using light resonant with the cooling transition.

Other complications arise when attempting to cool bosonic potassium, as a delicate balance between having a large capture volume and ability for sub-Doppler cooling exists. Due to the small separation of energy levels, cooling is only efficient when the detuning clears the entirety of the upper manifold [77, 109, 79]. It has been shown that the largest capture velocity is achieved when the cooling and repump beams are red-detuned from the entire excited-manifold, as per Fig 2.2.1. Consequently the large detunings does not produce effective sub-Doppler cooling forces and temperatures are expected to be on the order of mK [110, 111, 112]. One technique to achieve sub-Doppler temperatures, of these types of isotopes, is to perform standard Doppler cooling techniques first before reducing the cooling and repump beams detuning and varying the intensity significantly to counter-balance the heating mechanisms. Using this strategy temperatures on the order of tens of μK have been reported by two groups [113, 114].

2.3 Magnetic Trapping

While MOTs and sub-Doppler cooling provide a method for trapping atomic vapour, their temperature and volume are several orders of magnitude larger than that required for observation of condensation [43]. In order to further increase the atomic gas density, and enable cooling beyond the Doppler limit, magnetic traps may be used to provide a conservative potential. These do not rely on photon absorption re-emission cycles. Discussed in this section is the interaction that atoms, with non-zero magnetic dipole moment, have with an applied magnetic field. In the experiment presented here, the magnetic trap plays a pivotal role in trapping, moving and further cooling of our atomic clouds.

2.3.1 Atom Interactions in a Magnetic Field

The energy shift experienced by an atom in the presence of a magnetic field, B, is given by:

$$H_b = \frac{\mu_B}{\hbar}(g_s S_z + g_L L_z + g_I I_z) B_z. \tag{2.3.1}$$

With B_z the field along the z (quantisation) axis, S_z, L_z, I_z the operators for the z-components of the spin, orbital and nuclear angular momenta respectively, and g_s, g_L, g_I are the Landè g-factors. When this energy shift is small compared to the hyperfine splitting, $\mathbf{F} = \mathbf{I} + \mathbf{S} + \mathbf{L}$ and m_F are good quantum numbers. As a result, eqn (2.3.1) may be written as,

$$H_b = g_F \mu_B m_F B_z. \tag{2.3.2}$$

The resulting Zeeman energy shift is therefore non-zero and linear with field strength, given as

$$U(\mathbf{r}) = -\boldsymbol{\mu_F} \cdot \mathbf{B}(\mathbf{r}) = \mu_B g_F m_F B_z. \tag{2.3.3}$$

The force on an atom, $F(\mathbf{r})$, in the magnetic potential is therefore given by:

$$F(\mathbf{r}) = -\nabla U(\mathbf{r}) = -\mu_B g_F m_F \nabla B_z. \tag{2.3.4}$$

According to equation (2.3.4) that, depending on the sign of the product $g_F m_F$, atoms will minimise their total energy by moving to regions of lower, or higher magnetic field. The states for which $g_F m_F > 0$ are called low-field seeking states and are magnetically trappable as sta-

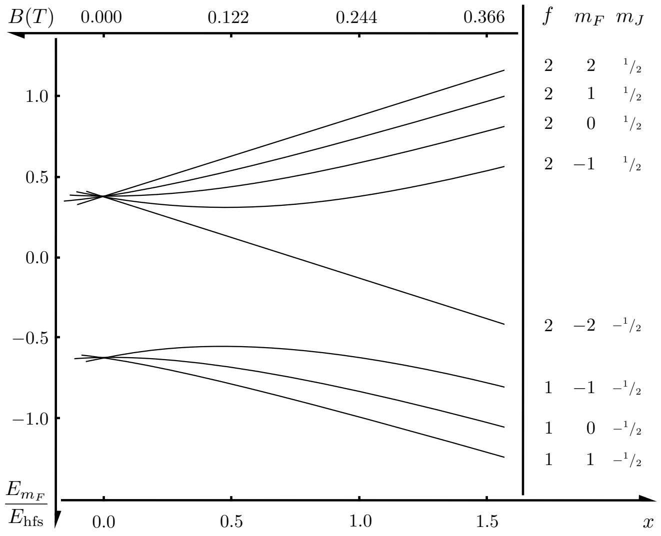

Figure 2.3.1: Breit-Rabi diagram for the energy level structure, E_{m_F}/E_{hfs} of ^{87}Rb ground state Zeeman shifts. Magnetically trappable states for both ^{87}Rb and ^{41}K are the$|F, m_F\rangle = |1, -1\rangle, |2, 1\rangle$ and $|2, 2\rangle$ states respectively. Image courtesy of [116].

ble configurations for local minima are possible. However, local maxima are not possible and high-field seeking atoms cannot be trapped by some static magnetic field. This is important when trying to load a magnetic trap from a 3D-MOT as the atoms have a distribution of sub-atomic states and cannot all be trapped. Magnetically trappable states of ^{87}Rb and ^{41}K are the $|F, m_F\rangle = |1, -1\rangle, |2, 1\rangle$ and $|2, 2\rangle$ states.

This treatment breaks down when the magnetic field applied becomes sufficiently large and the total electron $\boldsymbol{\mu_J}$ and nuclear $\boldsymbol{\mu_I}$ moment independently couple to it. The internal coupling is then treated as a perturbation to the interaction of the field with these independent moments. An analytical result exists for energy states belonging to the lower manifold of our atoms, i.e. $L = 0, J - 1/2$, in the form the Breit-Rabi formula [115], solutions shown for ^{87}Rb in Fig 2.3.1. These solutions are useful in the calibration of magnetic fields to access Feshbach resonances and better understanding effective field strength.

2.3.2 The Quadrupole Field

The simplest arrangement of electromagnetic coils, that provides a potential for holding low-field seeking atoms is the anti-Helmholtz configuration, consisting of two coils carrying current in opposite directions, Fig. (2.3.2) (a). This simple field also creates the linearly varying field

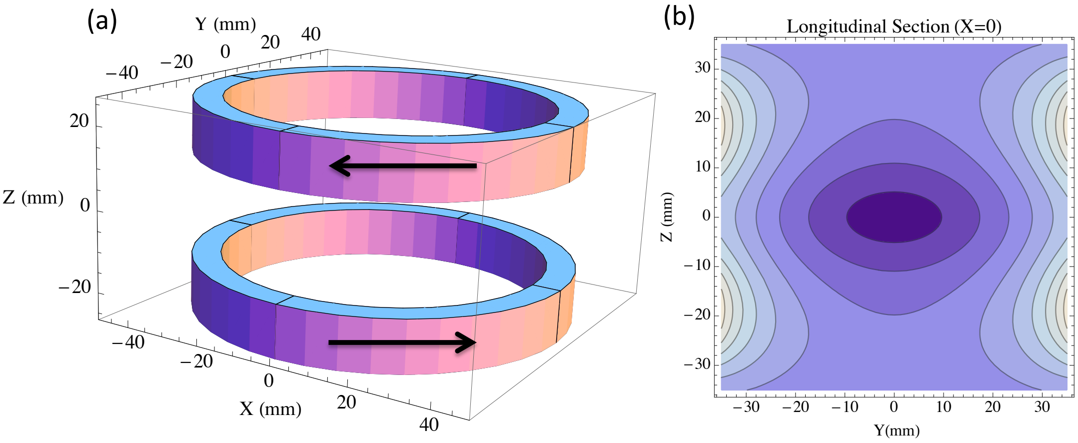

Figure 2.3.2: (a) Pair of coils in anti-Helmholtz configuration. The black arrows indicate the direction of current and (b) showing the field produced in the axial (z) and radial (y) direction. At the centre is a minima, representing the centre of a magnetic trap for low-field seeking atoms, linearly increasing with distance away.

required for the successful operation of the 3D-MOT. A single coil with current running through it has a field along the axial, B_z, and radial, B_r, directions given by,

$$B_z = \frac{\mu_0 I}{2\pi\sqrt{z^2+(a+r)^2}}\left(\frac{a^2-z^2-r^2}{z^2+(r-a)^2}E_2(k^2)+E_1(k^2)\right) \tag{2.3.5}$$

$$B_r = \frac{\mu_0 z I}{2\pi r\sqrt{z^2+(a+r)^2}}\left(\frac{a^2+z^2+r^2}{z^2+(r-a)^2}E_2(k^2)-E_1(k^2)\right). \tag{2.3.6}$$

Where z and r is the axial and radial distance from the centre axis of the coil, a the radius of the coil, $k^2 = \frac{4ra}{z^2+(a+r)^2}$ and $E_1(k)$ and $E_2(k)$ the complete elliptic integrals of the first and second kind respectively. The total field strength is given by $|\mathbf{B}|^2 = B_z^2 + B_r^2$. These equations are especially important when trying to design high quality coils for trapping, transferring and producing bias fields. The field produced at the 'trapping' region of a pair of anti-Helmholtz coils is given, to a first order, by:

$$\mathbf{B} = B'(\frac{x}{2}\hat{\mathbf{e}}_x + \frac{y}{2}\hat{\mathbf{e}}_y + z\hat{\mathbf{e}}_z). \tag{2.3.7}$$

The resulting field has a zero at the centre point between the two coils with the field strength increasing linearly with increasing distance from the centre, Fig. (2.3.2) (b). It is important to appreciate that the strength along the axial, z, direction is twice that in the radial. In a 3D-MOT, only a small magnetic field gradient, ≈ 12 G cm^{-1}, is required to provide an appropriate restoring force in combination of the optical molasses. However, when transferred into a magnetic trap the field depth must be sufficient to hold the cloud against gravity. This is ≈ 31 G cm^{-1} for ^{87}Rb, however a steeper trap is desirable as it is more resistant to sources of heating, preventing rapid depletion of the ensemble. Here we trap at gradients of $B'_z = (100, 160)$ G/cm depending on which region of the experiment the cloud resides.

2.3.3 Majorana Losses

The final stage toward quantum degeneracy, following appropriate Doppler cooling and trapping in a conservative potential, is evaporative cooling, section 2.5. This serves to cool atoms down to the nK regime, required to observe the transition to BEC [117, 118, 119]. Within a quadrupole field an atom's magnetic dipole moment precesses about the local external magnetic field at the Larmor frequency, $\omega_L = \mu B/\hbar$. Provided the field direction changes slowly, with respect to the Larmor frequency, the moment will adiabatically follow the direction and remain within its trappable state. The specific criterion to satisfy this is,

$$\frac{1}{\omega_L}\frac{\mathbf{v}\cdot\nabla\mathbf{B}}{B} << 1. \tag{2.3.8}$$

What may be noted is that as the magnetic field approaches zero the adiabaticity criterion above may be violated. This may occur for atoms near a magnetic zero field at low temperature and thus spend a large amount of time near this point. As a result an atom may exhibit a transition to a different m_F state which is untrappable, and will be lost. These losses are known as Majorana spin-flips [120] and the limiting factor of the simple quadrupole field as temperatures approaching degeneracy are reached. Furthermore, the loss of cold atoms and rethermalisation of the remainder may result in an acute heating that prevents the Bose Einstein condensation transition from occurring [121].

Several methods exist to counteract these losses, the primary being the design of potentials with non-zero minima. Purely magnetic solutions, such as Ioffe-Pritchard and time-orbiting potential (TOP) traps, have been successful [122, 123, 124, 125]. Other options are the transfer to a purely optical potential where the spin-flips are no longer relevant [119, 126]. These optical potentials have very fast duty cycles but suffer from poor loading due to poor spatial mode matching between dipole trap and quadrupole traps. A final solution is a hybrid technique utilised in many modern experiments [127, 128] where the combination of magnetic and optical trap prevent Majorana losses becoming an issue during the evaporation stage towards degeneracy.

This last method is the one we have chosen to utilise in our experiment.

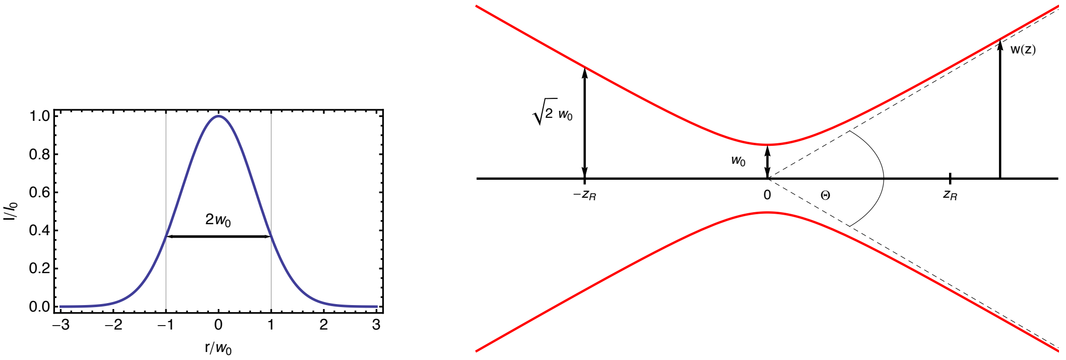

(a) Intensity profile of Gaussian laser beam at the waist.

(b) Beam profile ($1/e^2$) of a focused Gaussian laser along the axis of propagtion.

Figure 2.4.1: Beam profile of a focused Gaussian laser beam. The radius of the beam at the focus is given by w_0 the Rayleigh length determined by the distance it takes for the beam to expand to $\sqrt{2}w_0$, taken from [130].

2.4 Neutral Atoms in a Focused Gaussian Beam

Our discussion has mostly centred about the use of the scattering component of atom-light interactions and less concerned with the dipole force. Of most significance, for this experiment, is the effect of the dipole force for atoms residing about the focus of Gaussian beam. A focused laser beam, Fig (2.4.1), with power P propagating along the z-axis is described to have an intensity profile given by,

$$I(p,z) = \frac{P}{\pi w(z)^2} e^{-\frac{2p^2}{w(z)^2}}. \tag{2.4.1}$$

With radial coordinate p and the radius of the beam w when the beam intensity is $1/e^2$ of the maximum, in the radial direction.

$$w(z) = w_0\sqrt{1 + (z/z_R)^2}. \tag{2.4.2}$$

Where $z_R = \pi w_0^2/\lambda$ denotes the Rayleigh length and w_0 the smallest waist of the beam, at the focus. This focal point is also the trapping region of the beam, as trap depth is greatest here, occurring when U_0=U$(0,0)$. The dipole potential of neutral atoms may be approximated with a Taylor series if the kinetic energy, k$_B T$, of the atomic ensemble is much smaller than the depth of the trap. We may truncate the series at orders higher than two and gain the harmonic approximation,

$$U(p,z) = -U_0\Bigg(1 - 2\bigg(\frac{p}{\omega_0}\bigg)^2 - \bigg(\frac{z}{z_R}\bigg)^2\Bigg). \tag{2.4.3}$$

Quantifying the trap by its harmonic trapping frequencies,

$$\omega_p = \sqrt{\frac{4U_0}{m\omega_0^2}} \tag{2.4.4}$$

$$\omega_z = \sqrt{\frac{2U_0}{mz_R^2}}, \tag{2.4.5}$$

along the radial and axial directions, where m is the mass of the atom. The geometry of the trap is determined by looking at the aspect ratio between the axial and propagation axis, given by the ratio of the radial to axial frequencies trapping frequencies,

$$\frac{w_p}{w_z} = \sqrt{2}\frac{z_R}{w_0} = \sqrt{2}\frac{\pi w_0}{\lambda}. \tag{2.4.6}$$

Therefore, in general, the optical confinement of a single beam is stronger along the radial direction and weaker along the axial. This is important when making a single beam dipole trap as if the Rayleigh range is too great then the weak confinement may not be sufficient for trapping purposes.

With any trapping potential, the effect of gravity can greatly influence the geometry. In particular, assuming gravity along the axial direction of a single dipole beam, the acceleration of $g = 9.81$ m/s^2 causes an additional linear potential along its direction. This effect is not normally negligible unless $U_0 >> mgz$. For shallower traps, such as when optical evaporation is performed, an anharmonicity exists and gravity may begin to dominate. An example, of the effect of gravity, is shown in Fig (2.4.2). This is significant to be aware of as atoms may routinely ‘fall’ out of the trap as their own energy plus the effect due to gravity may exceed the potential depth. The effective trap depth, accounting for this effect, is given by the potential minimum which is shifted from origin by:

$$U_{\text{eff,z}} = mgz + I(0,z). \tag{2.4.7}$$

It is also convenient to refer to the potential depth by an equivalent temperature, for comparison with atom gas temperatures, given by U_0/k_B. The usefulness of this picture is that atoms that are hotter than this depth cannot be trapped. Interestingly to note is that the scattering rate is proportional to $I(p,z)/\Delta^2$, while the trap depth goes with $I(p,z)/\Delta$. As a result if the detuning

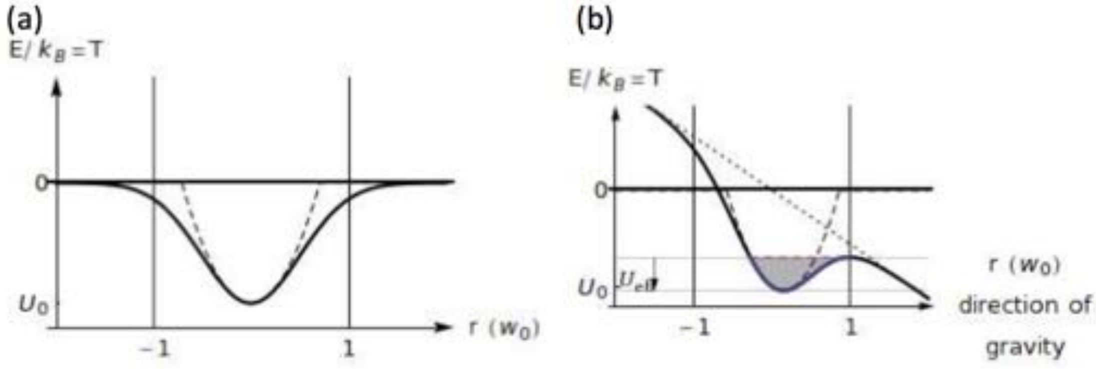

Figure 2.4.2: (a) Optical dipole potential without gravity, demonstrating symmetry about the centre. (b) Shows what occurs when gravity is no longer negligible. A skew of the trap occurs resulting in an asymmetry in the trap, which will be reflected in absorption images of an atomic ensemble. Image courtesy of [130].

of the trapping beam is far from resonance then the trap can be considered purely conservative. In practice background losses remove atoms from the trap prior to spontaneous emission induced losses become significant.

2.4.1 Decay, Parametric Heating and Losses

Precise knowledge of the trapping frequencies, allowing precise calculations of the Rayleigh length and w_0, is important when performing analysis on atoms in a dipole trap. These may be determined via parametric heating, by modulating the power of the trapping beam, at some frequency v. Due to the modulation atoms will be heated, and subsequently lost from the trap, when $v = 2\omega_i$, with $i = p, z$. This is also significant, as any noise on the trapping beam-matching v will cause atom number losses.

With a far-detuned beam, the atomic losses from light scattering events are negligible in comparison to other losses. The most significant of these are collision events, with background atoms determining the life time in the trap. One source of losses are collisions of trapped atoms with background vapour. This may be minimised by producing a low-vacuum environment, where the background vapour pressure is very low. As densities increase three body losses must also be taken into account. In this scenario, a molecule is formed between two atoms and the binding energy is transferred to a third. This also serves to rapidly deplete the number of confined atoms.

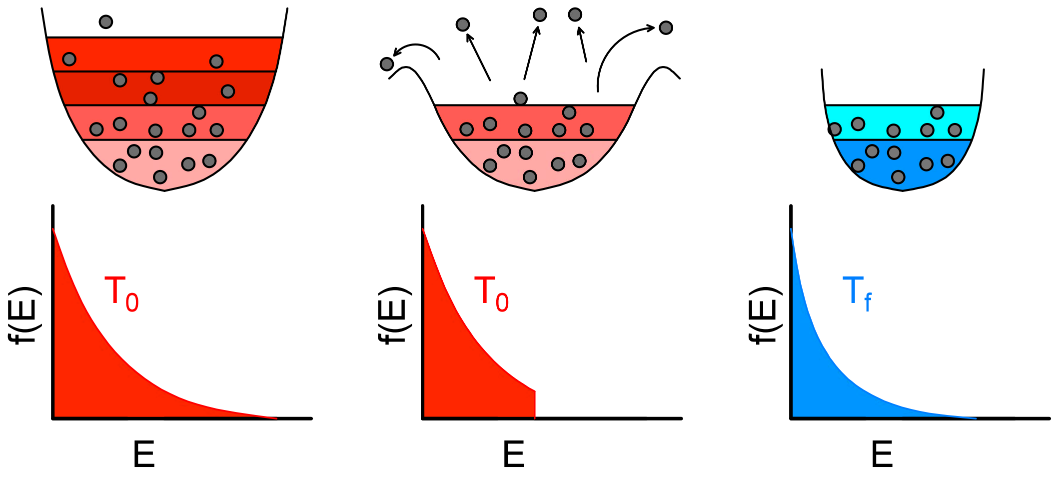

Figure 2.5.1: Evaporative cooling principle. Lowering the trap depth from some initial thermal distribution, $\langle T\rangle = T_0$ results in a truncation of trappable energies E. As a result the high-energy tail atoms are selectively removed and the remainder atoms re-equilibrates via collisions to a lower temperature T_f.

2.5 Evaporative Cooling

Laser cooling afforded physicists the ability to trap large samples of atoms at low temperatures and high density. The limit of the technique however, is that the temperature and density achieved in a conventional MOT does not have a phase-space density (PSD) high enough for the onset of condensation. Typically they are on the order of $\rho \approx 10^{-6}$ when in a MOT. This is several orders of magnitude lower than that required for the onset of condensation $\rho \approx 2$. To achieve this we can make use of evaporative cooling processes, a pioneering method for creating atomic clouds with high phase space densities [131].

Evaporative cooling is well understood conceptually. By selectively, and gradually, ejecting atoms from the edges of thermal distribution, remaining atoms may rethermalise via elastic two-body collisions. The net result is a lower equilibrium temperature, Fig. (2.5.1). The process itself amounts to truncating the trap depth, with a ‘knife’ energy, generally expressed as a multiple, η, of the cloud’s temperature T,

$$v_{\text{knife}} = \eta \text{k}_B T. \tag{2.5.1}$$

2.5.1 Microwave and Optical Evaporation

Several techniques for evaporative cooling, of atomic species, are available, with the elected method dependent on what is required. In this experiment two separate evaporative cooling methods are used to produce BECs of ^{87}Rb. Initially, microwave evaporation is used to prepare atomic clouds for loading into a hybrid trap. This is followed by optical evaporation until a condensate is formed. Microwave evaporation, used only on ^{87}Rb, relies on the spatially-varying

Zeeman shift in a magnetic trap. Intuitively, atoms with higher energy spend more time away from the trap centre. At the wings of the magnetic trap a large detuning of their hyperfine ground states is present, ≈ 6.834 GHz in absence of an external field. As a result, a particular microwave energy class is directly related to a certain spatial position in the trap these may removed from the trap to aid in evaporatively cooling the remainder of the gases. Our initial evaporative stage induces transitions from the trapped $|1,-1\rangle$ state to the untrappable $|2,-1\rangle$ manifold by sweeping the microwave frequency of radiation to selectively remove the most energetic atoms. In particular, a cloud may be irradiated by microwave radiation whose frequency is selected to only interact with the hottest of atoms. These are ejected from the trap and the remainder rethermalise to a cooler temperature. Care is required as if the ramp is executed too fast the sample has little time to rethermalise and additional atoms will be expelled before the cloud has equilibrated to a lower temperature. Following microwave evaporation the cloud is loaded

into an optical dipole trap where another stage of evaporative cooling occurs in order to produce a BEC. The principle behind optical evaporation is the same. By lowering the power in the dipole trap the trap depth is reduced and the more energetic atoms able to leave the trap. The remainder rethermalise to a lower temperature and the process can continue. Both these techniques are utilised within the experiment and addressed in greater detail in the relevant experimental chapters.

2.5.2 Efficiency

The figure of merit for the efficiency of evaporative cooling is the logarithmic derivative of the gain in phase space density, ρ, to the change in atom number, N. This is given by:

$$\gamma = -\frac{\mathrm{d}\ \mathrm{ln}\rho}{\mathrm{d}\ (\mathrm{lnN})}. \tag{2.5.2}$$

In an ideal scenario, where trap losses are wholly quantified by the evaporative procedure, the optimal rate for evaporative cooling is set by the initial temperature and by elastic collisional rate, $\Gamma_{el} = 1/\tau_{el}$. In reality, however, background losses are present due to collisions with untrapped atoms, while three-body losses at a rate $\Gamma_{loss} = 1/\tau_{loss}$ tend to oppose a rise in phase space density.

Thus, optimal cooling is a process by which γ is maximised, determined by the truncation factor η while also balancing the speed at which cooling occurs. In essence this is the optimisation of the ratio τ_{loss}/τ_{el} where the atoms should equilibrate as fast as possible compared to the rate at which they are lost from the trap. Generally these values are empirically found as background losses are highly experiment specific.

2.5.3 Sympathetic Cooling

Occasionally the direct evaporation of an atomic species is not desirable for cooling an ensemble. In the case of potassium the low natural abundance of ^{41}K leads to smaller atom numbers in a 3D MOT [68] making it inefficient for creating BECs as evaporative techniques incur large atom number losses. However, sympathetic cooling may be used to reduce the temperature of the ^{41}K component by using the rubidium cloud as a reservoir, or buffer gas, that acts as a coolant. Similar to regular refrigeration techniques, the temperature of a target gas is reduced by thermalisation with the reservoir.

2.6 Bose-Einstein Condensates

In this section, theoretical foundations of single species Bose-Einstein condensed (BEC) gases are discussed. In particular, the quantum-mechanical behaviour of ultra cold bosonic gases is discussed. This state of matter gives unique opportunities to study a variety of quantum effects on a macroscopic scale. These systems benefit from the large amount of intrinsic system control and control over atomic interactions, which can be advantageous when compared with other superfluid or superconductor systems.

2.6.1 Introduction

The rigorous theory of Bose-Einstein condensation in an ideal, interacting, zero and finite temperature gases has been discussed, in numerous review articles [132, 133], books [43] and theses. As such, for brevity, overviews of the main results that are relevant to our system are presented here.

A Bose-Einstein condensate (BEC) is a phase transition which relies on the indistinguishably of particles, composing an atomic ensemble. A description therefore needs to be treated with a quantum mechanical approach. The first prediction of this phenomenon was for photons, by Satyendra Nath Bose in 1924 [134], and generalised to encapsulate all bosons, by Einstein, the following year starting from studies on black body radiation [135] . Classically, the behaviour of a bosonic gas is determined by the Maxwell-Boltzmann distribution. In ordinary gases, independently of fermionic or bosonic nature, thermal energy $\mathrm{k}_B T$ is much higher than the energy level spacing of the system. A smooth distribution of state occupation is realised and no quantum exchange phenomena is relevant. This is not an accurate description, however, when a significant number of particles occupy the ground state.

2.6.2 Uniform Ideal Bose Gas

The mean occupation of single-particle states, n, for non-interacting bosons in thermal equilibrium is given by the Bose-Einstein distribution as,

$$f(\epsilon_n) = \frac{1}{\exp\Big[(\epsilon_n - \mu)/\mathrm{k}_B T\Big] - 1}. \tag{2.6.1}$$

Where ϵ_n is the energy of the n-th state and μ the chemical potential, which is set by particle number conservation. From this, the total number of particles may be evaluated by,

$$N = \sum_n f(\epsilon_n). \tag{2.6.2}$$

Importantly, the Bose-Einstein distribution also imposes the constraint $\mu < \epsilon_0$ for an ideal gas, lest a negative occupancy is observed. As μ approaches the energy level of the ground state the occupation of this level becomes equal to,

$$N_0 = f(\epsilon_0) = \frac{1}{\exp\Big((\epsilon_0 - \mu)/\mathrm{k}_B T\Big) - 1}, \tag{2.6.3}$$

which is large and comparable to the total number. This is the mechanism behind the phase transition to a degenerate quantum gas under specific conditions, discussed in the following section.

2.6.3 Semi-classical approximation

Treating the ground state as a special case, the total number of atoms in an ensemble, may be given by,

$$N = N_0 + N_T, \tag{2.6.4}$$

where N_T is the number of atoms in excited (thermal) states. Generally, calculating N_T is non-trivial, however, if we assume that thermal energy, $\mathrm{k}_B T$, is larger than the energy level spacing of the system, the summation over discrete states for thermal atoms may be replaced by a continuous integral over the density of states $\rho(\epsilon)$. Integrating over the entire phase space, the total thermal number of atoms may be given by,

$$N_T = \frac{1}{(2\pi\hbar)^3} \int\int \frac{1}{\exp\Big[(\epsilon(\mathbf{r},\mathbf{p}) - \mu)/\mathrm{k}_B T\Big] - 1} d\mathbf{p} d\mathbf{r}. \tag{2.6.5}$$

Here the discrete energy levels, ϵ_n, have been replaced by the continuous variable $\epsilon(\mathbf{r},\mathbf{p})$ dependant on position $\mathbf{r}$ and momentum $\mathbf{p}$. For a gas in a box, $\epsilon(\mathbf{r},\mathbf{p})$ is $p^2/2m$ and the position integral may be given by the volume of the containing box, such that $\int d\mathbf{r} = V$. This may then be evaluated to calculate the number density, n_T, as a function of μ.

$$n_T = \frac{N_T}{V} = \frac{1}{(2\pi\hbar)^3}\int_0^\infty \frac{1}{\exp\Big[(p^2/2m-\mu)/\mathrm{k}_BT\Big]-1}4\pi p^2 dp = \frac{1}{\lambda_T^3}g_{3/2}\Big[\exp(\mu/\mathrm{k}_BT)\Big], \quad (2.6.6)$$

where $\lambda_T = \sqrt{\frac{2\pi\hbar^2}{m\mathrm{k}_BT}}$ is thermal de Broglie wavelength. $g_{3/2}(z)$ is the 3/2 polylogarithmic function. This is positive and indicates that thermal atom density increases with increasing μ. However there is a limit, from the constraint $\mu < \epsilon_o$, for a trapped particle. This implies that, as N increases, the available excited states become saturated at some critical density, n_c which is given by,

$$n_c = \frac{N_c}{V} = \frac{\zeta(3/2)}{\lambda_T^3}. \quad (2.6.7)$$

Here, $\zeta(z)$ is the Reimann zeta function. All other atoms occupy the ground state, resulting in the observation of the BEC transition. The factor, $n\lambda_T^3$ is known as the phase space density of an atomic sample and the target of $\zeta(3/2) \approx 2.612$, as given by Einstein's theory, useful for the pioneering experiments aimed to realise this state. Eqn 2.6.7 may be reformulated, using the expression for de Broglie wavelength, to find the critical temperature for a given atomic density as to begin the transition,

$$\mathrm{k}_BT_c = \frac{2\pi\hbar^2}{m}\bigg(\frac{n}{\zeta(3/2)}\bigg). \quad (2.6.8)$$

Experimentally, systems are typically trapped in non-homogenous harmonic potentials such that,

$$V(\mathbf{r}) = \frac{1}{2}m(\omega_x^2x^2 + \omega_y^2y^2 + \omega_z^2z^2). \quad (2.6.9)$$

This equation describes a harmonic potential with trapping frequencies $\omega_i = 2\pi\nu_i$ and the new trapping potential results in a new critical density. This critical density is given by,

$$n_c(\mathbf{r}) = \frac{1}{\lambda_T^3}g_{3/2}\Bigg[\exp\bigg(-\frac{1}{2}\bigg\{\frac{x^2}{R_x^2} + \frac{y^2}{R_y^2} + \frac{z^2}{R_z^2}\bigg\}\bigg)\Bigg]. \quad (2.6.10)$$

The characteristic widths of this distribution, $R_i = \sqrt{\mathrm{k}_BT/m\omega_i^2}$, are known as thermal radii and indicates the extent of a thermal cloud, for a given temperature. The critical number is then found by performing an integral over the volume of the trap,

$$N_c = \zeta(3)\bigg(\frac{\mathrm{k}_BT}{\hbar\bar{\omega}}\bigg)^3. \quad (2.6.11)$$

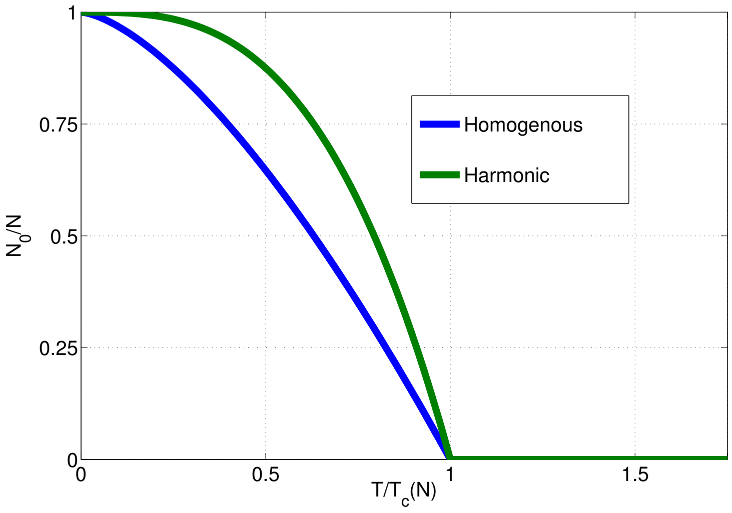

Figure 2.6.1: Plot of the condensate fraction for an arbitrary atomic sample showing differences in the homogenous and harmonic systems as a fraction of critical temperature.

With $\bar{\omega} = (\omega_x \omega_y \omega_z)^{1/3}$ the geometric mean trapping frequency. Similarly the critical point may be discussed in terms of a critical temperature T_c for a given atom number as,

$$\mathrm{k}_B T_c = \hbar \bar{\omega} \left(\frac{N}{\zeta(3)} \right)^{1/3}. \tag{2.6.12}$$

Using Eqn. (2.6.4) and Eqn. (2.6.12) the condensed fraction of an ideal atomic sample in a harmonic trap as a function of temperature may be given by,

$$\frac{N_0}{N} = 1 - \left(\frac{T}{T_c} \right)^3 \tag{2.6.13}$$

shown in Fig 2.6.1 compared to an expectation in a homogenous confinement, which has a 3/2 dependence.

2.6.4 The Bose-Einstein Condensate

The preceding section is an adequate description of thermal atoms of an ideal gas below the critical temperature but knowledge on the distribution and interactions of a condensate is more relevant to the experiment at hand. We first discuss the ideal (non-interacting) condensate, followed by the discussion of repulsive and attractive interactions and lastly briefly discuss dual species BECs.

Non-interacting Bose Gas

Considering the Bogoliubov approximation, we may treat a condensed Bose Gas as a classical field for which $\Psi_0 = \sqrt{N_0}\phi_0$, where ϕ_0 is the single-particle ground state wave function of the system. This is a solution to the Schrödinger equation,

$$\left(-\frac{\hbar^2\nabla^2}{2m} + V(\mathbf{r})\right)\Psi_0(\mathbf{r}) = \mu\Psi_0(\mathbf{r}). \tag{2.6.14}$$

Where μ replaces the usual energy term as the number of particles remains constant. For a harmonic potential, this is readily solved and yields a Gaussian wave function,

$$\Psi_0(\mathbf{r}) = \frac{\sqrt{N_0}}{\pi^{3/4}\bar{a}^{3/2}}\exp\left(-\frac{1}{2}\left\{\frac{x^2}{a_x^2} + \frac{y^2}{a_y^2} + \frac{z^2}{a_z^2}\right\}\right) \tag{2.6.15}$$

where $a_i = \sqrt{\hbar/m\omega_i}$ is the oscillator length along the i axis and $\bar{a}$ the geometric mean. The condensate density may then be directly calculated via,

$$n_0(\mathbf{r}) = |\Psi_0(\mathbf{r})|^2 = \frac{N_0}{\pi^{3/2}\bar{a}^3}\exp\left(-\left\{\frac{x^2}{a_x^2} + \frac{y^2}{a_y^2} + \frac{z^2}{a_z^2}\right\}\right). \tag{2.6.16}$$

Of particular significance, with this distribution equation, is that the characteristic length scale for an ideal condensate, $\bar{a}$, differs from the length scale of a thermal cloud, $\bar{R}$. In particular, thermal cloud radii are a factor of $(\zeta(3)/N_c)^{1/6}$ larger than the condensate. As a result, the spatial extent of the condensate is less than that of thermal cloud, yet can contain comparable numbers to the thermal component. When observing the BEC transition the two profiles are distinctly viewable in time-of-flight imaging, making it a useful element for quantifying the transition.

Interacting Bose Gas

While the presence of atomic interactions does complicate theory, it gives a wealth of potential applications for realising interesting phenomena in ultra cold atomic systems. Atoms in optical lattices, for example, may exploit the atomic interactions to transition from a superfluid to Mott insulator [35]. This is ideal for studying the dynamics of phase transitions and as a test bed for emulation of a variety of many-body system [132].

Consider N interacting atoms confined to a harmonic potential, V_{ext}, of the form given by

Eqn. (2.6.9). Using the second quantisation formalism, whereby many-body states are represented in the Fock state basis, the Hamiltonian of the system may be written as,

$$\tilde{H} = \int d\mathbf{r}\tilde{\Psi}_0^\dagger(\mathbf{r})\bigg(-\frac{\hbar^2}{2m}\nabla^2 + V_{ext} + \frac{1}{2}\tilde{\Psi}^\dagger(\mathbf{r}')V(\mathbf{r}-\mathbf{r}')\tilde{\Psi}(\mathbf{r}')\bigg)\tilde{\Psi}(\mathbf{r}). \tag{2.6.17}$$

Here $\tilde{\Psi}^\dagger$ and $\tilde{\Psi}$ are the boson field operators that create and annihilate particles at position $\mathbf{r}$ and $V(\mathbf{r}-\mathbf{r}')$ is the two-body interaction potential. In using only the two-body term it is assumed that temperatures are low and the atomic sample is dilute, which is a valid assumption for our system. As the interaction is weak it may be approximated as a mean-field interaction. As a result $V(\mathbf{r}-\mathbf{r}') = g\delta(\mathbf{r}-\mathbf{r}')$, with $g = \frac{4\pi\hbar^2 a_s}{m}$ is the coupling term governed by the s-wave scattering length a_s. This result is valid so long as $|n_0 a_s^3| << 1$ and $T << T_c$.

The time evolution of the operators may be given by using the Heisenberg equation such that,

$$i\hbar\frac{d\tilde{\Psi}(\mathbf{r},t)}{dt} = \Big[\tilde{\Psi}(\mathbf{r},t), \tilde{H}\Big] \tag{2.6.18}$$

If we impose the Bogoliubov approximation the field operator may be reduced to

$$\tilde{\Psi}(\mathbf{r},t) = \Psi_0(\mathbf{r},t) + \Phi(\mathbf{r},t). \tag{2.6.19}$$

Where Ψ_0 is the classical field representing the condensate wave function and $\Phi(\mathbf{r},t)$ excitation modes within the boson field. If we assume low temperature, this second term may be neglected and Eqn (2.6.18) substituted into Eqn (2.6.17) giving what is known as the Gross-Pitaevskii equation (GPE),

$$i\hbar\frac{d\Psi_0(\mathbf{r},t)}{dt} = \bigg[-\frac{\hbar^2\nabla^2}{2m} + V_{ext}(\mathbf{r}) + g|\Psi_0(\mathbf{r},t)|^2\bigg]\Psi_0(\mathbf{r},t). \tag{2.6.20}$$

This equation provides a very rich description of the behaviour of ultra-cold bosonic gases [75]. The ground state of a system may also be evaluated if we assume that the order parameter is separable such that,

$$\Psi_0(\mathbf{r},t) = \phi_0(\mathbf{r})\mathrm{exp}\bigg(-i\mu t/\hbar\bigg). \tag{2.6.21}$$

This reduces the GPE to,

$$\bigg(-\frac{\hbar^2\nabla^2}{2m} + V_{ext} + g|\phi_0(\mathbf{r},t)|^2\bigg)\phi_0(\mathbf{r}) = \mu\phi_0(\mathbf{r}). \tag{2.6.22}$$

This is a key tool for investigating the behaviour of non-uniform weakly interacting Bose gases exposed to some external potential.

Repulsive Interactions

A remarkable simplification to the Gross-Pitaevskii equation may be made that enables us to derive a particular expression for the ground state of the system, for repulsive particle interactions. Provided the trap exhibits no extreme anisotropy, the ratio of interaction and kinetic energy is given by,

$$N_0 \frac{a_s}{\bar{a}} >> 1. \tag{2.6.23}$$

This is satisfied under general experimental conditions and the Thomas-Fermi approximation, which enables the removal of the negligible kinetic energy term from Eqn 2.6.22, may be used to find that,

$$n_0(\mathbf{r}) = |\Psi_0(\mathbf{r})|^2 = \frac{\mu - V(\mathbf{r})}{g}. \tag{2.6.24}$$

It can be seen that the condensate density is different from the ideal case. Using the harmonic potential as before, the density distribution now becomes,

$$n_0(\mathbf{r}) = \frac{\mu}{g}\left(1 - \frac{x^2}{R_x^2} - \frac{y^2}{R_y^2} - \frac{z^2}{R_z^2}\right), \tag{2.6.25}$$

where the characteristic length scale $R_i = \sqrt{2\mu/m\omega_i^2}$ is the Thomas-Fermi radius at which the condensate density drops to zero along the i axis. This is an inverted parabolic shape that is larger in extent then the ideal case due to the presence of repulsive interactions. Despite the broadening of the BEC profile, the thermal cloud is still much broader and the transition readily observable in time of flight imaging. The relation between N_0 and μ may be found by integrating over the density profile n_0 to give,

$$N_0 = \frac{8\pi}{15}\frac{\mu}{g}\bar{R}^3. \tag{2.6.26}$$

Where $\bar{R} = (R_x R_y R_z)^{1/3}$ is the geometrical mean. This can be re-arranged for the Thomas-Fermi chemical potential in the form,

$$\mu = \frac{1}{2}\hbar\bar{\omega}\left(\frac{15 N_0 a_s}{\bar{a}}\right)^{2/5}. \tag{2.6.27}$$

Lastly the spatial extent of the cloud is given by the Thomas-Fermi radius in terms of N_0 as,

$$R = a\left(\frac{15 N_0 a_s}{a}\right)^{1/5}. \tag{2.6.28}$$

Under regular conditions the small size and high densities of a BEC usually do not allow direct observation of the condensate. However, when released from the trap, during the expansion, increases in the spatial extent and decrease in density enable it to be readily observed. In this release phase the residual energy of the sample is the driving force of its expansion. The rate at which it expands in a particular direction is directly proportional to the trapping frequency along this direction. As a result, for traps with large anisotropy between the z and perpendicular directions, such that $\omega_z/\omega_\perp << 1$, the size of the condensate along the perpendicular and z direction may be determined analytically as,

$$R_\perp(t) \simeq R_\perp(0)\sqrt{1+(\omega_\perp t)^2} \tag{2.6.29}$$

$$R_z(t) \simeq R_z(0)\left[1+\left(\frac{\omega_z}{\omega_\perp}\right)^2\left\{(\omega_\perp t) - ln\sqrt{1+(\omega_\perp t)^2}\right\}\right] \tag{2.6.30}$$

While this is a special case for highly anisotropic trapping geometries the basic elements are qualitatively important for a variety of traps. It can be seen that the tight direction expands much more rapidly than the weak resulting in a inversion of the trap aspect ratio for sufficiently long expansion times. This is yet another signature of a condensate that also enables calculation of the mean field energy of trapped atoms.

Condensate mixtures

The previous sections have discussed the properties describing single-species condensate. This thesis is concerned with designing and moving towards a dual-species system and the physics of BEC mixtures should be touched upon. Atomic mixtures are not new but demonstrate rich physics including collective oscillations [136] and the miscible to immiscible phase transition [137, 138]. Further control, over the interaction between species, has been proposed to allow observation of nonlinear Josephson-type oscillations [139], as well for use as a quantum computer [140]. They have also displayed increased sensitivity for metrology with squeezing [66]. These are all a direct results of the physical richness multi-species condensates offer. Here we concern ourselves with a dual-species condensate, which adds another interaction term to the GPE equation to enhance our parameter space.

Assuming short-range interactions, coupled Gross-Pitaevskii equations may accurately describe a dual-component condensate,

$$\left(L_1(\mathbf{r}) + g_{11}|\psi_1|^2(\mathbf{r}) + g_{12}|\psi_2|^2(\mathbf{r})\right)\psi_1 = \mu_1\psi_1(\mathbf{r}), \tag{2.6.31}$$

$$\left(L_2(\mathbf{r}) + g_{22}|\psi_1|^2(\mathbf{r}) + g_{12}|\psi_1|^2(\mathbf{r})\right)\psi_2 = \mu_2\psi_2(\mathbf{r}). \tag{2.6.32}$$

Here $L_i = -\frac{\hbar^2\nabla^2}{2m_i} + V_{ext,i}(\mathbf{r})$ and $g_{ii} = 4\pi\hbar^2 a_{ii}/m_i$ is the intra-species coupling constant that describes self-scattering processes of the i^{th} atomic sample while g_{12} describes the degree of scattering events between the two different species. Here we assume that $g_{11}, g_{22} > 0$ such that individual species are stable and then we may look at the ground state of the system. As the drive of the experiment is towards a near-homogenous trapping potential we limit the discussion to mixtures in a homogenous trap. From mean-field theory, the interaction energy between the species may be calculated as,

$$E_{int}(\mathbf{r}) = \frac{1}{2}\left(g_{11}n_1^2(\mathbf{r}) + g_{22}n_2^2 + 2g_{12}n_1(\mathbf{r})n_2(\mathbf{r})\right), \tag{2.6.33}$$

with $n_i = |\psi_i|^2$ the density of the i^{th} component. The interspecies scattering length, $g_{12} = 2\pi\hbar^2 a_{12}/m_{12}$ where $m_{12} = \left(\frac{1}{m_1} + \frac{1}{m_2}\right)^{-1}$ is the reduced mass of the two species. Considering a miscible system, such that the two species may freely 'mix' and fill the box of volume V with N atoms, of each species, then the interaction energy becomes,

$$E_{mix} = \frac{N^2}{2V}(g_{11} + g_{22} + 2g_{12}). \tag{2.6.34}$$

Alternatively if they are separated into volumes V_1 and V_2, then the total mean-field becomes

$$E_{sep} = \frac{N^2}{2}\left(\frac{g_{11}}{V_1} + \frac{g_{22}}{V_2}\right) \tag{2.6.35}$$

Using $V_2 = V - V_1$ and setting $dE_{sep}/dV_1 = 0$ it is found that $V_1/V = (g_{11} - \sqrt{g_{11}g_{22}})/(g_{11} + g_{22})$ such that the separated energy becomes,

$$E_{sep} = \frac{N^2}{2V}(g_{11} + 2\sqrt{g_{11}g_{22}} + g_{22}). \tag{2.6.36}$$

As can be seen, depending on the magnitude of g_{12} energy is minimised by either having the atoms miscible or have distinct regions of a single species. When $g_{12} > \sqrt{g_{11}g_{22}}$ the two species will be immiscible and attempt to spatially separate from one another. Interestingly, the interspecies scattering length a_{12}, and subsequently g_{12}, is readily tuneable for ^{87}Rb and ^{41}K clouds that are prepared in the $|F = 1, m_F = 1\rangle$ state via Feshbach resonances, discussed in section 2.7. This is an important feature of our system and influenced the design 'pathway' towards quantum degeneracy.

2.7 Ultracold Atomic Scattering

Binary scattering events are the main types of collisions in dilute, ultra cold gases. The strength of this can sometimes be controlled by Feshbach resonances. In the dilute gas regime, as in the experiment of this work, the dominant scattering process are two-body and three-body collisions, in which the particles interact via van der Waals forces, electrostatic repulsion and exchange interactions. Under certain circumstances, these may be tuned for both the inter and intra scattering of cold mixtures. Here we provide a brief overview of collisions in the low-temperature regime and Feshbach resonances.

2.7.1 Elastic collisions and Feshbach resonances

For indistinguishable particles the probability of a scattering event is quantified by the elastic collision cross-section, σ given by,

$$\sigma = \frac{8\pi a^2}{1 + k^2 a^2}, \tag{2.7.1}$$

where $k = \frac{2\pi}{\lambda}$, with λ the de Broglie wavelength of the colliding particles. As previously mentioned a refers to the characteristic length scale of the scattering process, referred to as the s-wave scattering length. This is, typically, on the order of several nanometers for bosonic alkali atoms. Once temperatures are sufficiently low this becomes independent of energy and reduces to $\sigma = 8\pi a^2$ and is equivalent the cross section of a hard sphere with radius a. In binary elastic collisions there is no change in the internal state, which make it ideal for being the mediator for evaporative and/or sympathetic cooling. The scattering length has little effect on the properties of a thermal gas but a large impact on the properties of a Bose-Einstein condensate.

Inelastic collisions, on the other hand, allow the consideration of internal states of the atoms. For cold samples, in which the average thermal energy per particle is much less then the separation between internal states, such collisions typically result in heating and loss from a trapped atom cloud. However, it is the existence of this internal structure that enable control of collisional interactions.

Qualitatively, in a two-body collision, open and closed channels refer to the collection of quantum states in which particles are allowed or forbidden to emerge from a scattering event due to energy conservation arguments. An open channel is one whereby any channel has less or equal energy E relative to the total energy of the system $E_{tot} = E_1 + E_2 + E_k$, Fig 2.7.1 (left), where $E_{1,2}$ are the internal energies of the particles, and E_k their relative kinetic energies. Any channel that possesses more energy is closed. However it is known that scattering potentials exhibit a resonant behaviour when a bound state (molecular) exists between the colliding particles. The presence of this molecular state may dramatically modify the atomic scattering length via Feshbach resonances [63, 141].

Interestingly this coupling, in a two-body collision, of the bound state in a closed channel can be tuned under certain circumstances. For alkali atoms different hyperfine states may have different magnetic moments and quantum numbers, thereby responding differently to applied magnetic fields. When an appropriate field is applied a bound state may be brought close to the interaction energy of the particles. They may then, briefly, scatter to the intermediate closed channel before decaying into the open channel this changing the scattering interaction strength about the Feshbach resonance. The change in scattering length by an external field is given by:

$$a = a_{bg}(1 - \frac{\delta}{B - B_0}), \tag{2.7.2}$$

where B_0 is the resonant field, δ the width of the resonances and a_{bg} the s-wave scattering length in absence any applied magnetic field. Due to the complexity of various contributions from several closed channels the determination of the location and width of these resonances are often left to be found experimentally. Fig 2.7.1 (right) shows two magnetic Feshbach resonances between ^{87}Rb and ^{41}K prepared in the $|F, m_F\rangle = |1, 1\rangle$ state. These are important for phase separation experiments, enabling us to readily tune the system across the miscible and immiscible transition. An extensive overview of Feshbach resonance physics may be found in [63].

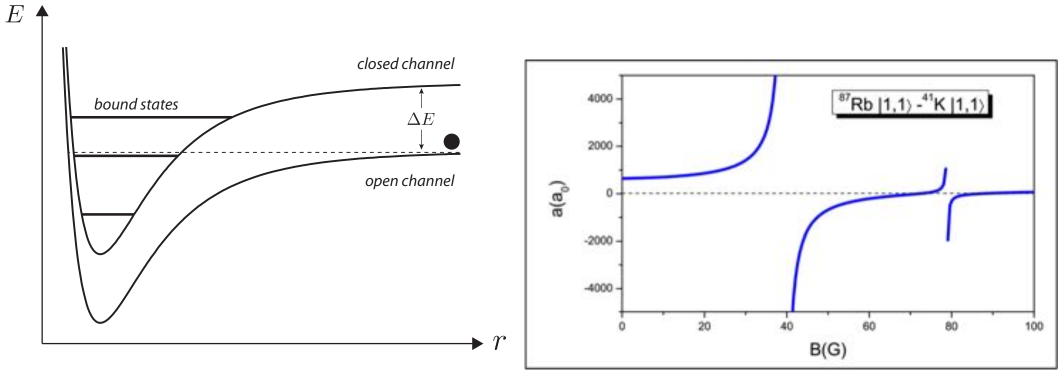

Figure 2.7.1: (Left) - A depiction of open and closed channels, corresponding to allowable and forbidden internal state transitions. In the presence of an allowable bound (molecular) state the scattering potential is greatly altered, adapted from [156]. (Right) A magnetic Feshbach resonance between ^{87}Rb and ^{41}K in the $|F, m_F\rangle = |1, 1\rangle$ state as the differing hyperfine states between the colliding and bound state may allow the molecular state to be tuned closer, image from [79]. The 40 G resonances is particular interesting as it is experimentally obtainable and broad allowing large tuneability.

2.8 Imaging

Having the capability to trap, cool, evaporate and manipulate is worth little if you cannot observe the cloud in order to gain quantitative and/or meaningful data. This is done by imaging the cloud, with a variety of techniques possible to do so. Here a brief overview of the current state of the art in imaging of ultra atomic gases and theory required to understand data collected is presented.

Their exist many imaging techniques, including absorption, fluorescence, scanning electron microscopy, phase contrast and dark ground imaging (to list a few), for probing and understanding Bose Einstein condensates. Here the measure for success is the atom number and spatial resolution achievable. In this regard, fluorescence has emerged as the front runner, having achieved single atom detection [142, 143, 144], at high resolutions. This method is technically difficult, in comparison to other imaging schemes and only applicable in deep optical traps. Furthermore, the measurement itself is a parity measurement for site occupation and not the actual number distribution due to light-assisted collisions. This means a ‘true’ image is only available when a single atom is confined to a single trap site [144]. An alternate approach, is applying scanning electron microscopy to ultra cold gases, enabling a resolution down to 150 nm, well below any optical based method [145]. Unfortunately this technique suffers from poor efficiency, relying on collection of ionised particles after collisions between the electrons and the ensemble. While these methods are impressive, such performance is not always necessary. Further, these are technically demanding imaging methods when compared to the simplicity of absorption imaging.

Absorption imaging, arguably the simplest method and perhaps the most robust, has recently moved forward demonstrating a number resolution down to 3.7 atoms [20]. This represents the method of choice for imaging in this experiment.

2.8.1 Absorption Imaging and Thermal Clouds

Absorption imaging is the primary diagnostic tool for probing the ultra-cold atomic clouds in our system. By passing a beam of near-resonant light through the atomic ensemble, absorption by the atoms casts a shadow that can be analysed. In particular a probe beam, with intensity profile $I_0(x, y)$, propagating along the z-axis and passed through an atomic sample of density $n(x, y, z)$ is attenuated as given by the Beer-Lambert law,

$$\frac{dI}{dz} = -naI. \tag{2.8.1}$$

where a is the atomic cross-section for a closed transition,

$$a = \frac{3\lambda^2}{2\pi}\frac{1}{1 + 4(\Delta/\Gamma)^2 + I/I_{sat}}. \tag{2.8.2}$$

With I_{sat} and Γ the saturation intensity and natural line width of the imaging transition, and I and Δ are the intensity and detuning of the imaging light. To obtain a useful expression we integrate Eqn. (2.8.1), to show:

$$n(x, y) = \frac{2\pi}{3\lambda^2}\left[\frac{I_0(x, y) - I_F(x, y)}{I_{sat}} + [1 + 4(\Delta/\Gamma)^2]\ln(\frac{I_0(x, y)}{I_F(x, y)})\right] \tag{2.8.3}$$

Where $I_F(x, y)$ is the intensity profile of the attenuated beam. If the incident light is below the saturation limit, $I_0(x, y)dxdy << I_{sat}$, then the two-dimensional density profile may neglect the first term and Eqn. (2.8.3) reduced to,

$$n(x, z) = \frac{2\pi}{3\lambda^2}\frac{\Gamma^2 + 4\Delta^2}{\Gamma^2}\ln\frac{I_0(x, y)}{I_F(x, y)}. \tag{2.8.4}$$

Under these conditions the column density is determined only by the ratio of absorbed and incident light, requires no knowledge of the absolute power the atoms interact with. Detection efficiencies and calibrations are not explicitly required for accurate atom distribution properties.

The size, temperature and phase-space densities of an atomic cloud can be determined from the column density distribution $n(x, y)$. A fast method for extracting atom number is the integration of the optical density (OD) of the absorption profile. The OD can be found by taking the negative logarithm of the fractional transmission of a probe beam through an atomic cloud,

$$OD(x, y) = \sigma \int n(x, y, z)dz = -\ln(\frac{I_0(x, y)}{I_F(x, y)}). \tag{2.8.5}$$

The optical density can be used to find the total atom number, found by integrating over the imaging area.

$$N = \int n(x, y, z)dxdydz = \frac{1}{\sigma} \int \int OD(x, y)dxdy. \tag{2.8.6}$$

As images are taken via a CCD absorption spectra are discretised, thus the integral for atom number becomes a summation over the array. In order for more accurate atom numbers, another image is taken that records background light levels while also aiding in cancelling dark-current noise. This is known as the dark image, I_D, and is subtracted from the absorbed and imaging profile such that,

$$OD(x, y) = -\ln(\frac{I_0(x, y) - I_D(x, y)}{I_F(x, y) - I_D x, y}). \tag{2.8.7}$$

Alternatively, atom number and temperature can be determined by fitting the image of the cloud with the expected density profile, as determined by the type of trap the atom sits within. Due to Zeeman shifts and the small size of in-situ images, atoms are usually released from the trap and allowed to expand before an image is taken. A thermal cloud is well described, when released from a harmonic trap, by a Gaussian such that,

$$n(x, y) = A\text{exp}\bigg(- \frac{(x - x_0)^2}{2\sigma_\perp^2} - \frac{(y - y_0)^2}{2\sigma_y} \bigg) + B, \tag{2.8.8}$$

where $A = \sigma \frac{N}{2\pi\sigma_\perp\sigma_y}$. By fitting the six parameter Gaussian to the cloud, determination of the atom number and size distribution of the cloud is made possible. Generally a 2D fit over a CCD array is computationally long and we instead elect to fit two different 1D Gaussians across two orthogonal line profiles. Thus $\sigma_\perp$ and σ_y can be found for meaningful data extraction. Temperature may be calculated from a single in-situ measurement, however, the optical densities are typically too high and in order to take useful data we make use of time-of-flight (TOF) imaging. In TOF imaging the trapped atoms are allowed to expand ballistically, for a time t, before an image is taken. The density profiles remain Gaussian with the characteristic length scales of the cloud, $\sigma = \{\sigma_\perp, \sigma_y\}$, evolving as,

$$\sigma^2(t) = \sigma^2(0) + t^2\sigma_v^2 \tag{2.8.9}$$

Where $\sigma_0 = \sqrt{(2\mathrm{k}_B T/m)}$ is the characteristic width of the atoms within the trapping potential. By taking two images at different times the temperature can then be extracted from the cloud width at the two points τ,

$$T = \frac{m}{2\mathrm{k}_b}\frac{\sigma^2(t_2) - \sigma^2(t_1)}{t_2^2 - t_1^2}. \tag{2.8.10}$$

Alternatively when the trap frequencies are known the temperature can be calculated from a single width distribution via,

$$T = \frac{m\sigma^2(t)\omega^2}{2\mathrm{k}_B(1 + t^2\omega^2)}. \tag{2.8.11}$$

2.8.2 Imaging condensates

When the temperature of an atomic sample, confined to a harmonic potential, is lowered below the critical temperature a Bose-Einstein condensate begins to emerge. This manifests as a narrow peak in the phase space density, with a spatial extent smaller than that of thermal profile. This represents the condensed fraction of the cloud, described by the Thomas-Fermi function. The three-dimensional, and column, density profile of the condensate is then given by,

$$n(x, y, z) = \frac{15N}{8\pi R_\perp^2 R_z}\left(1 - \frac{(x - x_0)^2 + (y - y_0)^2}{R_\perp^2} - \frac{(z - z_0)^2}{R_z^2}\right) \tag{2.8.12}$$

$$n(x, y) = \frac{5N}{2\pi R_\perp R_z}\left(1 - \frac{(x - x_0)^2}{R_\perp^2} - \frac{(z - z_0)^2}{R_z^2}\right)^{3/2}. \tag{2.8.13}$$

Where R_i are the Thomas-Fermi radiuses of the distribution. With the addition of an offset term, the fitting function of the optical density for the condensed cloud is then Eqn 2.8.13. At intermediate temperatures, around the critical temperature, a condensate is not pure and a bimodal function is used as the fit. This bimodal function is simply the sum of Eqn 2.8.13 and Eqn 2.8.8. The condensed atom number may be obtained from,

$$N = \frac{8\pi}{1.5 \times 10^4} R_\perp^2 R_z A, \tag{2.8.14}$$

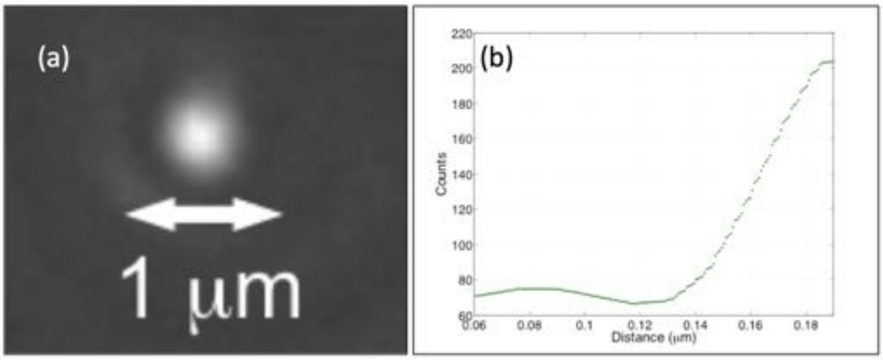

Figure 2.8.1: Point spread function of a digital point source after it has been minimised and reimaged. The FWHM of the first system is imaged and measured to be 650 nm within 7 % of theoretical best value at 532 nm. Image taken with imaging system of the experiment.

Where $A = \frac{5N}{2\pi R_\perp R_z}$.

In summary, the imaging of atomic clouds allows one to quantify the temperature, number and spatial distributions of trapped atomic vapours. Further, one can directly observe the emergence of a Bose-Einstein condensate by looking for a narrow incongruity with thermal distribution.

2.8.3 Imaging resolution

Due to finite aperture size, an imaging system can only reproduce a limited range of spatial frequencies of an object. As these imaging systems are linear, however, the limit is well characterised by its response to a point source, known as the point spread function (PSF) Fig.(2.8.1). This has the form of an Airy pattern whose extent is determined by the incident wavelength and numeral aperture of the system. The intensity distribution, of the PSF, is given by,

$$I(\rho) = \left(\frac{2J_1(\rho)}{\rho}\right)^2. \tag{2.8.15}$$

Where $J_1(\rho)$ is the Bessel function of first order and $\rho = r \cdot 3.795/r_0$ is the radial distance r scaled by the resolution r_0. Resolution of the system is defined by the point were the first zero $I(\rho)$ and given by $r_0 = 1.22 \cdot \lambda/(2\text{NA})$. An example of a PSF, showing the Bessel function nature, is shown in Fig. (2.8.1).

Chapter 3

The Apparatus

The construction of a fully operational apparatus that can reliably create, control and image Bose-Einstein condensates was the main focus of my project. Despite advances and global knowledge of BEC machines it typically takes new groups several years to reach the point of producing novel experimental data. This chapter provides the particulars of our experimental methods and infrastructure towards our ^{87}Rb and ^{41}K BEC apparatus. In particular the design, construction and basic performance of the vacuum system, necessary for isolation from the environment, laser system, required for the cooling, trapping and manipulation of atomic vapour, and the magnetic coil infrastructure are presented. Each of these are addressed in detail in this chapter. However, a technical summary is presented first.

The system consists of two chambers, the high-vacuum (HV) side, sitting at 1×10^{-7} mBar, and the ultra-high-vacuum side (UHV), at $< 10^{-10}$ mBar. Within the HV section, cold atomic beams of ^{87}Rb and/or ^{41}K , are produced by a 2D-MOT before being sent into the UHV side through a small aperture. This collimated beam of cold atoms is then collected and held in a glass octagonal chamber in the 3D-MOT. Currently, atomic clouds of ^{87}Rb and ^{41}K can be simultaneously, and independently, produced. The remainder of the pathway to BEC is established only for ^{87}Rb.

Approximately 60 % of ^{87}Rb atoms, caught in the 3D-MOT, are recaptured in the magnetic quadrupole trap before being transported to another region in the UHV side of the apparatus. This is a small glass chamber, termed the science cell, is fused to the octagon. This is done via a transfer sequence conducted by consecutively alternating the current passing through three pairs of electromagnets. Transfer to the science cell is necessary in order to provide high optical, and close physical, access to the atomic cloud. This is necessary for the use of high-resolution commercial imaging microscopes close to the cloud, while also enabling ample space for interacting with the atomic cloud with a variety of optical beams. Microwave evaporation then produces a much colder, and therefore smaller, atom cloud. This is matched, in terms of spatial mode, for loading into a single-beam dipole trap. In the future, this step will also cool ^{41}K via sympathetic cooling techniques. Emergence of a Bose Einstein condensate occurs as the cloud is optically evaporated following a successful load into the hybrid trap.

At the completion of my time within the laboratory we were able to routinely collect more than 2×10^9 ^{87}Rb atoms in the 3D-MOT that would be result in $\approx 2 \times 10^5$ atoms in the BEC. This represents a strong starting point and it is anticipated that, with sufficient optimisation, the number of condensed rubidium atoms will be greater than 10^6. Independently, or simultaneously, we were also able to capture ^{41}K in the 3D-MOTs. Potassium is yet to be condensed as ^{87}Rb was used as a test species to benchmark and troubleshoot the apparatus. This is due to the fact that techniques are better established with rubidium than potassium, and therefore we didn't have to concern ourselves with working with comparatively small atom number clouds and potential issues arising from inter-species interactions.

In order to reach this point the entire apparatus had to be designed, constructed, built and tested from the base up. In this chapter the main infrastructure is described, detailing the key elements that make up the backbone of the apparatus including the vacuum system, laser sources, optics and delivery and coil system, that took form in the first year of this project.

3.1 Vacuum System

A pristine vacuum environment is essential for all cold-atom experiments that require long trap lifetimes. Collisions with background gas particles, which have energies many orders of magnitude above trapped atoms, cause significant losses and heating which can impede evaporative cooling and limit the lifetime of a trapped atomic cloud. In the worst case scenario, these background losses will preclude emergence of a Bose-Einstein condensate. Even background vapour, which may serve to feed a BEC, can create severe limitations on the lifetime of trapped atomic clouds. As an example, background vapour may cause decoherence of carefully prepared quantum states leading to spurious phase shifts in the output of atom interferometers [66]. To prevent this, background collisions must be minimised.

Another key design element is the amount of physical access an experimenter has to address a trapped cloud. The variety of cooling, trapping, and imaging beams required, and considerations for magnetic coil infrastructure, makes it advantageous to create a multi-chamber system. In particular, the multiple chambers enable additional infrastructure to continually be added to the system. Further, it allows for a pressure differential throughout the system to mitigate background collisional losses. Our differentially pumped system enables the main experimental chamber, where evaporation to BEC is performed, to be kept at ultra high vacuum (UHV) pressures ($< 10^{-10}$ mBar) while allowing the atomic source region to have relatively high alkali vapour pressures ($\simeq 10^{-7}$ mBar), necessary for trapping large numbers of atoms. In our system we produce a low-velocity atomic beam from background vapour in the 2D-MOT chamber, Fig. (3.1.1), that is forced through a differential tube into the UHV section that serves as our main experimental chamber.

3.1.1 Overview

A schematic of our vacuum apparatus is shown in Fig (3.1.1). The majority of the system is constructed from commercial ultra-high vacuum components. These are of the conflat (CF) variety, sealed by single use copper gaskets via compression with knife edges. A custom designed 3D-MOT chamber, with adjoining science cell, was made by Precision Glass Blowing, while the 2D-MOT chamber was constructed in-house by the mechanical workshop. A 6-way cube separates these two regions. Vertically a NEXTorr D 200-5 ion pump, with integrated hybrid non-evaporable getter (NEG), is mounted to the cube via a conical nipple connected to a large ion-pump mounting flange. The 8 L/s ion pump removes noble-gas loads, and an effective pumping speed of 200 L/s is achieved with the NEG element. On the underside of the 6-way cube a 90° flange is connected to an all metal valve, which was permanently closed once the ion pump and NEG element were activated. The remaining two sides consist of 'windows' that allow optical access into the vacuum chamber. The 3D-MOT chamber is connected to the cube by the way of adjustable bellows and a rotatable conflat flange.

The 2D-MOT side consists of a custom-made chamber, connected to the 6-way cube via the differential tube, Section 3.1.3. This is a long aperture that creates a pressure gradient across the two regions of the experiments. The back end connects to a 5-way cross. Vertically mounted off the cross is 'T' flange which has another all metal valve and Gamma-Vacuum TiTan 105 ion pump, pumping at 10 L/s. Electrical feed throughs are attached to either side of the cross that connect to the internally connected atomic dispensers. These dispensers supply the system with the atomic vapour of ^{87}Rb and ^{41}K when required. A second 3-way cross is attached

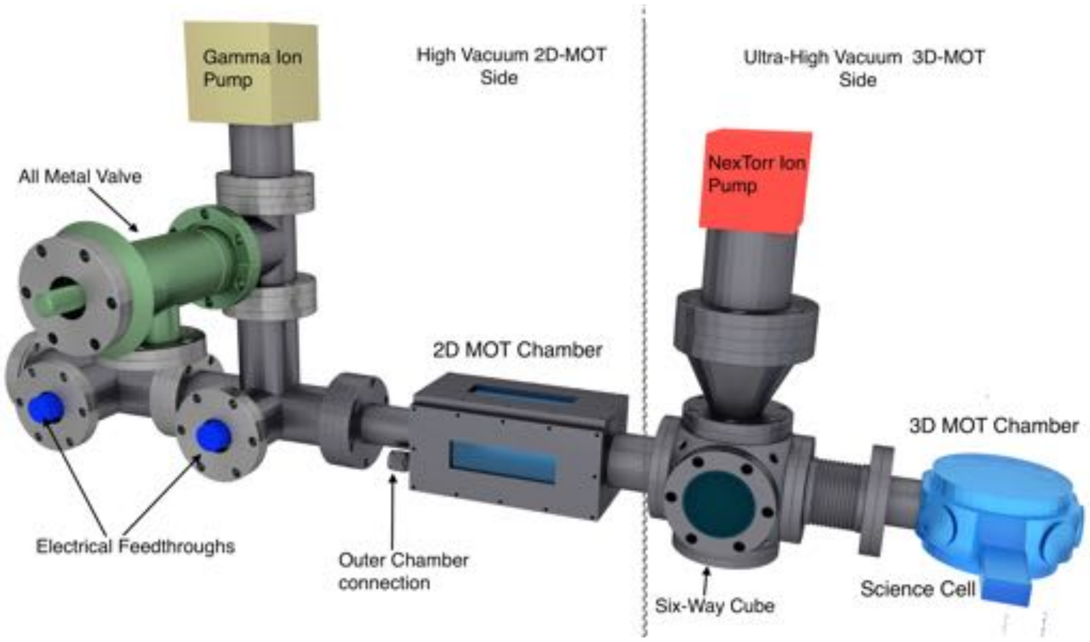

Figure 3.1.1: Render of the full vacuum system, which comprises the main component of the apparatus. The key elements of the system are shown indicating the difference between the sides of the 2D-MOT and 3D-MOT of the chamber. These are separated internally by a low conductance differential pumping tube. A description of each element is provided in the main text.

with additional electrical feed throughs mounted on the side. The back face consists of an AR coated window enabling optical access. In the following section, the key elements of the vacuum system are discussed. This includes the differential pumping mechanism, 3D-MOT and 2D-MOT chamber and bake out procedure.

3.1.2 Differential Pumping

In order to create the ideal environment for our trapped atomics gases a pressure differential of two or three orders of magnitude, between the 2D-MOT and 3D-MOT chambers, a two-stage differential pumping set up was designed. A simplified diagram of how we achieve this is shown in Fig. (3.1.2). The two key regions of the system, the 3D-MOT and 2D-MOT chambers are connected to their respective pumps, with speeds S_1 and S_2 L^{-1}. The pumps are separated from the main chamber, of each distinct region where P_1 & P_2 are labelled, by adjoining elements, with conductance C_1 and C_2. This limits the pumping speed at these points, resulting at an effective pumping speeds are S_1^* and S_2^*, where $1/S^* = 1/S + 1/C$ across the differential tube.

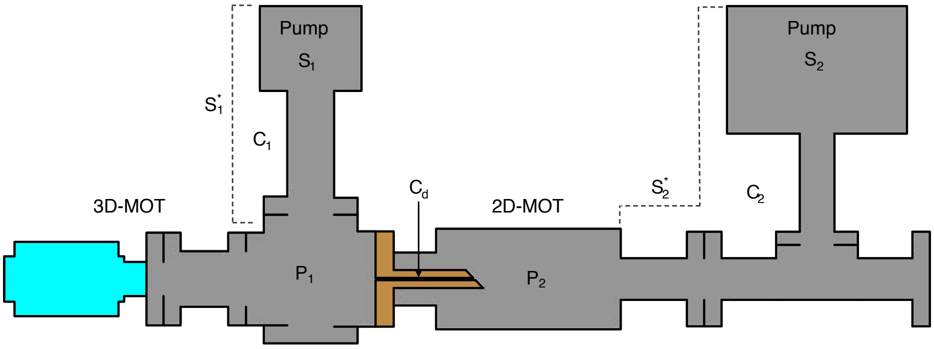

Figure 3.1.2: Cross-section of the vacuum system showing the differential pumping arrangement provided by the low conductance element C_d.

This copper tube, separating the 2D and 3D-MOT chambers, is a custom made copper tube with conductance C_{d}. This creates a pressure differential across the two, given by,

$$\frac{P_2}{P_1} = 1 + \frac{S_1^* - S_2^*}{C_{\mathrm{d}}} \simeq \frac{S_1^* - S_2^*}{C_{\mathrm{d}}}. \tag{3.1.1}$$

The conductance of each cylindrical vacuum piece is given by,

$$C = \frac{\pi}{6}\sqrt{\frac{2\mathrm{k}_B T}{m\pi}}\frac{D^3}{L}. \tag{3.1.2}$$

Where D is the diameter of the tube and L its length. Here, $S_1 = 200$ L/s and $S_2 = 10$ L/s, while the effective pump speed is $S_1^* = 75$ L/s and $S_2^* = 5$ L/s, due to limited conductance C_1 and C_2. The bored hole in the differential tube is a 12 mm long, 1.2 mm diameter hole with conductance $C_{\mathrm{d}} = 0.016$ L/s. Using these values the expected pressure differential is given as $P_2/P_1 \simeq 1200$. Additionally, any atoms that pass through the tube must have a certain trajectory lest it interact with the walls of the tube. This means that any atom sent from the 2D-MOT to the 3D-MOT is well matched to the 3D-MOT capture range.

As a differential pumping scheme consists distinct pressure regions, it is instructive to discuss their design and construction individually. First we present the custom designed and constructed 2D-MOT chamber, where background vapour supplies the 3D-MOT, and then discuss the 3D-MOT chamber.

3.1.3 2D-MOT chamber

The 2D-MOT chamber is where a background gas is cooled, in two dimensions, to produce a collimated beam of atoms that are captured in the main experimental chamber. These cold atomic beams are not only relevant to ultra cold atom experiments, but also have a wide variety of significance in a variety of other applications, including atom optics [146] and QED cavities [147]. Regarding the production of intense atom beams, Zeeman slowers [148] are still widely used to obtain a high flux of atoms. Alternate methods, such as low-velocity intense source MOTs [149] are also used. Here we have elected to construct a chamber for use as a two-dimensional MOT which enables the use of relatively low laser power, low atomic vapour pressure and moderate infrastructure to produce our cold atom beams [150, 151, 152]. A 2D-MOT operates by cooling atoms in two-directions while a combination of the longitudinal thermal motion and an additional push beam, forces atoms to move along this direction. Passing them through a suitable aperture, the divergence of the beam can be controlled. A more detailed explanation is provided in section 4.1.1.

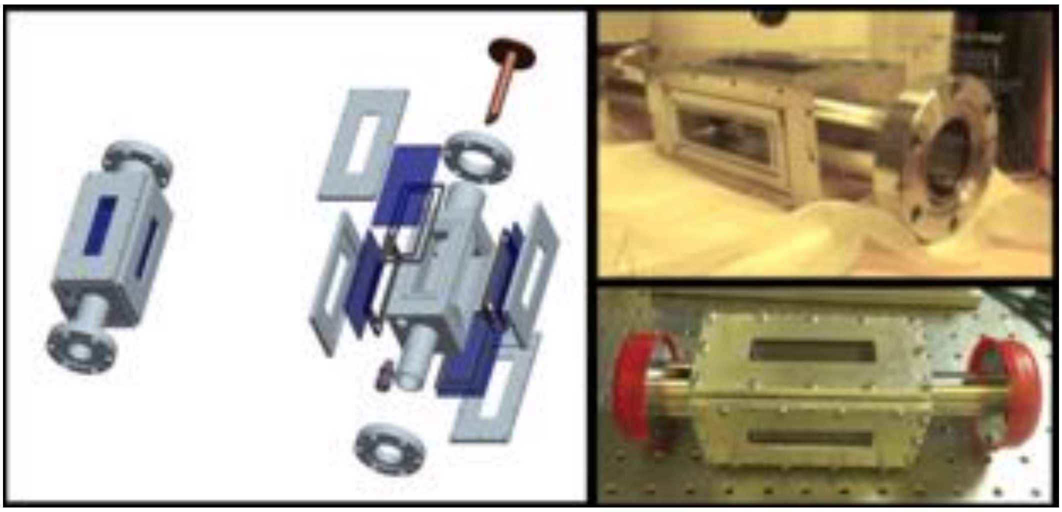

Figure 3.1.3: 2D-MOT chamber of the vacuum system prior to assembly. Left - render of the assembled and exploded components of the 2D-MOT chamber, illustrating the double o-ring vacuum configuration and attachment points. Right - Actual chamber before and after assembly.

Originally the 2D-MOT chamber was an all-glass custom made piece. However, upon initial assembly it was damaged and a new metal chamber was designed and constructed, Fig (3.1.3). The design itself avoided the use of UHV glues and metal seals to increase reliability. It consists of a machined stainless steel cuboid chamber, with CF flanges welded to the ends. The inner chamber is 62 × 21 × 75 mm, with 20 × 75 × 3 mm windowed regions to allow optical access. This window size was chosen as it matches the 2D-MOT beam extent as originally designed for the defunct all-glass chamber. The windows themselves are BK7 glass, not AR coated, and held onto the main chamber by M3 screws. A vacuum seal is provided by custom made Viton O-rings recessed into milled grooves, Fig (3.1.3). Shown in the figure are the existences of two separate, rectangular, O-rings that seal an inner and outer volume respectively. This produces two nested vacuums, with the outer limiting permeation of atmospheric gases through the inner o-ring and into the main chamber. This allows realisation of UHV pressures with Viton seals [153]. The recess, which provides the sealing point for the O-rings, was milled with angled grooves. A standard, rectangular milled groove would have resulted in micro-channels that extend across the o-ring, creating a vacuum leak. Angled channels, when correctly milled, make a seal with the Viton through which these channels are not present. A standard threaded screw-in 10 mm tube adapter provides a port to vacate the outer vacuum region. This is viewable in the exploded view of the 2D-MOT chamber in Fig (3.1.3). Additionally the double Viton seal illustrates the space of the outer chamber, connected to one another by screw holes to each of the four faces. To prevent atmospheric gas permeation, this outer volume must be periodically pumped down. A small diaphragm pump automatically pumps down this part of the system each night. A dimensioned image of the 2D-MOT outer chamber is given in Fig (3.1.4).

Several other important aspects of the system are housed with the 2D-MOT chamber. First, a five-way cross connects two electrical feed through elements and a T-piece that adds an all metal valve and the Gamma-Vacuum TiTan 105 10 L/s ion pump. Another T is attached, to the final port of the cross, for an additional electrical feed through point and optical viewport, Fig (3.1.4) (top). The ion pump is held at 65 °C to prevent arcing from the alkali deposition. The electrical feed throughs allow external connection to the internally mounted vapour sources. The vapour sources are SAES alkali metal dispensers, containing ^{87}Rb and ^{41}K, in their naturally occurring isotope mixtures. In total nine sources are currently installed in our vacuum chamber, 5 for potassium and 4 for rubidium. These must be thermally activated to expel contaminants, before bringing the system down to its terminal pressure, to ensure their proper operation and reduce chance of contaminating the system. The electrical feed throughs allow current to be passed through these dispensers that heat the sources contained within. This causes a reduction reaction to expel a pure gas sample into the chamber. These dispensers are operated in one of two ways. These are either continuously run at a low current (4 A) or via flashing (6 A) for 1 min every hour).

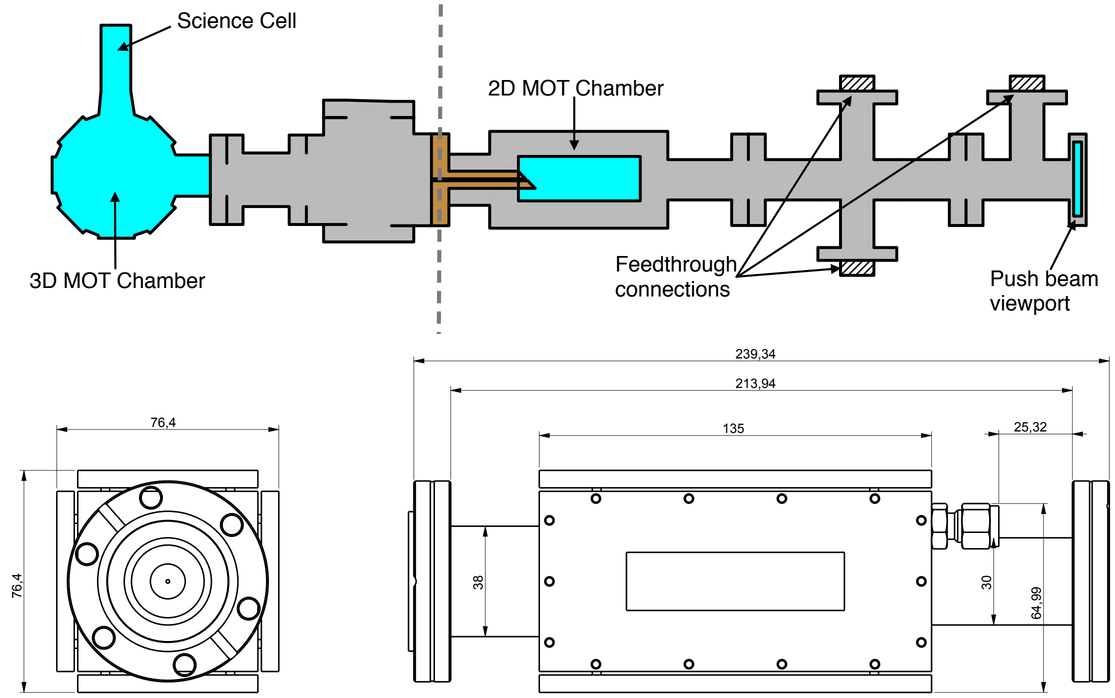

Figure 3.1.4: Top - Birds eye cross-sectional view of the vacuum apparatus. Indicating the key areas of the 2D-MOT side. The 2D-MOT chamber connects to a five-way cross that connects to two electrical feed through connection points. Another feed through is provided at the 'T' point. Optical access is provided by the rear viewport at the back of the system. The ion pumps (not shown) extend out of the page. Bottom - Dimensioned schematic of the two-dimensional MOT chamber, all dimensions in mm.

3.1.4 3D-MOT Chamber

The bulk of the experimental procedure, to create a BEC, of ^{87}Rb, is carried out in the main experimental chamber, known as the 3D-MOT chamber. In order to have a successful and versatile experiment, this region must satisfy several criteria. The 3D-MOT must have sufficient optical access for three orthogonal cooling and trapping beams. Similar access is required, following initial trapping in the 3D-MOT, to continue to pathway to condensation and have ability to manipulate and image atoms in the science cell. The glass components must be designed with consideration to the other infrastructure required, including quadrupole coils, imaging beams and other manipulation elements. Here we optimised our design to allow close physical access to the cloud at the science chamber for high-resolution imaging.

The 3D-MOT chamber is a custom glass piece, with a glass to CF flange transition, designed in-house and manufactured by Precision Glass Blowing, Fig (3.1.5). A quartz octagonal cell

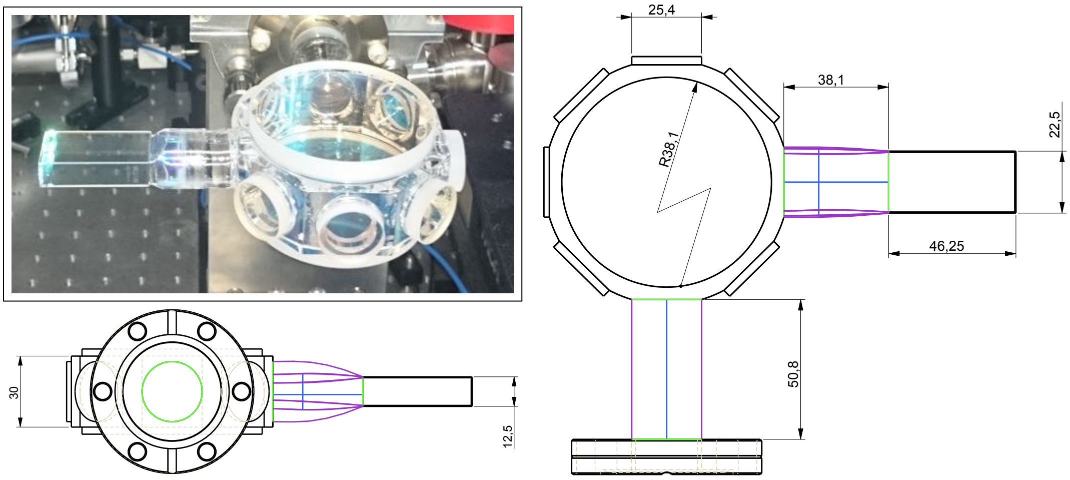

Figure 3.1.5: Top - Image of the actual manufactured octagonal glass chamber after assembly onto the system (left). Six 1" diameter windows are available for optical access allowing four to be utilised for the MOT. Other orthogonal beams enter through the vertical windows. The science cell was fused to the octagon via a 38.1 mm glass transition providing sufficient clearance for required access while also minimising transfer distance. The rectangular cell allows a microscope objective to be placed close to the cloud.

minimised the overall size of the system while providing sufficient viewports for optical access. The octagon windows are AR coated ($700-1100$ nm) and 25.4 mm diameter, providing sufficient access for conventional 25.4 mm optics. Vertically, the 3D-MOT chamber is capped with AR 76.2 mm diameter windows. Originally these vertical windows were intended to be 5 mm thick, for close access, but manufactured to be 10 mm thick. This was done in order to prevent physical stress that would cause optical distortions, or even breakage, under vacuum. The science cell, also made from quartz, was fused to a side window, orthogonal to the CF flange. This is done to remove direct line of sight from the 2D-MOT beam and vapour source that feeds the main experimental chamber. The science cell is a $12.5 \times 46.25 \times 22.5$ mm Hellma Analytics 101.150-QS fluorescence cell with 1.25 mm thick walls. The clear aperture of the Hellma cell is the central $10 \times 45 \times 20$ mm region with $1-\lambda$ flatness specified across the apertures. This type of science cell is uncommonly thin in ultra cold atom experiments, yet enables a significant advantage. In particular it allows very tight physical access to the eventual location of BECs. The windows are thin enough, and the cell small enough, that commercial high magnification microscope objectives can be brought close for efficient imaging.

The other elements of the 3D-MOT side are shown in Fig (3.1.6). A six-way cube connects the HV and UHV side as well as the glass chamber by a set of bellows. These bellows were added

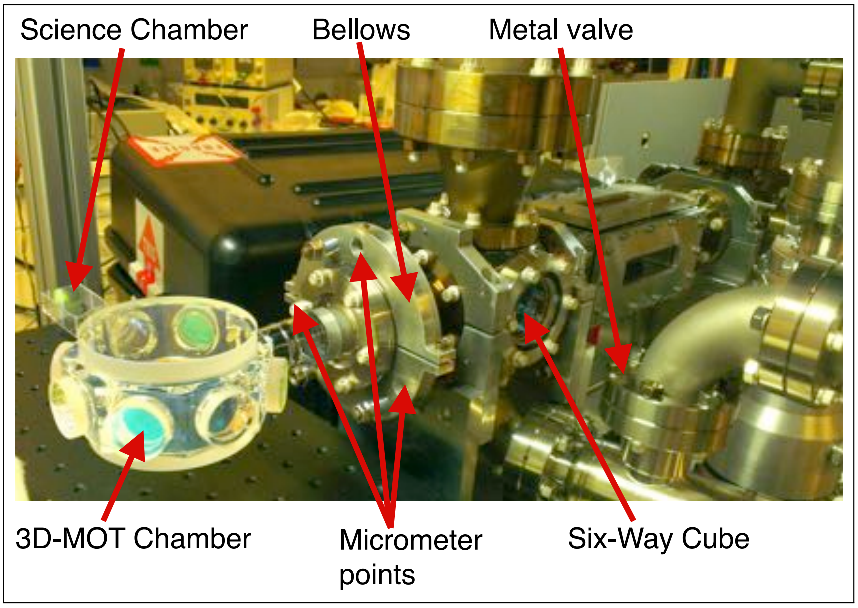

Figure 3.1.6: Image of the vacuum system illustrating the key elements of the 3D-MOT. Not shown is the NEXTorr pump and NEG element connected to the nipple vertically.

to reduce stress on the glass chamber, during construction, while also providing some spatial degrees of freedom to control the orientation of the glass cell. Due to imperfect manufacturing procedures the science chamber is not square relative to the octagon, off axis by $\approx 1°$. By adding micrometers at the bellows mounting point, the science cell may be brought square with optical table to prevent aberrations, and alignment complications, with the high-resolution imaging system. These micrometers (not pictured) are held in by a small M4 screw and rest on ball bearings on the attaching CF flange. The result is an ideal science cell positioning, but tilted octagon cell. This is acceptable as the 3D-MOT performance has shown to be have negligible susceptibility to this slight misalignment. The final element of the UHV region, is the conical 4.5" nipple connected to the NEXTorr ion pump (not shown). The 4.5 " adapter prevents limiting the pumping speed at the differential tube by having negligible resistance to conductance.

3.1.5 Assembly and Baking

In order to achieve UHV conditions ($< 10^{-10}$ mBar), required in the science chamber, as many impurity atoms and contaminants adsorbed to the interior surface and those trapped within the bulk of the metal components must be removed. This is crucial as small amounts of contaminants, such as skin oil residue or water vapour, would delay or limit the lowest obtainable pressure of a vacuum system. All elements prior to assembly were thoroughly cleaned. This included an ultra-sonic methanol bath of the 2D-MOT elements, alcohol wiping of viewports and flanges, and routine acetone rinsing. All vacuum connections are CF flanges sealed by single use copper gaskets and silver-plated vacuum bolts, with the exception of the 2D-MOT chamber. The sealing of the 2D-MOT chamber was a delicate procedure as any undue stress, on the windows or Viton O-rings, could easily result in damage or formation of gas channels.

HV and UHV pressures may only be achieved provided the outgassing of vacuum elements is small. Contaminants trapped within the vacuum components must thus be removed. To do so, the entire system goes through a baking stage where the temperature is elevated to $\simeq 275°$C as outgassing of impurity atoms, introduced during the manufacturing process, exponentially increases with temperature. Further, water and organic hydrocarbons adsorbed on the interior surface are also removed. For the bake to be successful the entirety of the apparatus must be brought up to temperature, lest outgassed atoms re-attach to the cold regions. These atoms would subsequently redistribute when the system was cooled to room temperature. This bake-out must be done under vacuum to remove all impurities. As ion pumps are only suitable for use at pressures less then 10^{-6}mBar, the impurities must be removed via alternate pumping methods. As such a bake-out and UHV realisation is a two-stage pumping process. First, the vacuum is pumped to a moderately low pressure and baked. Contaminants are removed by an a pair of external pumps, before the ion pump can be engaged. The standard configuration consists of a turbo pump supported by an atmospheric pressure pump, such as a scroll or diaphragm pump, known as the backing pump. These must be removed from the system as their mechanical motion can introduce detrimental vibrations to an experiment. By connecting them to the system through the metal valves, once impurities are removed, the system can be sealed off from the turbo and backing pump before they are switched off.

The general bake-out procedure was as follows. First, the ion pumps were off with the turbo pump idle while the backing pump reduced the system to its terminal pressure. A scroll pump was used for both sides of the system, with the pressure plateauing at 10^{-3} mBar overnight. The turbo pump was then activated reducing the pressure to $\simeq 10^{-7}$ mBar. Although this is a sufficient pressure in which the ion pumps could have been engaged, the outgassing of deep-seated impurities, constituting a form of leakage, would limit the pressure of the system and/or rapidly degrade the ion pumps. As such, the system was baked by increasing the temperature to promote this outgassing. For optimal effect, each component of the vacuum was heated to its highest rated operational temperature with thermal gradients across the system minimised. Naturally, glass

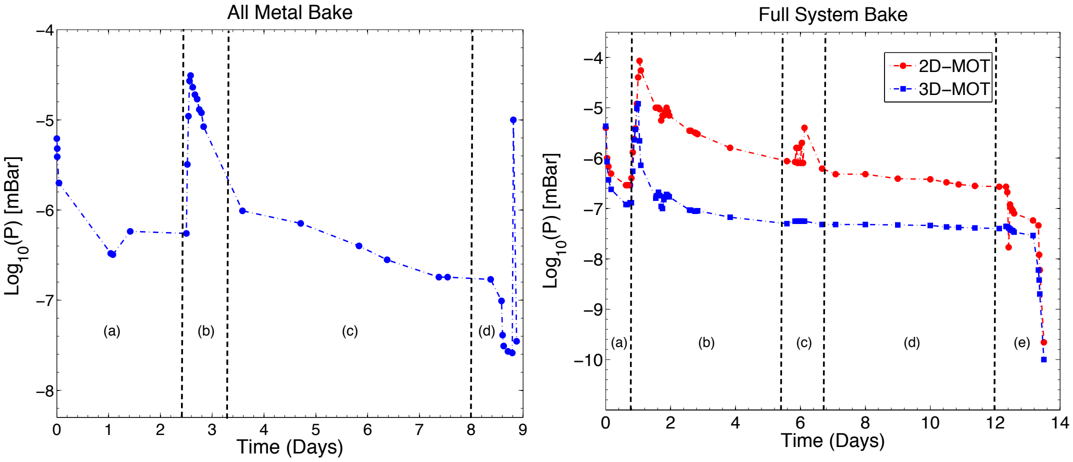

Figure 3.1.7: Representative pressure data recorded for the two key bakes of the system. Right - The all metal bake with four distinct regions (a) Turbo and backing pump pressure reduction before raising the temperature in (b) to $\bar{T} = 330$ °C. The extended bake (c) where the temperature remains constant until pressure begins to plateau. Once this occurs the system is brought back to room temperature and further pressure reduction occurs (d). Left - The second bake of the full vacuum system showing the pressure in the 2D and 3D MOT sides respectively. (a) The initial pump down of the system with turbo and backing pump before the temperature rise and first part of extended bake(b). The dispensers were outgassed in (c) before allowing another extended bake (d). The turbo pumps were switched off and ion pumps on in (e) resulting in pressures $< 10^{-10}$mBar on the 3D-MOT side as desired. A pressure spike in the all metal bake, section (d), was caused by brief activation of the vapour gas dispensers.

and other non-metal components could not reach the same temperature as stainless steel and copper and, as is not uncommon, two bakes were performed. Initially a higher-temperature all-metal bake was performed to quickly remove deep-seated impurities within metal components. The system was initially constructed using blank flanges and nipples in place of viewports, 2D-MOT and 3D-MOT chambers respectively. A nitrogen valve was affixed to the system for the baking procedure. Subsequently a lower-temperature bake was undertaken with all elements installed.

In order to rise the system to temperatures greater than 300 °C, resistive heating tapes, connected to mains-voltage and regulated by commercial light dimmer switches were wrapped around the entirety of the system. Thermocouples were then placed as close as possible to chamber walls in strategically-chosen locations, to probe the local temperature. Subsequently, to maintain heat, several layers of commercial aluminium foil were wrapped about the apparatus, creating an oven. The all-metal system was brought to an average temperature of 330 °C and held for 6 days before it began to plateau at approximately 3×10^{-8} mBar in two weeks.

Reducing the temperature back to ambient resulted in a further pressure drop, Fig (3.1.7) (left). Following this the system had to be fully assembled, with glass components added, necessitating opening the system up to atmosphere pressure, potentially reintroducing contaminants. To reduce reabsorption of these impurities the system was flooded with nitrogen and a continuous stream present during re-assembly. With the 2D-MOT and 3D-MOT chambers and viewports affixed, the bake-out procedure was repeated at an average temperature of 150 °C over a period of two weeks, Fig (3.1.7) (right). Here ion pump gauges monitored the pressure for each side. This proved important as the 2D-MOT cell took a significantly longer time to reach terminal pressure, attributed to the residual impurities in the 2D-MOT chamber and Viton O-rings. A custom brass oven was constructed to be placed around the 3D-MOT in order to avoid contact of the heating cables with the glass cell. During the bake the dispensers were also flushed of impurities by briefly passing current through them. Once brought to room temperature the all-metal valves were finger tightened while the NEG element and ion pumps were engaged. The two pressures quickly reduced to 3×10^{-10} and $< 10^{-10}$ mBar (the ion pump gauge measurable limit) for the 2D-MOT and 3D-MOT regions respectively.

While we have described the main two bake-outs of our system several complications arose that made the procedure more difficult. As our original, all-glass, 2D-MOT chamber cracked during its first assembly trial (after the all metal bake) and the new stainless steel 2D-MOT chamber had to be baked on it's own prior to assembly. Viton readily absorbs water and had to baked also. This was a precarious procedure as rising the temperature also results in the O-rings becoming more brittle, potentially hindering their ability to seal the system. As previously discussed the outer volume within the 2D-MOT could not maintain its pressure of 10^{-2} mBar for extended periods due to permeation through the outer o-ring. During the December festivities of the 2013-2014 summer this chamber was not outgassed for several weeks, enabling diffusion of atmosphere gases into the outer volume that also increased the pressure of the 2D-MOT chamber. As such another bake-out of the system, just on the 2D-MOT chamber, was undertaken to reduce the pressure back down. A final note is that, during assembly, two small leaks arose at the differential-pumping tube flange and bottom of the cube. While not initially a problem its has become apparent that the vacuum is no longer ideal, pressures on either side increasing to 3×10^{-10} and 5×10^{-8}mBar in the 3D/2D chamber, and may be contaminated due to their presence. In particular it is thought that they are somewhat pressure limiting the system and saturating the NEG element. Thereby reducing the pumping speed and hence pressure differential across the system. The result is the vacuum may soon be re-opened to atmosphere to mend these leaks and a second ion pump added to the 3D-MOT side of the system.

3.2 Experimental control

One of the technical challenges, for experiments in atom-optics, is the accurate timing and control on long and short time scales. At the beginning of each experimental run it normally takes ≈ 10 s→ 15 s to form an adequately sized MOT, and double this to form a BEC. Before, during and after these events a variety of smaller tasks must be completed with fine control down to μs. In the most general sense, a typical atom optics experiment requires control over a variety of electrical systems that require either digital or analogue input. Further, the time scales and resolution required for each of these is typically varied ranging from μs to s. This separates the requirements of a control system into two key elements, the components that create and produce signals, and the timing and control elements.

Commercial PXI input/output cards supply digital and analogue signals. These cards are housed in a National Instruments NI PXIe-1062Q chassis, enabling communication with the main experimental PC. An NI PXI-6723 card produces analogue signals. This module provides 32 analogue channels with digital triggering capabilities, and 8 digital I/O channels. It is slew rate limited to 10 kHz with outputs voltages from −10 to 10 V. Digital, TTL logic, is from a NI PXI-6514 with 32 available I/Os. They have two high levels, 3 V and 5 V. As these are integral and expensive components, they are protected against the circuits they connect to by buffer operational amplifiers circuits. Connection cables connect the I/O cards to connector busses in rack mounts that house the buffers, Fig. (3.2.1).

In order to interface with the cards we make use of the open source 'Cicero Word Generator' control package, authored by Aviv Keshet at the MIT Center for Ultracold Atoms. This software allows users to visually configure complex timing sequences. Most significantly, the software includes the option for a 'variable timebase'. This has the ability to generate clock pulses, triggering outputs from NI cards, only when card output needed to change. This is opposed to a 'fixed timebase', where each clock pulse would update the cards regardless of its requirement to change. As such buffer length, which are a list of instruction for the card, is minimised. Additionally, the ability to use an field programmable gate array (FPGA) enables a user to divide down an external frequency source for use as a variable timebase. In this experiment we use a SRS FS725 10 MHz atomic clock as a stable clock base, which the FPGA can divide down. A schematic of the computer control and timing system is shown in (3.2.1).

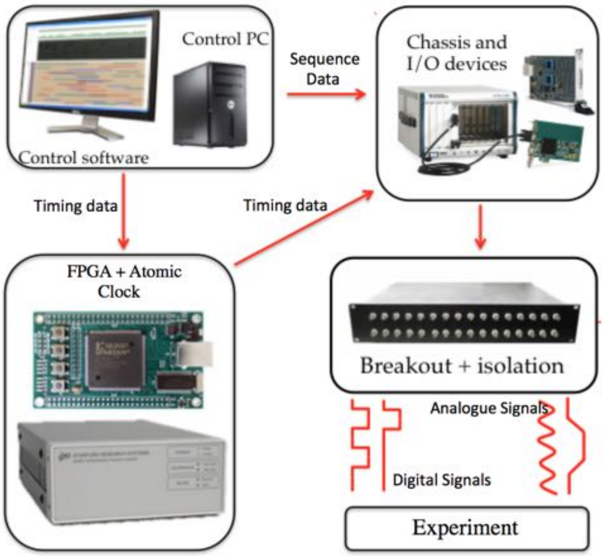

Figure 3.2.1: Schematic of the sequence and timing signals in the experiment. The control software is Cicero Word Generator with the Atticus server for communication with the NI hardware and FPGA. The FPGA creates a variable timebase, for optimising sequence length, based of a stable 10 MHz fixed signal from the atomic clock. The FPGA triggers the NI hardware to change its output which is passed to the experimental apparatus through protective breakout boxes.

3.3 Laser System

Light required for the efficient cooling, trapping and imaging, of atomic clouds must be of a specific wavelength and narrow linewidth, when compared to the Doppler width and the hyperfine states of atomic gases. This is readily achievable with commercially available lasers, generally stable below the relevant atomic linewidth, 6.0 MHz and 6.2 MHz for ^{87}Rb and ^{41}K, respectively. This experiment consists of a combination of commercial external-cavity-stabilised diode lasers (ECDL) and tapered amplifier (TA) modules with linewidths typically below 1 MHz. These diode lasers also demonstrate a mode-hop free tuning range > 15 GHz, and powers ranging from 100 mW to 1 W. Here we discuss, in detail, the laser system required to produce the broad range of frequencies to cool, trap, and image atoms, along the experimental pathway, to condensation. In particular, we discuss the frequency locking, beam control and combination techniques that make our laser system, Fig (3.3.1).

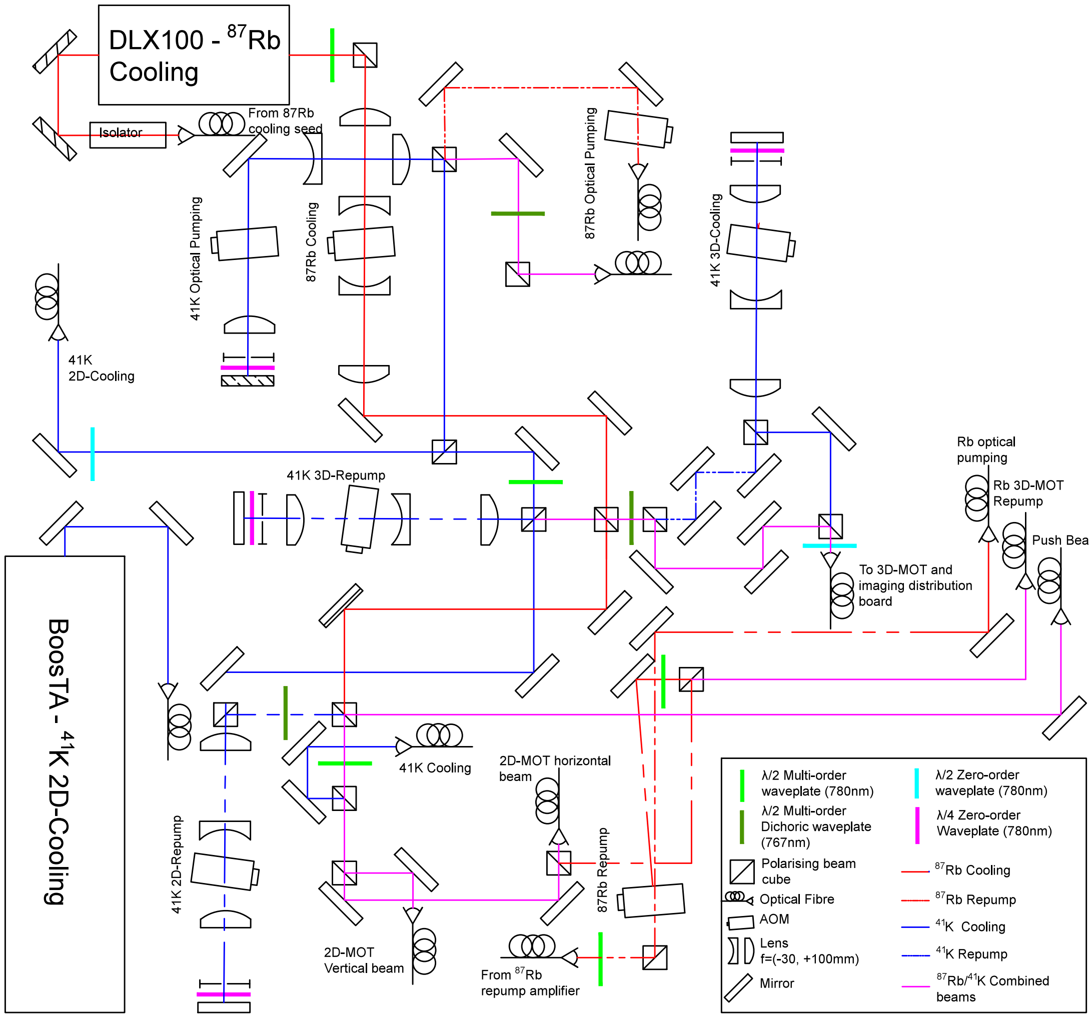

Figure 3.3.1: Overview of the laser system used to generate the cooling, repump and imaging beams used in the experiment. See text for a detailed description. Not shown are the master lasers that provide the frequency stabilised 'seeding' light for the amplifiers.

3.3.1 Saturated absorption and locking

When an ECDL laser is not actively stabilised, the frequency will drift in accordance to fluctuations in temperature with time. This is prohibitive for the requirements of laser cooling. The precise knowledge and control of the laser frequency is also required. Naturally, locking the laser frequencies directly to the hyperfine features of the relevant atomic spectra is ideal as these provide a natural wavelength reference. In order to do so these states must be distinguishable within the Doppler broadened profile. The method to do this, employed in our laboratory, is saturated absorption spectroscopy [154].

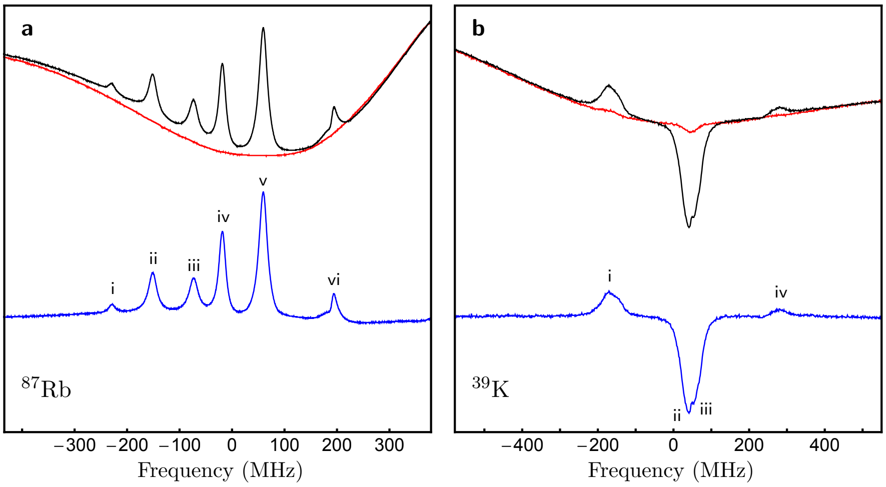

Figure 3.3.2: Saturated absorption spectra of the D_2 cooling transitions of ^{87}Rb and ^{41}K, courtesy of [156]. The Doppler profile shown in red, saturated spectroscopy in black and the difference in blue. (a) Transitions from the $|F = 2\rangle$ sate of ^{87}Rb showing the direct transitions to the $|F' = 1, 2, 3\rangle$ i, ii, iv, the rest being cross over transitions. (b) Similarly the spectra of ^{39}K showing the merged $|F = 2\rangle$ (i) and $|F = 1\rangle$ (iv) transitions. ii and iii correspond to their respective cross-over dips respectively.

In saturated absorption spectroscopy, a weak beam is passed through an atomic vapour cell, producing a thermally broadened absorption spectra (Doppler spectrum), as the laser is scanned over a range of frequencies. A counter-propagating pump beam also moves through the cell. In general, atoms will interact primarily with a single beam as a result of Doppler shifts. However, those at rest will interact with both beams simultaneously. For these atoms, the pump beam forces them to lie in an excited manifold or cycle them into a dark state. As a result, the probe beam will no longer be attenuated due to the fact that a significant number of atoms will be in a ‘dark’ state. Similarly if the wavelength, in the atomic reference frame, lies halfway between two transitions (such between the cooling and repump lines) an additional feature in the absorption profile is observable, termed the cross-over peak. Typically this is the strongest feature in the saturated absorption spectroscopy spectra and used to establish a stable frequency reference. Due to the small natural abundance of ^{41}K (6.7 %), its signal is weak. As such the lasers are locked to the cross over transition of the more abundant (93 %) bosonic isotope ^{39}K. Further, potassium has an inherently small splitting between hyperfine features that are not resolvable in our lab. These saturated absorption spectra for the D_2 cooling transition for both species are shown in Fig (3.3.2). Our cooling lasers, for ^{87}Rb and ^{41}K, are locked to the $|F = 1, 2\rangle$ cross over dip (ii). Similarly the repump laser is locked to the $|F = 1\rangle$ cross over feature.

3.3.2 Beam Control

A broad range of control over a beams frequency, power and the ability to toggle an on/off state is integral for the operation of the experiment. Control over the frequency and power is given by acousto-optic modulators (AOMs) and their driving circuits. AOMs consist of a crystal transducer capable of converting RF energy to sound waves. These travelling sound waves produce a diffraction grating on which incident light may scatter. The coupling of incident light with the sound waves, under the correct conditions, can result in the majority of power being placed into a non-zero order of the diffraction pattern. By varying the frequency of the input signal the periodicity of the diffraction changes along with the frequency of the scattered light.

The driving signal is provided by a voltage-controlled oscillator (VCO) that passes through a voltage variable attenuator (VVA), a RF switch and then a 2 W amplifier before creating the diffraction grating in the crystal. All these elements are Mini-Circuits elements connected via SMA connectors. The VCO has a user input that defines the frequency fed into the VVA. Similarly the VVA has a user analogue voltage input which enables the resistance of this element to be changed as required. This alters the power into the AOM, and subsequently, the diffraction efficiency giving a user power control over a beam. Lastly, the RF switch ensures that the signal to the AOMs can be extinguished. For ^{41}K, the majority of AOMs are 2 W AA-opto electronics MT110-A1-2, centred on 100 MHz. The remainder, used mostly for ^{87}Rb light are 1 W 80 MHz Isomet 1205c units.

While the RF switch does provide a method for toggling on and off the AOM it does not provide complete extinction as thermal and trickle effects persist. A simple solution to completely extinguish a beam is a physical barrier in its path, via a shutter. Commercially multiple options for optical shutters exist however in-house shutters provided the best performance. These are made based on the design from the Scholten group in Melbourne [157]. The shutters are constructed from generic defunct iPod hard drives. The voice coil actuator drives the hard drive arm that moves a flag shuttering the beam as required. These shutters are fast, with a rise time of $\simeq 3$ ms, and provide complete extinction.

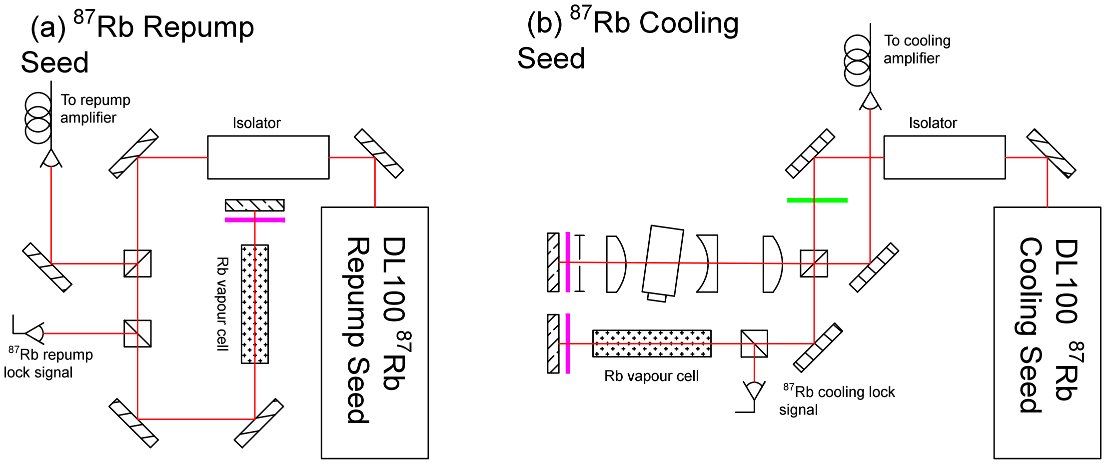

Figure 3.3.3: Schematics of the ^{87}Rb master oscillators for the repump (a) and cooling (b) light.

3.3.3 Rubidium laser sources

The repump and cooling light, for trapping and cooling ^{87}Rb, is derived in a two-stage process. First, low-powered master oscillator ECDLs are locked to their respective cross-over transition, Fig 3.3.3, with their output used to seed a pair of amplifiers, made from modified laser cavities. Both master oscillators are Toptica DL100 units, with outputs of 80 mW. A small portion, ≈ 4 mW, of this is sent to the saturated absorption lock pathway. In general the pathway consists of a Rb vapour cell with the retro-reflected 'probe' beam fed onto a photodiode. This signal is fed into a lock-in amplifier, producing an error signal along peaks of the absorption spectra. The error signal may then be used to lock the laser to the correct transition. Cooling light is locked to the $|F = 2\rangle \rightarrow |F' = 2, 3\rangle$ crossover peak, located 133 MHz below the $|F = 2\rangle \rightarrow |F' = 3\rangle$ cooling transition. A double-pass acoustic-optic modulator (AOM), centred on 100 MHz changed as required, in the cat's-eye retroreflector configuration, in series with another single-pass AOM (fixed at -80 MHz after the amplifier) brings the wavelength closer (or further) from resonance as required, Fig (3.3.3). Quantitatively, the double pass AOM may be used to scan the detuning, $\Delta = +1\ \Gamma \rightarrow -18\ \Gamma$ as required, over a short time period. Care must be taken that detuning does not cause power fluctuations from decreased diffraction efficiency through the AOM. For cooling and trapping we red detune to $-2.7\ \Gamma$. During imaging the light is brought closer to resonance, for a stronger absorption signal. Given the limited amount of real estate, on the main experimental table, and concerns about mechanical vibrations from the main experiment, these master oscillator ECDLs are placed on a separate optical bench to the vacuum system and other optical elements. This isolates them from the various mechanical components that might disrupt the lock, such as shutters. A 10 m, 630 nm Thorlabs polarisation maintaining (PM) fibre transports the seed light for the cooling amplifier to the main experimental table. This serves as the cooling light for both the 2D and 3D MOT beams as required.

Given the large separation between the $|F = 1\rangle$ and $|F = 2\rangle$ states of ^{87}Rb ($\approx$ 6.8 GHz) it is not practical to derive the repump light from the cooling light directly. Previously, we attempted to use an offset lock, using the set frequency of the cooling light to lock the repump light, but found the method not suitably stable. As such another saturated absorption spectroscopy lock was used. Repump light is locked to the $|F = 1\rangle \rightarrow |F' = 1, 2\rangle$ cross over peak, 78.5 MHz below the desired repump transition ($|F = 1\rangle \rightarrow |F' = 2\rangle$). As per the cooling light, the majority of power is coupled into an optical fibre to use as a 'seed' in the modified Toptica DLX110. This unit, acting as an amplifier, has a small aperture drilled into the rear with its grating removed, such that the cavity is fed directly from the ECDL light. This provides a high amount of power, directly available for the main experimental region, without having to worry about locking it directly. This amplifier feeds several cold atom experiments in the laboratory, with approximately 80 mW brought over to our experimental table. The repump light is brought to resonance by a single-pass AOM providing a +78 MHz shift. This light serves as the repump for both the 2D & 3D-MOT.

3.3.4 Potassium laser sources

In comparison to ^{87}Rb, the laser requirements for effective cooling and trapping of ^{41}K are more technically demanding. This is a consequence of the energy spectrum separation between $|F = 1\rangle$ and $|F = 2\rangle$ manifolds. In general, a greater amount of power is required, as the distinction between cooling and repump light becomes semantic, while four different wavelengths are required to efficiently operate the 2D and 3D-MOT [69]. In regards to specifically targeting ^{41}K atoms, it is important to recognise that due to the low natural abundance of this isotope ($\approx$ 7%), creating a reliable lock on the repump, cooling or cross-over dip is difficult with regular vapour cells. As a result, to produce light resonant on the ^{41}K D2 line, the master laser is locked to the ^{39}K cross-over transition and post-processed via AOMs to the desired frequency.

The 'master' laser for the ^{41}K light is provided from a refurbished Toptica DLX110 ECDL, optimised for lasing at 766 nm, with a nominal output power up to 400 mW. Frequency stabilisation is done via a saturated absorption spectroscopy set-up, where 2 mW is provided from an internal beam sampling plate, emitted from a side aperture. We shift the output of this beam by 85 MHz before passing it through the vapour cell. The signal from the retro-reflected beam is sent to a Toptica Digilock module, which allows computer control of the lock. While we lock to the $|F = 1, 2\rangle \rightarrow |F'\rangle$ ^{39}K crossover feature, the frequency shift provided by the AOM ensures the light is ≈ 22 MHz red detuned of the $|F = 2\rangle \rightarrow |F' = 3\rangle$ cooling transition of ^{41}K, Fig (3.3.4) (left). We may change this detuning by changing the frequency of the AOM, when required. The bulk of the power from this laser is coupled to the main experimental table to be 2D-MOT cooling light. The remaining (≈ 60 mW) is used to seed a Toptica BoosTA tapered amplifier. This provides the power for the remainder beams required for cooling, trapping, optical pumping, push and imaging the cloud. This BoosTA preserves the spectral properties of the input light, while supplying 1.5 W. While sufficient, the outlay of the locking AOM means any change (such as optimisation of 2D-MOT detuning) will result in a cascade of frequency changes throughout the system. Fortunately, the cat's eye retroreflector arrangement of AOMs prevents small changes in detuning from producing large changes in power delivery.

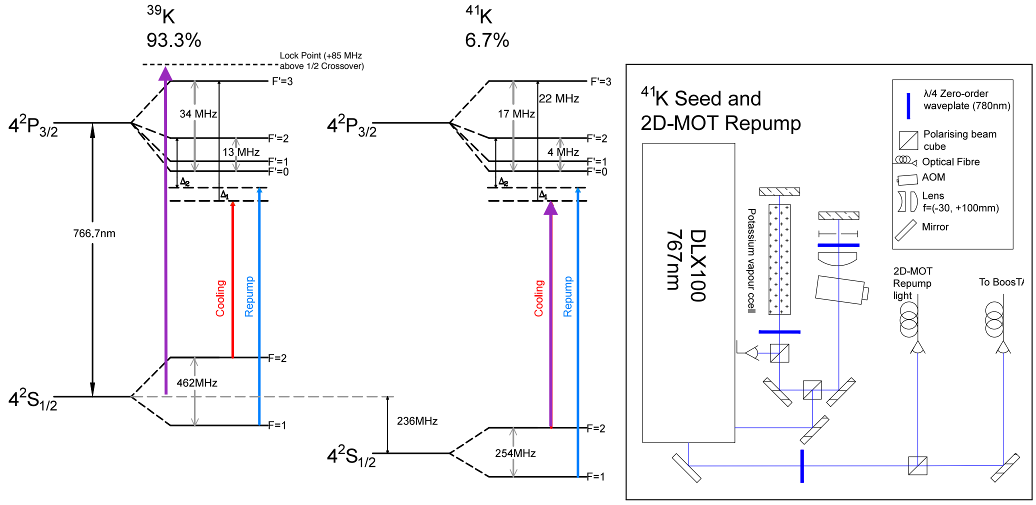

Figure 3.3.4: Left - Level diagram showing the locking frequency and corresponding frequency in reference to ^{41}K. In particular we lock blue of the cross-over feature of the abundant isotope, which results in a red-detuned cooling beam on the target species. Right - Schematic of the DLX110 that is locked to this transition. It feeds the tapered amplifier while also providing sufficient 2D-MOT cooling light.

The remainder of light necessary for cooling and trapping potassium are derived as follows. Amplified cooling light from the BoosTA is first coupled into a Thorlabs single-mode PM630 fibre with a 18 mm Shcäfter Kirchhoff optical coupler with approximately 70% coupling efficiency. This is necessary as the spatial mode output of the BoosTA is poor and must be cleaned for efficient use in the remainder of the system. As a result, only 1 W remains for coupling to the main experimental chambers. The remainder of beam manipulation is done by multiple passages through 110 MHz AOMs. After these multiple passages, Fig (3.3.1), we are left with four distinct beams with differing frequencies. These are the 3D-MOT cooling and 3D-MOT repump beams, as well as the 2D-MOT cooling and 2D-MOT repump. Some of these are cascaded, such as how the 3D-MOT cooling is derived from the 3D-MOT repump which is derived from 2D-MOT cooling, which must be considered when optimising the performance of the system.

3.3.5 Beam Combination and Fibre Launching

Following beam manipulation, there are six trapping and cooling beams that must be coupled into five different optical fibres for use at the vacuum apparatus. The 3D-MOT beam contains ^{87}Rb cooling and ^{41}K 3D cooling and repump light. ^{87}Rb repump is brought in on a separate fibre, as only a small amount of power is required for a efficient cooling and trapping. Originally all four wavelengths were to be brought into the 3D-MOT distribution board, on a single fibre, however the dichroic waveplates on-hand and required to do so, were not zero-order for 766.7 nm and any combination of all four wavelength wavelengths would result in a loss of $\approx 20\%$ power from one of the ^{41}K beams. The combination of these frequencies involves the mixing and overlapping of the beams via the use of wave plates and beam cubes, observed by tracing the beam pathways in Fig (3.3.1). The 3D-MOT fibre then couples to the distribution board that controls splitting and power balance between the three pairs of orthogonal beams required for 3D-MOTs, Fig (3.3.5). A small glass slide picks off a portion of this power, before entering the distribution region, for use as imaging light.

In contrast to the 3D-MOT beam, the 2D-MOT beam does not couple all required frequencies into a single fibre before delivery to the vacuum chamber. Instead, two are derived from the free-space coupling without an intermediate fibre. Similar to the 3D-MOT, the three wavelengths of ^{87}Rb cooling and ^{41}K 2D cooling and repump are combined to a single beam via various wave plates and beam cubes before being split into the vertical and horizontal 2D MOT fibres. After this split, the two beams have well defined polarisation and adding the ^{87}Rb repump will not cause power losses. This is done only on the horizontal beam, Fig (3.3.1).

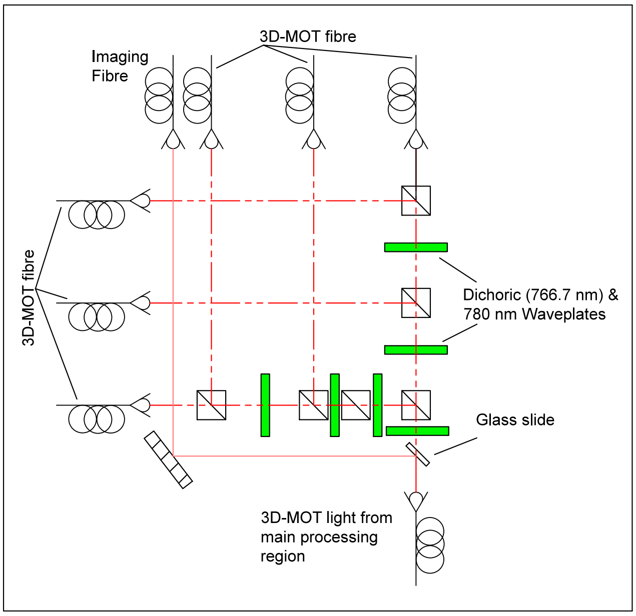

Figure 3.3.5: Distribution board for separating the single 3D-MOT fibre containing three frequencies into the six beams required to cool and trap atoms in three orthogonal directions. The wave plates and beam cubes allow for precise power balance and control. Each fibre couples with approximately 85 → 90% efficiency. An extra waveplate is provided in the first reflected pathway to dump specularly-reflected s-polarised light.

3.4 Magnetic Coils

The remaining major experimental infrastructure to be discussed are the magnetic coils used to produce quadrupole fields for the 2D and 3D-MOTs, magnetic transfer sequence, and bias field production at the science cell. The novel coil and heat dissipation design of the 3D-MOT side coils resulted in a technical publication [158]. While this paper describes the primary iteration of the design a manufacturing fault of the glass chamber meant a second iteration was required for appropriate dimensionality.

The production of controllable magnetic fields for cold atom experiments has been the subject of extended study [159], and benefits from the advancement of conventional electromagnets in other fields. Generally, magnetic coil designs tend towards maximising current density through the coils which is limited by heat dissipation capabilities [160, 161]. One common solution, to maximise heat dissipation, is the use of hollow-core conductors, allowing for water cooling through the wire core. However when using low current power supplies to drive coils, achieving high fields necessitates large numbers of turns, N, and thus high pressure coolant systems as the viscous resistance scales with N^3 [162, 163]. This use of hollow or solid core wire is common in the cold-atom community as it is easy to construct and demonstrate moderate cooling capabilities sufficient for most systems. Due to the individuality and broad scope of modern cold-atom experiments and differences in 'build', it is necessary to constantly improve design.

Recent innovations by Sabulsky et al. have demonstrated a modified Bitter-type electromagnet consisting of axially-stacked copper arcs with highly efficient heat dissipation [164], demonstrating a temperature change of 8 °C/kW. The design is easily extended to include greater numbers of arcs, without restriction of coolant flow, and achieves a turn density of > 0.77 turns mm^{-1}, but may limit optical access and requires technical machining. A radially constructed electromagnet, by Ricci et al. has also utilized ducts for an improved cooling arrangement, but with relatively low copper fill and turn packing ratio [163]. These designs are not readily extended to include adjacent and overlapped magnets which is required magnetic transfer schemes [165, 166, 167].

In our experiment a 6 kW power supply, with maximum current output of 100 A, is available. An optimal coil design required a high number of turns, to produce the required field gradients (160 G/cm for efficient microwave evaporation), while also considering the physical dimensions of the coils due to spatial constraints around the cell and optical access. Given the small distance the atomic cloud must be transferred to reach the science cell, we elected to have a three-coil transfer system, section 4.2.2. Given these constraints the free variable to optimise for our coils was turn density. This rejected the usage of conventional hollow core wire and cooling methods. Here we present our novel, high-turn density, electromagnet coil design arrangement that combines the structural simplicity of conventionally wound coil while maintaining large cooling surfaces.

3.4.1 Magnetic coil design

In order to achieve high turn densities we elected to construct the coils by concentrically wound EMI insulation foil. The wire itself consists of 25.4 μm insulating Kapton bonded onto 127.0 μm thick copper of varying height (Alpha-Core Laminax-B), Fig (3.4.2). Prior to assembly the Kapton was trimmed to be flush with the copper and adheres to only a single side of the foil. As such when wound upon itself each turn is electrically insulated. This material enables a fill factor, ratio of conductor to cross-sectional area, of up to $\lambda = 0.83$. However, this disables the possibility of passing coolant in parallel with current, similar to conventional coils, but provides cooling surfaces along the axial faces of the electromagnets. Three sets of coils, for use in (anti-)Helmholtz configurations were constructed via the radial winding of the copper tape over a PVC form, matched to the required dimensions, Fig (3.4.1).

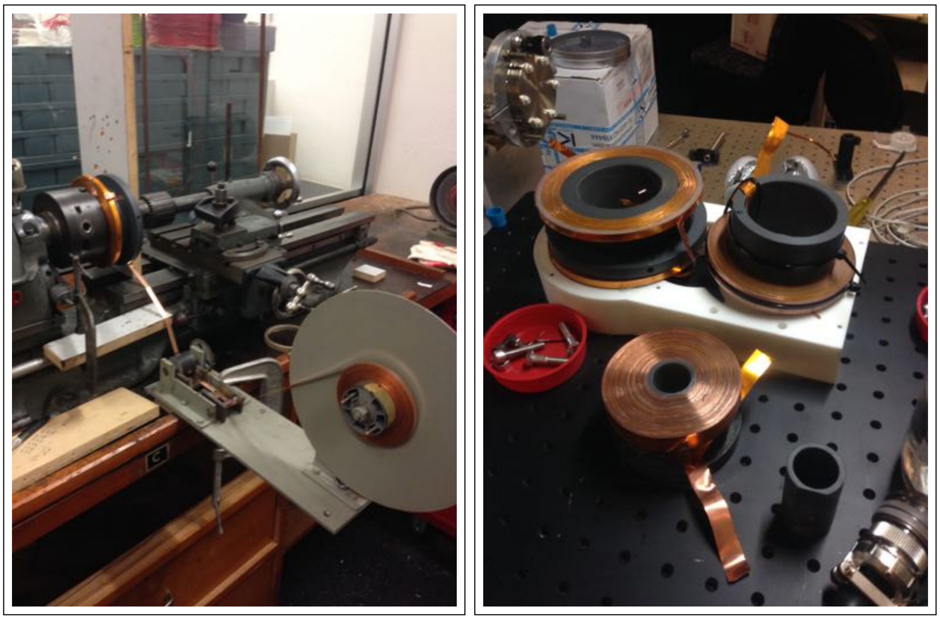

Figure 3.4.1: Left - The set-up for winding coils. A loose spool feeds over several pulleys before being wound about a PVC form. The brake that maintains tension and guides the foil onto the PVC piece is not pictured. Right - Fully wound coil set prior to thermal epoxy bonding.

The construction procedure underwent several iterations in order to produce usable electromagnets. In order to bond the coils, such that they would not unravel, a thin layer (0.3 mm) of thermal epoxy (Cotronics 128, thermal conductivity 4.3 W/Km) was applied to the axial faces. A earlier method used regular glue to bond each layer to its neighbour, however this rapidly reduced the fill factor, λ. Further, with moderate powers passed through the coil the epoxy would deteriorate. thermal epoxy was ideal, despite reducing thermal conductivity between the copper and coolant, as it provided a protective layer to resist corrosive effects. Despite being a thin layer, water ingress has not been seen to occur and deemed sufficiently insulating. The epoxy is also electrically insulating but this feature is unimportant as even uncoated copper coils present no shorts between layers. In order to achieve maximum fill factors, constant high tension during the winding was crucial. Furthermore, surface uniformity is highly desirable for small coils to remove any inhomogeneities of the produced field and to stack coils closely. To maintain the flatness, a guiding channel with adjustable tensioning ‘brake’ was made from PVC and placed between the spool and coil winding guide. In total our coil system consists of two identical pairs of three different coils (I, II & III). The properties of each coil, including number of turns N_i, inner and outer radii r_i & r_0, fill factor λ and turn densities are summarised in Table 3.1. Coil I

Coil	N (turns)	r_i (mm)	r_o (mm)	λ(%)	Turn density (mm^{-1})
I	39	40	47	69	5.6
II	112	15	35	72	5.6
III	58	45	55	74	5.8

Table 3.1: Physical parameters of our quadrupole producing coils used on the main apparatus. A second set of coils exists to be placed in (almost) anti-Helmholtz configuration.

and II only sustain relatively moderate, time averaged, powers in the experimental sequence and thus constructed from a single continuous piece of 12.40 mm high foil. Coil III, however, must sustain higher powers for greater times and is constructed from two 6.35 mm coils connected in parallel, their cross sections and relative locations are shown in Fig (3.4.2). This two coil approach enables greater surface area for cooling.

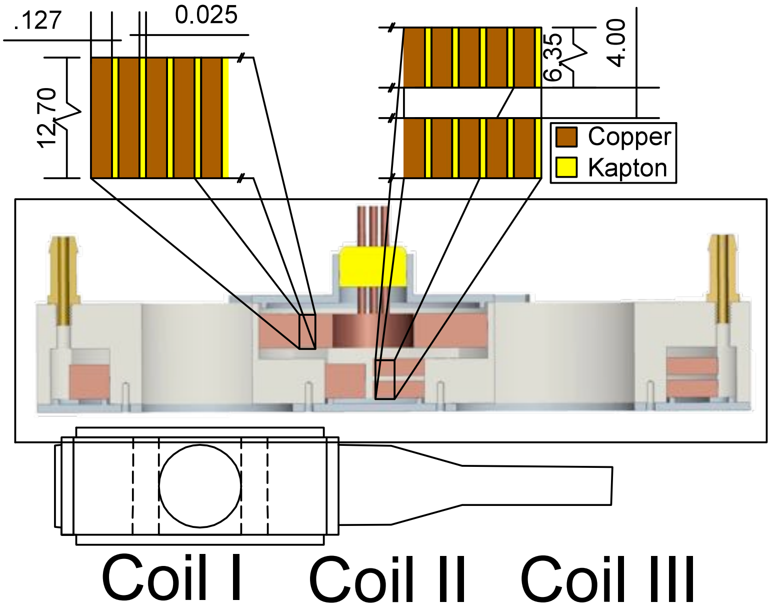

Figure 3.4.2: Cross section of our coils showing the relative positioning and Kapton sizes (mm). In particular Coil III is constructed of two smaller electromagnets connected in parallel for greater cooling capacity. These are encased by machined Macor® providing channels along the axial faces of coils for heat dissipation.

3.4.2 Cooling design

Machined Macor®, a glass-ceramic, provides channels through which heat is removed from the coils, Fig.(3.4.2). This material is non-magnetic and non-conductive, eliminating eddy currents and advantageous when rapidly changing the magnetic field. It further demonstrates a low thermal expansion (coefficient of expansion of 9.3×10^{-6} /°C) and temperature stability up to 1000 °C. For use as a magnetic transfer circuit the coils must be overlapped at alternating heights. Viton spacers are placed on the axial faces of the coils to create $3 \to 5$ mm channels for coolant to flow over these surfaces. Optical access to the glass cell is provided through the central regions of Coils I & III, via bored holes, Fig.(3.4.3). Electrical connections are fed out through the centre coil.

The coils are placed within the Macor hold and sealed via a PVC lid with a small, 2 mm lip within the coil voids made water tight by a bead of silicon sealant forming a gasket. These lids are held via 5 mm M3 nylon screws. Coolant (water) is brought, and removed, into the Macor cavity by 8 mm flexible tubing through a thread-to-push-in adapter. Flow is provided with a commercial aquarium pump (Eheim 1046) with a pressure of 0.12 bar and maximum flow of 300 lph. The flow rate is mediated by a manual ball valve, with a maximum rate of $Q = 2.8(2)$ L/min through a single hold, limited by pump pressure and tubing size. Heat is removed from the active coolant through the combination of a 20 L reservoir and chiller unit (Hailea HL-380CA) set to 20 °C. K-type thermocouples were also attached to the electromagnets in order to monitor the surface temperature.

3.4.3 Control and Safety

In order for electromagnets to do useful work in the system the current passing through them must be well controlled, known and stable. Here this is achieved via a feedback stabilised MOSFET control circuit. Power for the coils is provided by a 60 V, 100 A supply (Delta Elektronica SM60-100) run in CV mode. In order to have control over the current through an individual coil a control circuit creates a variable resistance in series with a coil pair via the moderation of the gate voltage on a high-power MOSFET (IXYS-IXTX200N10L2), Fig. (3.4.4). For a given voltage range the response of the MOSFET will also be linear. During operation of the coils both the MOSFET and the individual electromagnets dissipate the power passed through them resulting in an increase in their temperature and subsequently changing their resistance. This would produce a gradually changing magnetic field if not well controlled, which is highly undesirable

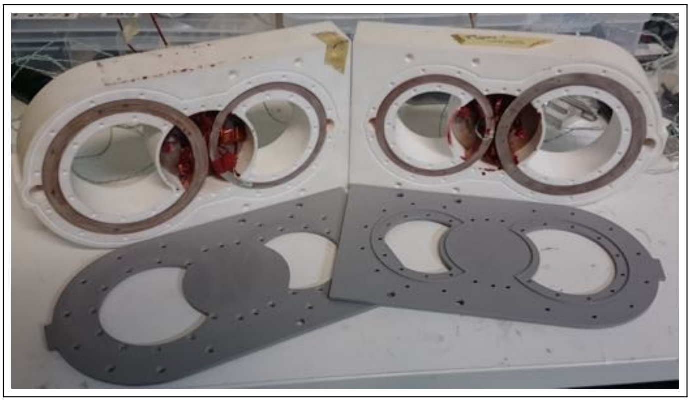

Figure 3.4.3: Photograph of the coil pairs wound and situated within the Macor hold. Noticeably there are differing radii and optical access through coil I and coil III representing the required access at each point. In particular the larger internal radius of coil III is necessary in order to get a microscope objective close to the glass cell for high resolution imaging. Through coil I only counter propagating 25.4 mm diameter MOT beams are required. Also shown are the sealing PVC 'lids' which have a lip to hold the coils firmly and provided a surface to seal against internally so no water can leak or air 'sucked' in.

for most applications in the experiment. In order to compensate for this, a negative feed back loop is provided via a hall probe (S25P100D15Y) for measuring the current and an op-amp, which serves to stabilise the current in response to current changes, Fig 3.4.4 (right). As the magnetic field is proportional to the current passed through the coils the field is stabilised.

In order to protect the analogue control box that supplies, the gate signal to set the current through the coils, and from any unintentional analogue input is passed through a unity gain op-amp buffer before passing through a low-power MOSFET. The analogue signal will only be passed to the feedback op-amp if a TTL input, on the gate of the low-power MOSFET, is positive. This TTL input is supplied via a optoisolator, which separates the digital control box from the coil circuit, Fig 3.4.5 (left). Three versions of this circuit are run in parallel from the main power supply to drive the three electromagnet pairs individually. During operation the MOSFETs must dissipate moderate powers, and if left thermally isolated, would break down. As such these elements were clamped to a water-cooled steel block via silicon heat-transfer pads to keep them within operational temperatures in the main circuit box Fig 3.4.5 (right). Since completing laboratory work this has been updated and each MOSFET has its own 3D-printed enclosure and aluminium water cooled module that electrically isolates them while providing superior heat dissipation.

Seen in the control circuit diagrams are flyback diodes, which are used to allow current to

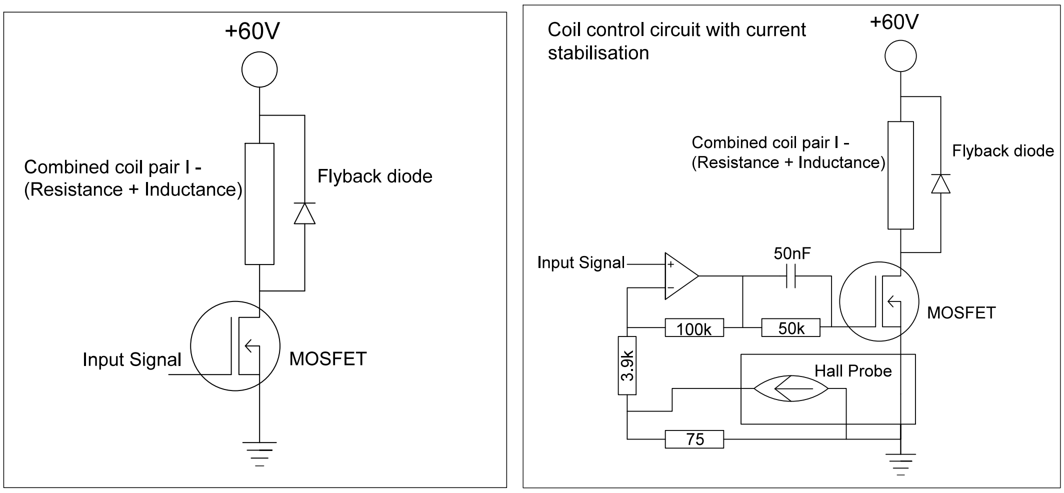

Figure 3.4.4: (Left) Schematic demonstrating basic function of the coil control circuit. A signal applied to the gate of the MOSFET will change the effective resistance from the 60 V supply to ground. As such a change is gate voltage will alter the current through the coil. (Right) Coil control circuit with feedback circuit implemented. As the coils and MOSFET change resistance the current through them will change. This change in current will produce a signal to feed to the negative terminal of op-amp forcing the output to change until the inputs of the op-amp are equal.

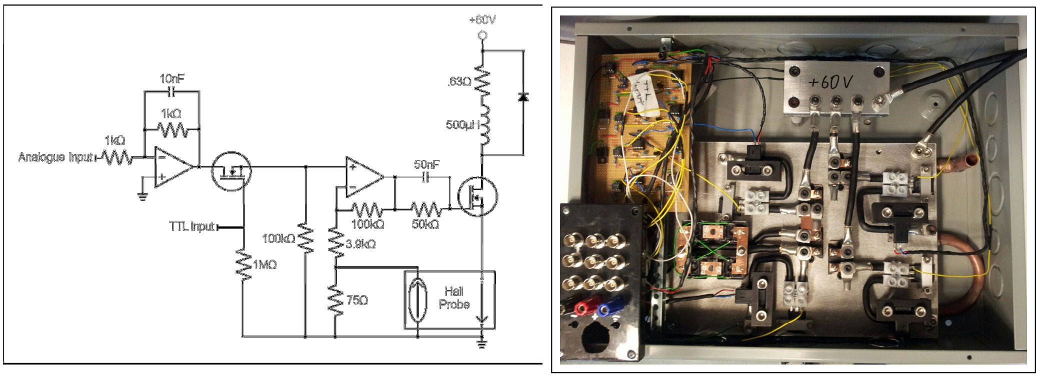

Figure 3.4.5: Schematic (left) of the three parallel circuits used to drive the coil pairs. The main elements are the driving power supply with current regulated by the high-power MOSFET. The circuit box (right) shows the parallel connections for the three coil circuits from the 60 V. The components all are secured to a large aluminium block. Viewable is a copper pipe, which follows a serpentine pattern underneath and provides water cooling to the aluminium block, as a result anything that is in thermal contact with the aluminium may dissipate heat readily.

flow back into the power supply when the coils are abruptly turned off for avoiding a high voltage spike on the MOSFET drain. For coil pairs I & II a regular diode was sufficient however the ‘switch off’ time at moderate currents is too long for coil pair III, used to provide confinement

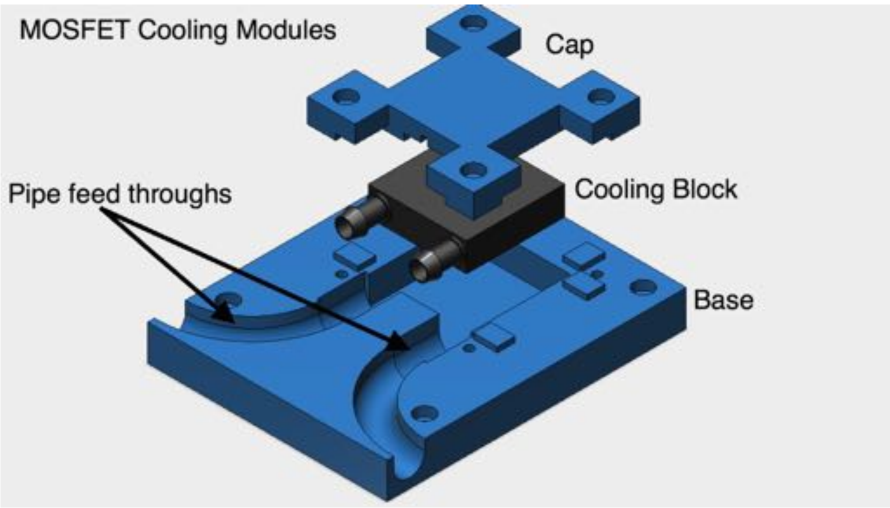

Figure 3.4.6: Individual MOSFET cooling module that provides superior heat dissipation capabilities then the original cooling method. A MOSFET is pressed between the cap and cooling block with silicon heat paste maximising thermal conduct between the block and the MOSFET. Water is brought in and out by flexible tubing that connects to the aluminium cooling block. As the base and cap are 3D printed components the MOSFETs are electrically isolated from one another. Previously a silicon pad had to be provide insulation as the cooling block housed all MOSFETs.

in the science cell. As such, a Zener diode clamp [168] is used instead to rapidly decrease the current decay through the coils when signalled off ($\approx 50\ \mu$s at 60 A)

While the coil driving circuit provides sufficient control over the current and turn on/off of current through the coils it does not protect it against some unforeseen or unintentional behaviour or component failure. In particular if the cooling water stops flowing, or a control circuit fails the coils may overheat and result in a catastrophic failure. As such, an interlock circuit is present that monitors the temperatures of each coil, temperatures of each MOSFET, the current through each coil and the flow rate. In particular K-type thermocouples are read into an Arduino Uno via MAX31855 thermocouple amplifiers. A brass hall-effect flow rate meter is also monitored by the Arduino and determines the flow rate by measuring the frequency of the rotor. Similarly, Hall probes monitor the current through each coil, which the Arduino converts to a current. Each interlock ‘cycle’ the Arduino measures these values and compares them to pre-set maxima/minima. If they fall outside these ranges the power supply interlock is toggled, and current can no longer be drawn. As an additional precaution, the Arduino itself is interlocked to prevent any failures associated with itself. In particular if it becomes inactive a 555 ‘watchdog’ circuit [169] will restart the Arduino making it trip the interlock and reinitiate the interlock checking procedure. If the Arduino interlock circuit does activate then the interlock will not be reversed until a N/O push button is manually pressed by a user. These additional precautions prevent any unspecified or sporadic operation of the coil cicuit.

Briefly, additional modifications to the Coil pair III control circuit exist. This is the ability to switch from quadrupole field producing anti-Helmholtz configuration, required for magnetic trapping and evaporation, to bias field Helmholtz configuration through a pair of relays. Further an additional control circuit, between the two coils, is present enabling the coils of the pair to run at different currents. This will, in the future, allows us to move the vertical position of the cloud for imaging with the highest resolution 0.65 NA microscope objective.

3.4.4 Coil Performance

The inductance, resistance, volume available, and operation temperatures are crucial constraints in coil design determining the maximum attainable field, or field gradient for anti-Helmholtz coils [163]. Here we discuss these parameters and cooling performance, as used on the apparatus. Resistance was derived from current measurements through a shunt resistor, $R_0 = 1.00(1)\ \Omega$ and voltage across the coils at low test currents. Field characteristics and thermal properties were investigated by varying current through the coils in 5 A intervals from $I = 0 \rightarrow 50$ A for single coils and monitoring coil temperature by change in resistance, this is characterised as temperature rise per kW, K_i. Field strength was measured with a linear Hall effect sensor, (Honeywell SS94A1F) at a set distance from the centre the coil. This was used to calculate the field gradients when in anti-Helmholtz configuration with known separation, z_0, and relative position along transfer axis x_0. The results are summarised in Table 3.2.

Coil Pair	Resistance (Ω)	Average separation (mm)	Axial Gradient ($\frac{\mathrm{G}}{\mathrm{cm\ A}}$)	K_i °C/kW
I	0.25	78	1.6	50
II	0.39	113	1.7	
III	0.42	79	2.1	35

Table 3.2: Performance of our coil and cooling system. These are results for the coil pairs with current flowing in series while water is brought in parallel for the two Macor ® coil cases. Axial gradients for on-apparatus separations were calculated from measurements on the absolute field G/A at a fixed distance from a single coil. Temperature data for coil II is not relevant as it is only on for 0.8 s each 40 s

Noticeably, Coil pair I has a resistance approximately half that of the other coils owing to its small width and lower number of turns. During the magnetic transfer sequence this is undesirable as it forces too large a voltage drop across the controlling MOSFET resulting in failure. To remedy this a 0.2 Ω high-power resistor circuit is placed in series with the coil. The coolant is brought in parallel to the two Macor® coil cases resulting in a pump-limited flow rate of 3.8 → 4.5 L/min. The temperature rise with reference power allows the maximum sustainable power input to the electromagnets to be calculated. This is defined as the boiling point for the water bath, initially cooled to 20 °C, calculated to be 2 kW and 2.85 kW for coils I and III respectively. Long time thermal steady state maximum field gradients are then calculated as 170 G/cm and 210 G/cm, respectively. Our coils do not operate near these values, due to safety considerations and limited available current.

Ultimately, the achieved magnetic field is dependent on the highest sustainable current density, limited by the cooling efficiency and additionally dependant on potential power loss mechanisms such as switching elements and contact resistances of connected leads. To gauge the performance of our coils we compare our design with similar hollow core copper wire designs of identical volume as Coil III. A standard hollow copper square tubing (3.18 mm with a 1.55 mm bore) would occupy 24 turns and length of 8.2 m, assuming perfect winding $\lambda = 81$ %, dissipating 1 kW at 241 amps to achieve the same maximum field. A water flow rate of 0.40 L/min would be required for same temperature rises requiring a 12 bar power head, a 100-fold increase. Despite the lower operating power, the higher currents and large water pressure required may present practical challenges. We have thus developed a novel alternate design for low-current power supplies, which also only require low pressure water cooling.

3.5 Summary

This chapter surmises the bulk of the work completed in the first year of the project, encapsulating the design and construction of the crucial infrastructure of the apparatus. In particular the time was devoted to the development of the whole laser system, frequency and intensity stabilisation, and the optical system to deliver it to the vacuum apparatus. This vacuum chamber was built, baked and re-baked several times. Additionally, the main electronics necessary for control were designed and constructed. The timely process of designing and optimising of the coil system was also completed and their novel design and cooling capacity resulted in a technical publication [158]. From here, research work focussed on the experimental pathway to condensation that requires these backbone elements.

Chapter 4

Performance

After the main backbone infrastructure was set in place, we began the task of producing Bose Einstein condensates. This is a multi-step procedure that required:

1. Production of a high flux cold atomic beam in the 2D-MOT that could be forced through the differential pumping tube.
2. Capture of atoms from the atomic beam in the 3D-MOT.
3. Optimal number transfer from the 3D-MOT into a magnetic trap.
4. Magnetic hand-off procedure to move the cloud from the 3D-MOT chamber to the science cell.
5. Microwave induced evaporation and loading into a hybrid trap.
6. Optically induced evaporation to produce condensates.

The culmination of my time within the laboratory resulted in the production of ^{87}Rb condensates and ^{41}K 3D-MOTs. The procedure for condensation requires adequate performance of each discrete element and is summarised as follows. In our experiment the 2D-MOT first produces a beam of atoms that feeds the 3D-MOT. Once a sufficiently large number of atoms are captured the cloud is compressed and transferred to a purely magnetic trap. The three pairs of coils are then used to transfer the atoms from the 3D-MOT chamber into the science cell where they may be loaded into a hybrid trap consisting of a single 1064 nm dipole beam and the quadrupole magnetic trap. Subsequently, microwave evaporation can be used to cool the remainder ^{87}Rb atoms until a condensate is formed. In this chapter we discuss each step of the system in detail to quantify and evaluate the systems performance.

4.1 2D & 3D Magneto Optical Traps

The basis for a stable and efficient ultra-cold atom experiment is the ability to first capture and cool a large number of atoms. Here we do so with a 3D-MOT in line with the majority of BEC experiments. The future of our experiment relies on the simultaneous collection and cooling of ^{87}Rb and ^{41}K atoms, in the glass 3D-MOT chamber, fed by a cold atomic beam from the 2D-MOT chamber. The operating principles of laser cooling have previously been discussed in Section 2.1.

4.1.1 2D-MOT

In order to produce large atom-number condensates, a large number of atoms must first be trapped in the 3D MOT. Loading the 3D-MOT from a background gas, located in the same vacuum chamber, is not desirable as it restricts trapping lifetime and atom number. The differentially pumped system eliminates these issues by having the background source separate from the 3D-MOT. In order to feed the 3D MOT, a high-flux, low-velocity atomic beam is produced with a two-dimensional magneto-optical trap (2D MOT). A 2D-MOT can produce a well-collimated atomic beam with high flux of cold atoms quite easily. This is done by a pair of racetrack coils, which with current appropriately running through have a node along the central axis, with two pairs of orthogonal, counter propagating laser beams between them. This combination confines atoms to a cylindrical region at the centre of the apparatus. In reference to Fig. (4.1.1), this means atoms are trapped in the z and y direction, but free to move along x.

Here our racetrack coils are wound over rectangular aluminium forms, measuring 150×50 mm. 120 turns of 0.615 mm diameter copper enamelled wire was wound about these, and mounted around the 2D-MOT chamber such that differential pumping tube is centred between the coil pairs. This results in a spatial separation, between the inner faces of the coils, of 92 mm. This yields a transverse magnetic field gradient of 4.33 G cm^{-1}A^{-1}. In general, each coil has $2.5 \rightarrow 3$ A passed through them, producing an operational field gradient of $B' \simeq 13$ G cm^{-1}. This vanishes along the propagation axis that connects the 2D-MOT chamber to the 3D-MOT region. These coils were designed using the freeware Radia package, for Mathematica.

In order to cool atoms sufficiently, for them to remain in the magnetic node long enough to

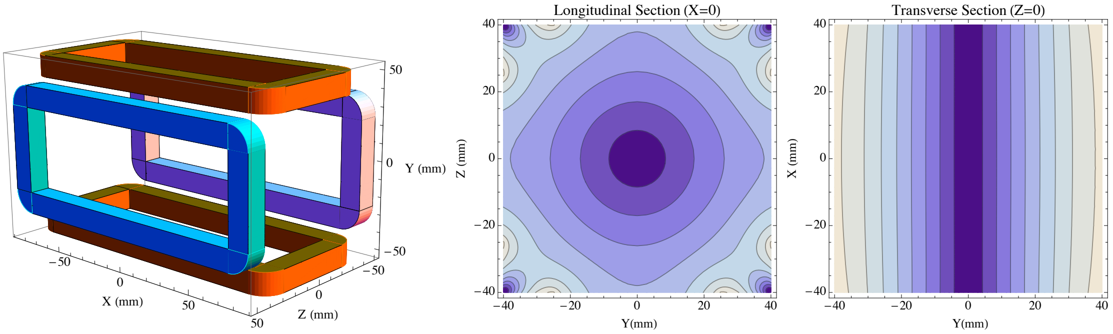

Figure 4.1.1: 2D-MOT racetrack coil design and field topography. (Left) The racetrack coils configuration of our 2D MOT. By running each pair in anti-Helmholtz configuration a node along the propagation axis (along the X direction) exists, seen in the field topography images (Middle) and (Right). As such Doppler cooling and trapping in the Z and Y is provided and atoms may move freely along the X-axis node to produce a 'beam' of atoms.

produce a beam, they must have a sufficiently long interaction time with the cooling beams. An atomic gas will have a thermal distribution of velocities as such, the most efficient way to produce a high flux atomic beam is to focus on cooling over a large area. Here this is accomplished by expanding the beams in one direction before passing them into the 2D-MOT chamber, Fig 4.1.3. The limiting factor in how wide the cooling area can be is the physical constraints of the system and power available. Here the windowed region of our 2D-MOT chamber limits us. 2D-MOT cooling light, fibre coupled from the main laser system, is brought to the 2D-MOT chamber and collimated to produce a 12.0mm diameter beam. These collimators also house quarter wave plates producing the circularly polarised light required for cooling. Before the beams are sent through the 2D MOT windows they are expanded along the propagation axis by a pair of cylindrical lenses. This cylindrical telescope consists of $f_1 = 50$ mm and $f_2 = 200$ mm lenses. The beam is then expanded, by a factor of 4, in the longitudinal direction of the 2D MOT. At this point, the beams are collimated and ready to project through the 2D MOT chamber. The counter-propagating beams are supplied by retro-reflecting these beams, with prism retroreflectors Fig. (4.1.3) (c). While this reflected beam will have a reduced power, compared to the incident beam, this power loss is negligible for 2D-MOT operation. This method is desirable as it mitigates the need for extra power and infrastructure of two additional beams.

The 2D-MOT beams, altogether, contain four different frequencies of light. The horizontal beam has ^{87}Rb cooling light, and both the cooling and repump light for ^{41}K. The vertical beam, however, contains these three frequencies as well as ^{87}Rb repump. This configuration provides Doppler cooling in two-dimensions, resulting in atomic vapour localisation about the node of the

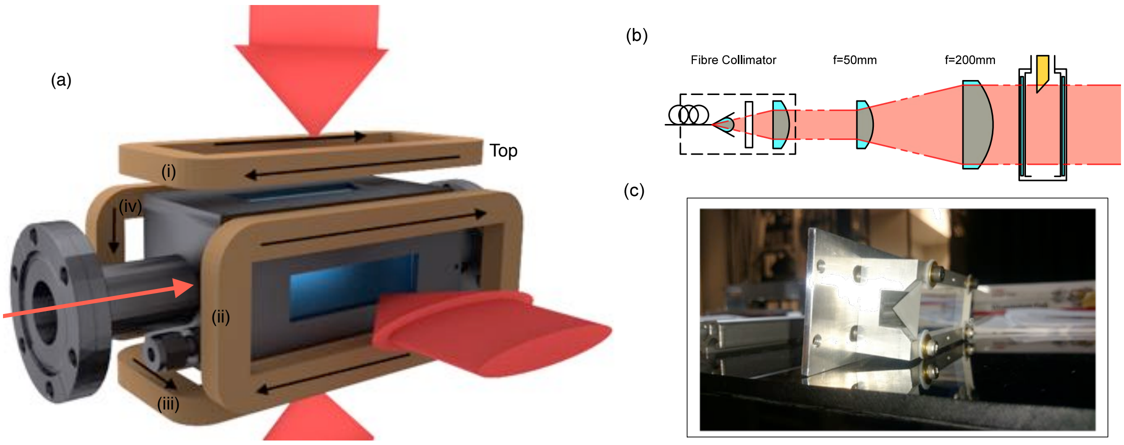

Figure 4.1.2: (a) Schematic of the two-dimensional MOT illustrating the how the cooling beams and racetrack coils operate. First light must be expanded along the propagation axis via a cylindrical telescope (b) before they are retroreflected by prisms (c) to produce the counter propagating beams. This provides transverse cooling of the atomic beam while the atoms thermal velocity along the longitudinal 2D MOT axis allows a beam to form. A 'push' beam directed along the beam direction enhances the flux immensely.

quadrupole field. A low power push beam, derived from the 2D-MOT beams in the laser system, promotes atomic flux through the differential tube into the UHV section of the vacuum system, where they may be collected in the 3D MOT. Independent control of each coils magnetic field contribution and 2D-MOT beam alignment and power allow for tweaking of the 2D-MOT.

The 2D-MOT produces a two-dimensionally confined cloud that will move through the differential pumping tube as a bright atomic beam. Although no explicit dampening of motion along the beams axis exists the physical dimensions of the differential tube and filtering effect of the 2D-MOT can keep the atomic beams mean speed as low as $\langle v_z \rangle \simeq 20$ m/s [170]. This is due to the fact that only atoms with relatively low axial velocity will spend enough time in the trapping region to experience sufficient atom-light interactions to pass through the differential tube. Optimal power and detunings are presented in Table 4.1. Normally the 2D-MOT is operated for $10 \rightarrow 15$ s at which point the number of atoms in the 3D-MOT saturates. Loading ^{87}Rb, atoms into the 3D MOT, at a rate of $\simeq 2 \rightarrow 5 \times 10^8$ atoms sec^{-1}. Numbers on ^{41}K load rates are currently unknown but the 2D-MOT can create an atomic flux of ^{41}K. The total flux, from the 2D-MOT, is most likely not optimised as the power and detunings are optimised on the 3D-MOT atom number and not the atomic flux.

The end of the copper differential tube is cut and polished to produce a 45 ° titled mirror. This mirror allows us to send a hollow beam along counter to the atomic flux, to reduce the

Laser Parameters			
2D Magneto Optical Trap			
Beam	Detuning [Γ]	Power/beam [mW]	Intensity [mW/cm^2]
^{87}Rb 2D Cooling	-2.75	38	8.4
^{87}Rb 2D Repump	0.0	3	0.7
^{41}K 2D Cooling	-2.5	35	7.7
^{41}K 2D Repump	-3.0	35	7.7
^{87}Rb Push Beam (Cooling)	-2.75	0.4	4
3D Magneto Optical Trap			
Beam	Detuning [Γ]	Power/beam [mW]	Intensity [mW/cm^2]
^{87}Rb 3D Cooling	-2.75	8	7.1
^{87}Rb 3D Repump	0.0	4	3.5
^{41}K 3D Cooling	-2.0	10	8.8
^{41}K 3D Repump	-4.0	8	7.1

Table 4.1: Summary of the 2D/3D-MOT parameters that produce optimal ^{87}Rb & non-optimised ^{41}K. Detuning of beams refer to the $|F=2\rangle \rightarrow |F'=3\rangle$ and $|F=1\rangle \rightarrow |F'=2\rangle$ transitions for the cooling and repump beams, respectively.

velocity distribution. This may be beneficial to produce lower velocity atomic beams that may enhance our capture rate and atom number in the 3D MOT, but has not yet proved necessary to implement.

In summary, the 2D-MOT is fully operational and continues to effectively produce cold atomic beams of ^{87}Rb and ^{41}K beams, which can be captured in the 3D-MOT.

4.1.2 3D-MOT

Once the laser infrastructure and coils of the 2D MOT were sufficiently aligned and optimised both it and the 3D MOT performance could be evaluated. The 3D MOT (laser schematic shown in Fig (4.1.4) (a)) consists of three pairs of orthogonal, counter propagating beams that intersect at the centre of the glass octagon. Shown in the schematic are the two planar pairs while the vertical beams are entering and leaving the page respectively. Unlike the 2D MOT the counter propagating beams could not be formed from retroflections, as the expected loss in power would cause a non-negligible asymmetry at moderate powers that would hamper the performance. The vertical beams are sent along the planar axis before being reflected into/out of the page.

Each 3D MOT beam contains cooling light for ^{87}Rb cooling and both 3D cooling and 3D repump frequencies for ^{41}K. These beams are expanded from the fibre and collimated to 25.4 mm diameter. The light has its polarisation set to be circularly polarised by quarter waveplates, as required for correct operation of the 3D-MOT. Having these polarisations set to within a few

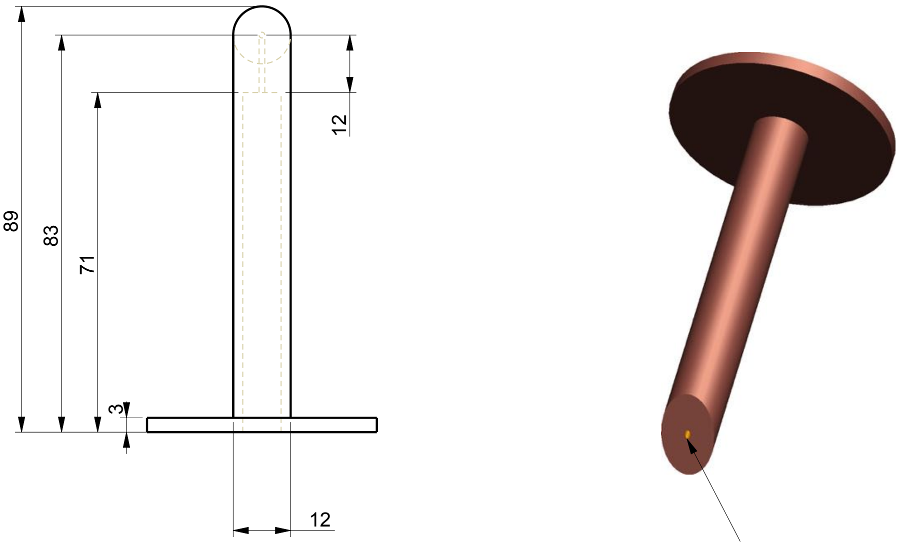

Figure 4.1.3: Schematic (left) and render (right) of the differential pumping tube showing the tilted mirror and the two-stage bore in through the centre, units in mm. Proximal to the opening, at the mirror end, the conductance is limited by a small aperture tube which then is then opened to a larger tube.

percent was found to be crucial for highly symmetric, large atom number MOTs. ^{87}Rb repump is brought in separately, collimated to a 25.4 mm diameter beam and brought in from the science cell end of the experiment. Repump is brought in from this direction as it can then be used, regardless of the location of the atomic cloud, whether at the 3D-MOT location or at the science cell. Alignment of MOT beam pairs is done by aligning one to the centre of the two windows of the glass octagon, with the reciprocal laser aligned to this beam, ensuring symmetry. Centred above and below the glass octagon is coil pair I, housed in the Macor holds. During 3D-MOT operation 6.6 A are passed through the coils to generate the three-dimensional quadrupole field with a gradient of $B' = 10.5(5.3)$ G/cm in the axial (radial) direction. Using typical powers and detunings, shown in Table 4.1, $3.0 \rightarrow 5.0 \times 10^9$ ^{87}Rb atoms, and an unmeasured number of ^{41}K atoms, may be caught at the centre of the glass octagon. An absorption and fluorescence image of ^{87}Rb and ^{41}K atomic clouds is shown in Fig (4.1.4) (b) & (c) respectively. We are able to produce each of these clouds separately as well as concurrently illustrating the point at which the experiment became officially ‘dual-species’.

In short, the 3D-MOT adequately contains large numbers of ^{87}Rb and some ^{41}K that can be used to move towards producing Bose Einstein condensates. In order to troubleshoot our apparatus, techniques and methods it was elected to focus on doing so initially for ^{87}Rb. Expe-

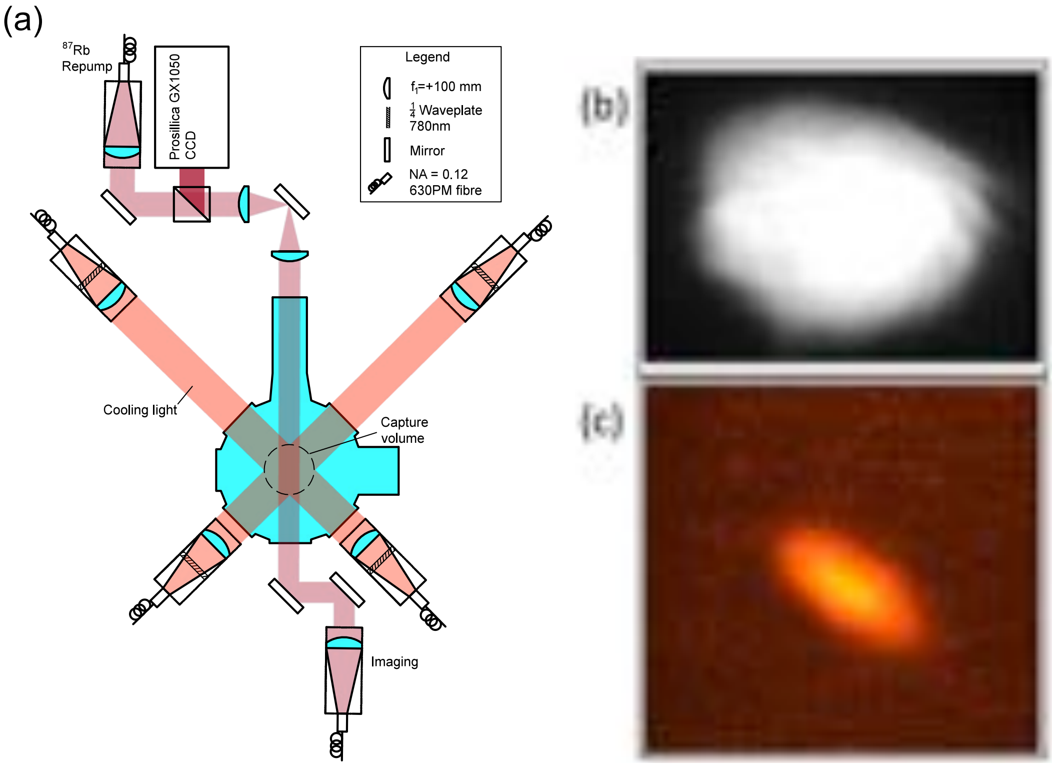

Figure 4.1.4: (a) Schematic of the 3D MOT optics set up showing four of the six cooling beams, the ^{87}Rb repump and imaging path. The imaging system is out of focus in regards to the atomic cloud at the 3D MOT location and spatial information cannot be obtained while atom number can. (b) Fluorescence image of a ^{87}Rb cloud and (c) fluorescence image of a ^{41}K cloud.

rience and literature on what constitutes adequate performance for rubidium is abundant, and therefore any systematic errors could easily be determined by only looking at this one species. If we had attempted to simultaneously progress with both species, any difficulties arising from interspecies interactions would not be readily distinguishable from systematic problems. As a result the remainder of this thesis deals only with ^{87}Rb.

4.2 CMOT, Magnetic Trapping and Transfer

The initial cooling and trapping of atoms in the MOT stage produces cool and relatively dense samples, where temperatures of the order of 100 μK are reached. Yet atoms still have a gain several orders of magnitude in their phase-space density before the emergence of a BEC is expected. This is not possible with dissipative confinement of magneto-optical traps. Due to the stochastic nature of heating, due to multiple absorption and reemission cycles, any further reduction in temperature is not possible. A way to avoid this is to load the atoms into a purely magnetic trap, where no atom-photon processes take place. From here a range of pathways are available to move towards quantum degeneracy. Here, this involves moving confinement from the 3D-MOT to a purely magnetic trap, before transferring the cloud to the science cell. Subsequently, additional cooling can be done to reach low enough temperatures such that a condensate emerges from thermal profile. Here we discuss the methods and performance for the initial magnetic trapping and transferring procedure.

4.2.1 CMOT, Bias field and Magnetic Trapping

In general, purely magnetic traps require a much larger field gradient to compensate for the loss of the optical molasses beams as the atoms move out of the 3D-MOT. This corresponds to a smaller cloud volume, but the atoms have the same phase-space density. Thus, prior to loading, the atomic cloud must be compressed in what is known as CMOT [171]. In particular we have to compress the atomic ensemble enough so as thought it can efficiently load a 100 G cm^{-1} magnetic trap, starting from the 10.5 G cm^{-1} gradient in the 3D-MOT. If the magnetic field is rapidly switched, from the MOT value to 100 G/cm, atoms farthest away from the centre would receive large increase in energy resulting in excessive heating and losses. CMOT prevents this by significantly increasing the density of the cloud, while also reducing the temperature. This is accomplished by red-detuning the cooling beam away from resonance and simultaneously reducing the repump power. As a result, the outward light pressure from within the atomic ensemble is reduced as the scattering rate decreases. The result is a cloud with less atoms but higher phase space density compared to the standard MOT. Within this experiment, the ^{87}Rb cooling light is scanned from $-2.75\ \Gamma \rightarrow -10\ \Gamma$ linearly over 40 ms with the repump power is decreased to $\approx 10\%$ of its initial value.

Following this compression a large fraction of atoms reside in the $|F = 1\rangle$ manifold as the power in the repump light is not sufficient cycle them back into the $|F = 2\rangle$ state. We further encourage this by a 2 ms optical depumping stage where the repump is completely switched off and the cooling light remains on. This forces the remainder of atoms to move to the $|F = 1\rangle$ state. This ensures a purity of spin states in the magnetic trap, as only atoms in the $|F = 1, m_F = -1\rangle$ level are magnetically trappable. This purity of states is, allegedly, crucial to forming a dual-species condensate of ^{87}Rb and ^{41}K, as discussion with the Inguscio group has indicated that spin mixtures result in prohibitive losses. During CMOT and the depump process, the magnetic field is held at an axial gradient of $B' = 10.5$ G/cm. At their conclusion the magnetic field gradient is rapidly changed to 60 G/cm (30 A), trapping 50 → 60 % (1.5×10^9 atoms) of atoms originally held in the 3D-MOT. Following this the gradient is increased to 100 G/cm (60 A) over 100 ms. While precluding any formal, or intentional, sub-Doppler cooling processes, the ^{87}Rb atoms re-captured in the magnetic trap, when optimised, are generally colder then the Doppler temperature, sitting at 80 μK. We are okay with this.

Cooling beam detuning, sweep times and power reduction of the repump are all parameters that must be optimised in CMOT. However, to prevent heating and thus achieve the highest phase space density within the magnetic trap, the CMOT cloud centre must be well aligned with that of the magnetic trap. This means the six orthogonal MOT beams must be well aligned and power balanced. This is observed by looking for isotropic expansion of the atomic cloud when the magnetic field is switched of, as well as the persistence of the molasses. However it is difficult to perfectly align the centre of the MOT beams with the zero of the quadrupole field. In order to fine-tune the field minimum, for optimal magnetic trap loading, three small electromagnets are used to 'push' this minimum about. These coils consist of 40 turns of 0.6 mm diameter enamelled copper wire wound to 50 mm diameter. These three single coils were placed orthogonally and as close to the cell as possible, however more recently coil pairs have been added and show greater stability. . Small currents can be passed through them to compensate for small misalignments and spurious magnetic fields. The current through theses coils is not permanently fixed as small drifts in alignment or power balance, in the MOT beams, generally requires the occasional 'tweaking' of bias coil current. Generally, however, they have 400 → 900 mA passing through them. The precise numbers are determined by maximising the atom number and temperature of atoms transferred into the magnetic trap.

4.2.2 Magnetic Trapping and Transfer

Once the atomic cloud is loaded in the magnetic trap it has to be adiabatically transported 104 mm until it resides 20 mm from the end of the science cell, adiabatically. Several methods to do so exists, each with their own distinct set of advantages and disadvantages. Some of these include using moving optical tweezers [172, 173], physically moving a quadrupole producing pair of coils [174, 175, 176] and through a magnetic 'hand-off' procedure through a chain of static magnetic coil pairs [165]. We elected to perform a magnetic hand-off procedure to transfer our atomic cloud. The optical tweezer method was discounted as vibrational and long-term stability was considered prohibitive and physically moving a single coil pair precludes the volume it sweeps out. This would complicate using our microscope objective lens to image the cloud.

The coil chain transfer technique has the advantage of structural and vibrational stability, provided it is designed adequately, and allows for high optical access. Disadvantages of this technique are the need for additional electronic control circuitry and increased electrical power requirements. These elements can be mitigated by using as few coils as possible and making certain their design.

Theory

Transfer is accomplished by moving the magnetic field minima from the initial magnetic trap location to the science cell. This corresponds to application of appropriate current ramps through the three coil pairs that surround that 3D-MOT vacuum chamber, Fig (4.2.1). Initially the atomic cloud lies at the magnetic minima of the quadrupole field produced by a single coil pair. As the current in the neighbouring coil is increased the centre of the trapping potential is moved, which the atomic cloud can follow. However, the atoms are no longer contained in a strictly quadrupole field, and the 'shape' of the atomic cloud changes following the topography of magnetic field. As the current in the second coil pair continues to increase, the cloud continues to be displaced towards its centre point. By repeating this procedure, with multiple pairs of coils, an atomic cloud can be transferred over a large distance.

When a coil chain system contains many coil pairs the transport procedure results in the repetition of the aforementioned transfer process. If done over several coils, the modulation of the traps aspect ratio could cause heating of the atomic ensemble. In order to combat this an additional third coil pair can be used. This allows the cloud to be transferred from one location to the either in a single trap geometry, not consistently stretching and compressing. This aids in adiabatically moving the cloud. In practice, however, a change is aspect ratio has to occur at the beginning and end of the transfer sequence.

The axial, B_z, and radial, B_r, component of magnetic field, produced from a single magnetic

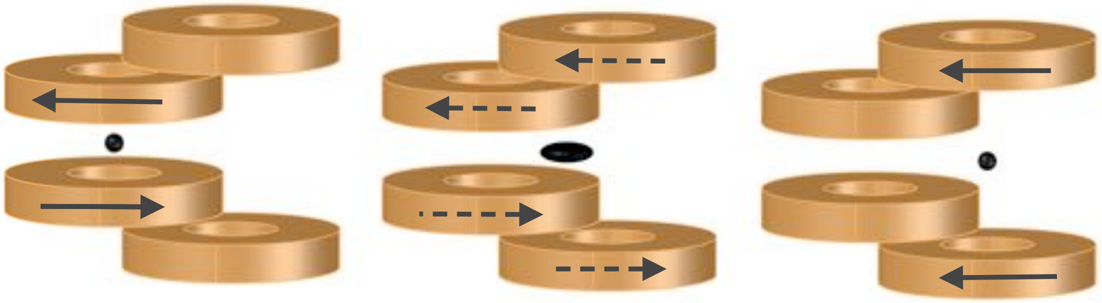

Figure 4.2.1: Illustration of the magnetic transfer technique for a two coil pair. First an atomic cloud is held in a quadrupole magnetic trap by a single pair of coils. An adjacent overlapped pair is then turned on and the shape and location of magnetic minima changes, which the atomic could follows. By applying the appropriate current ramps the atomic cloud may be transferred through a series of multiple coils.

coil is given by,

$$B_z = \frac{\mu_0 I}{2\pi\sqrt{z^2+(a+r)^2}}\left(\frac{a^2-z^2-r^2}{z^2+(r-a)^2}E_2(k^2)+E_1(k^2)\right) \tag{4.2.1}$$

$$B_r = \frac{\mu_0 z I}{2\pi r\sqrt{z^2+(a+r)^2}}\left(\frac{a^2+z^2+r^2}{z^2+(r-a)^2}E_2(k^2)-E_1(k^2)\right), \tag{4.2.2}$$

where z and r is the axial and radial distance from the centre axis of the coil, a is the radius of the coil, and $k^2 = \frac{4ra}{z^2+(a+r)^2}$, $E_1(k^2)$ and $E_2(k^2)$ the complete elliptic integrals of the first and second kind respectively. The total field strength given by $|\mathbf{B}|^2 = B_z^2 + B_r^2$.

As mentioned, this experiment has three pairs of electromagnets that are used to transfer the cloud from the 3D-MOT location to the science cell. To do so adiabatically we must slowly move the field minima while attempting to minimise changes in the clouds aspect ratio. Ideally we transfer the cloud with a fixed magnetic field gradient and keep the centre of the cloud at a magnetic field zero. This can be done by finding the appropriate current through each coil for a given position along the transfer axis. By using the equations for the axial and radial fields (B_i), and their derivatives $(B_i'x)$ as well we can set up a linear system of equations to find the current, I_i, through each coil at a given position.

$$\begin{pmatrix} B_1 & B_2 & B_3 \\ B_{1x}' & B_{2x}' & B_{3x}' \\ B_{1z}' & B_{2z}' & B_{3z}' \end{pmatrix}\begin{pmatrix} I_1 \\ I_2 \\ I_3 \end{pmatrix} = \begin{pmatrix} 0 \\ B_x' \\ B_z' \end{pmatrix} \tag{4.2.3}$$

This set of equation ensures that for any point, x, along the transfer axis the total field is zero, and the axial and transfer magnetic field gradients B'_z and B'_x are fixed. However, as the atomic cloud must start and finish in a stationary quadrupole field, it has to be ramped to these transfer gradient values. The most crucial point, then, is to determine these transfer field gradients, which are subject to a variety of limitations and constraints.

Transport Considerations

The heuristic for successful magnetic transfer, of our atomic cloud, is adiabaticity of the procedure. This requires that the cloud does not undergo any heating and atoms are not lost from the trap. This is also influenced by the infrastructure related limitations such as the heat dissipation capabilities of the coils, their physical size, and the amount of current available to be passed through the coils.

The first consideration is supporting the cloud against gravity, such that losses are not an issue. The minimum field gradient required to support atoms against gravity is given by,

$$B'_g = \frac{mg}{g_F m_F \mu_b}. \tag{4.2.4}$$

For ^{87}Rb atoms trapped in the $|F = 1, m_F = -1\rangle$ magnetic substate this gives an axial gradient requirement of $B'_z = 30.5$ G cm^{-1}. Similarly, as atoms must be moved accelerated and decelerated from/to rest, at the start and end of the transfer procedure, they are subject to accelerations in the transfer direction. The field gradient must be sufficient to support the cloud against this. For a given field gradient, in the transfer direction, the maximum acceleration is given by,

$$B'_y = \frac{ma_y}{g_F m_F \mu_b}. \tag{4.2.5}$$

To minimise transfer time, and therefore opportunities for losses via Majorana spin flips and other methods, we wish to accelerate the cloud as fast as possible, meaning as large a trap gradient as possible. This is limited by the amount of current available and the heat dissipation capabilities of the electromagnet cooling system. Here, the cooling capacity is not an issue, and we are wholly limited by the maximum current our power supply can output, 100 A. With this constraint, and having a radial aspect ratio of $B'_x/B'_y = 1.7$ as suggested in literature [165, 177], we are limited to transfer gradients of $B'_z = 100$ G cm^{-1} and $B_x = 64$ G cm^{-1}. This provides a

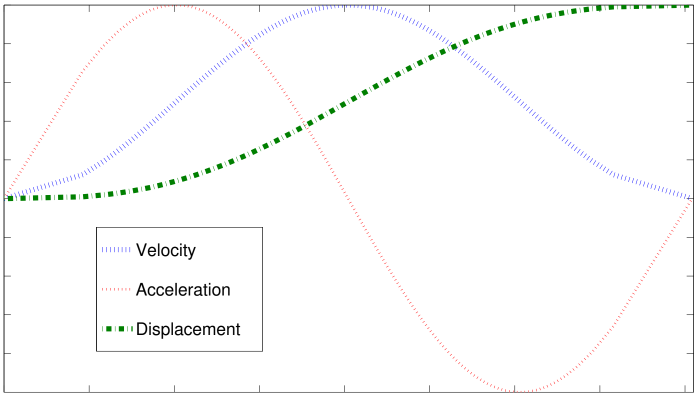

Figure 4.2.2: Velocity, acceleration and displacement profile of a transfer sequence of the modified 'Hanning Window' variety. Axes are arbitrary for each profile, showing 'smoothness' at which a cloud may be accelerated.

maximum transport acceleration of $a_y = 5.8$ m s^{-2}.

Using these gradients, the linear current system can be solved along the transfer axis, $x = 0 \rightarrow$ 104 mm, yielding a function of current in terms of spatial position. However, in the laboratory this is a temporal problem and $\mathbf{I}(\mathbf{x})$ must be transformed to $\mathbf{I}(\mathbf{t})$. If a linear conversion is applied the cloud is abruptly accelerated and decelerated multiple times throughout the transfer process. This was our initial method, however heating and atom losses were prevalent. To eliminate this the cloud must have its velocity slowly increased to prevent abrupt accelerations. We do so by forcing the atoms to have a Hanning window velocity profile. From this we can also gain expression for the displacement and acceleration of the cloud:

$$x(t) = kt - \frac{ck}{2\pi}\sin\left(\frac{2\pi}{c}t\right), \tag{4.2.6}$$

$$v(t) = k - k\cos\left(\frac{2\pi}{c}t\right), \tag{4.2.7}$$

$$a(t) = \frac{2\pi}{c}k\sin\left(\frac{2\pi}{c}t\right). \tag{4.2.8}$$

Using the constraints outlined above ($v(0) = 0$ m s^{-1}, $max[a(t)] < 5.8$ m s^{-2}) the constants c and k can be found for a variety of maximum accelerations. The precise functional form the acceleration, velocity and displacement profiles are shown in Fig (4.2.2).

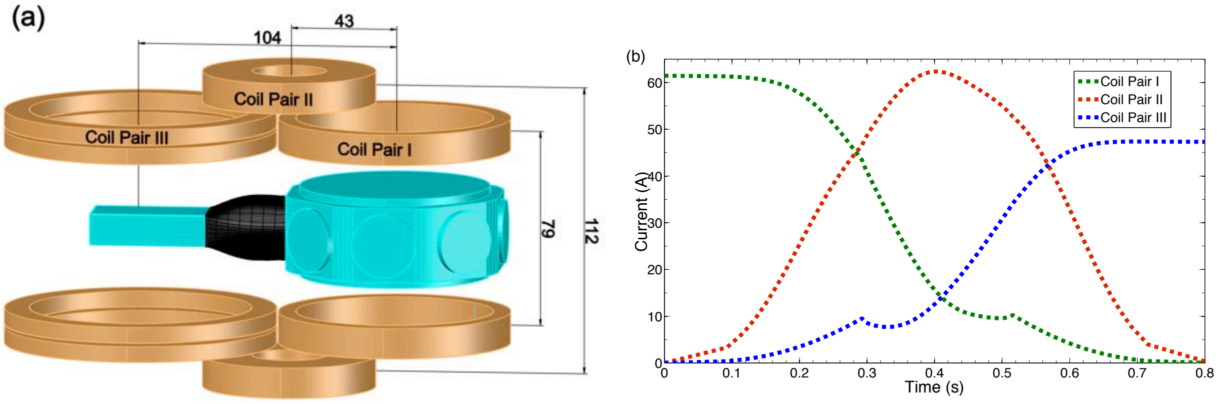

Figure 4.2.3: (a) Illustration of the transport coils dimensions. The atomic cloud is transferred from the centre of coil pair I to the centre of coil pair III at steady state axial gradient of $B'_z = 100$ G cm^{-1} and axial aspect ratio of $B'_y/B'_x = 1.7$. This is done in 810 ms by the application of current ramps through each coil (b).

System and Performance

With a smooth acceleration profile and knowledge of the steady state transfer magnetic field gradients the system is almost ready to transfer the cloud. The final consideration is the fact that due to the finite overlap of the coils, restricted by the amount of optical access required through their centres, the currents required to transfer the cloud at the beginning and end of the sequence at the desired field gradients is not always feasible. To mitigate this we use linear ramps, on the current, to move it to the point where a solution first exists. This holds the axial gradient at 100 G cm^{-1} while changing the radial fields. This is done for the first and last 25 mm of the transfer sequence.

Several current ramps, with differing maximum accelerations, were used to test the performance of the transfer sequence. All ramps with a maximum acceleration less than 3 m s^{-2} would adiabatically transfer the entire atomic cloud, any faster and losses were present. As ^{41}K will be implemented into the transfer sequence in the future, a maximum acceleration of 1 m s^{-2} was chosen to accommodate its smaller mass. This transfer takes a total of 810 ms, with the current through each pair of electromagnets shown in Fig (4.2.3) (b). At the end of the transfer sequence approximately $1.0 \rightarrow 2.0 \times 10^9$ ^{87}Rb atoms routinely reside in the science cell at 90 μK, demonstrating negligible atomic losses from the trap and minimal heating of the ensemble. As a result the atomic ensemble sits in a $B'_z = 100$ G/cm quadrupole field produced by coil pair III, primed for microwave evaporation.

4.3 Microwave Evaporation and the Optical dipole trap

Once we have efficiently transferred the atoms to the science cell, the ^{87}Rb atoms are ready to undergo a two-stage evaporative cooling procedure to force the transition to a Bose-Einstein condensate. The first step is microwave evaporation to first reduce the temperature of the ensemble. Additionally this stage will also be used to sympathetically cool ^{41}K. This reduction is temperature also results in a smaller atomic cloud that is now mode-matched to be loaded into a optical dipole trap where optical evaporation can be used to produce a condensate.

4.3.1 Microwave Evaporation

Generally, when evaporating a single species it is common to make use of radio-frequency (RF) transitions from the trapped to untrappable states. This method is preferred as signal generators and amplifiers in the RF category (kHz to MHz) are readily available. Unfortunately the Zeeman substate splitting for ^{41}K and ^{87}Rb are almost identical and RF evaporation on one of the atomic species would also evaporate the other leading to depletion ^{41}K. Fortunately, the large hyperfine splitting of ^{87}Rb (6.835 GHz) is far from resonance for ^{41}K, making it a viable transition for the evaporative cooling of ^{87}Rb. In particular, we selectively eject hot ^{87}Rb atoms from the magnetic trap via the $|F, m_f\rangle = |1, -1\rangle \rightarrow |2, -1\rangle$ transition.

Production & Performance

In order to perform microwave evaporation, we must first produce the signal to irradiate the atomic ensemble. We accomplish this via the circuit shown in Fig (4.3.1). First, a Valon 5008 dual frequency synthesiser produces ≈ 15 dBm at 2.950 GHz, before being frequency doubled to 5.900 GHz. Near resonant radiation is then produced by mixing the frequency doubled Valon signal with a 0.925 GHz signal produced by a programmable Holzworth HSM2001A RF generator. It is this element that allows the microwave radiation to be brought closer to resonance. Before amplification, a series of filters remove other frequencies that are produced during the mixing process, suppressing noise. Sufficient power must be applied to the atomic cloud in order for the evaporation process to be efficient. Thus, prior to irradiating the atomic cloud, the signal is amplified. A Khune PA 7000 A amplifier is used, producing 4 W of power. Circulators are used to protect any high power back reflections from damaging the circuit. After amplification, the radiation is sent through an impedance-matched horn, which delivers the radiation to the atomic cloud.

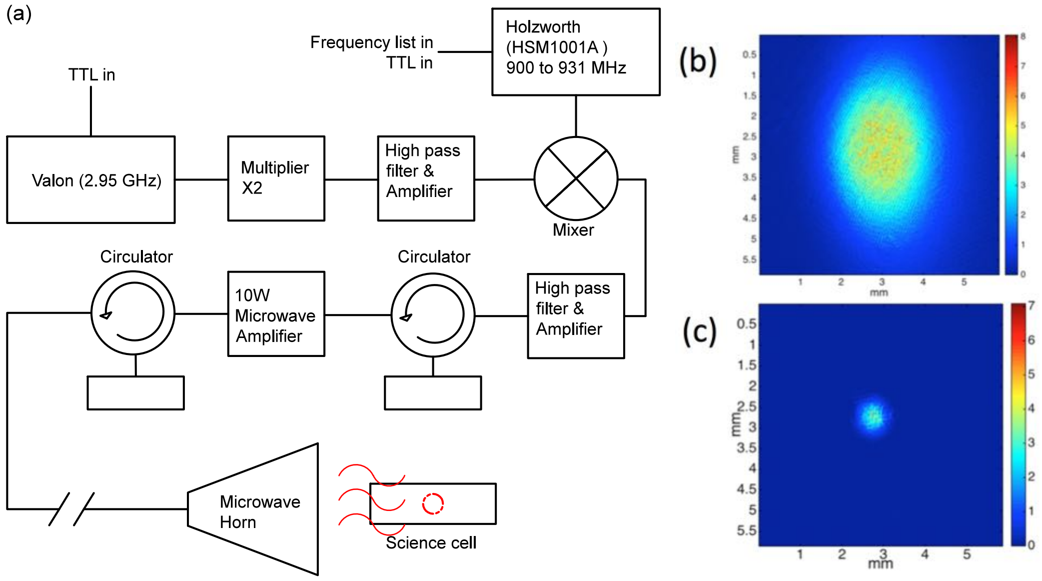

Figure 4.3.1: (a) Circuit for producing the microwave radiation to evaporatively cool ^{87}Rb atoms trapped in a $B_z' = 160$ G cm^{-1} quadrupole field. Over a 5 s ramp 1×10^9 atoms at 100 μK (b) are irradiated during the sweep until 50×10^6 atoms at 20 μK remain (c).

One limiting factor for how fast atoms may cool is the rate at which atoms rethermalise. This is closely related to the magnetic field gradient atoms reside within. In particular, the stronger the magnetic field gradient the faster evaporation may proceed. As such, the current through the quadrupole coils (pair III) is ramped from 47.6 A ($B_z' = 100$)G cm^{-1} to 76.2 A ($B_z' = 160$ G cm^{-1}) over 600 ms prior to beginning the evaporation sequence. Immediately following this, the microwave radiation is switched on and the evaporation ramp moves the frequency from 6.825 GHz to 6.830 GHz in 5 s. In this sequence 1×10^9 atoms at 110 μK are evaporatively cooled until 5.0×10^7 atoms at 20 μK remain.

4.3.2 Hybrid Trap

Quadrupole potentials have many advantages when used in creating BECs. In particular, their large trap volumes and tight confinement allow for efficient evaporative cooling. They are also experimentally easy to produce by way of anti-Helmholtz coils while being physically unobtrusive. Unfortunately Majorana spin-flips limit phase-space densities to those too small for the emergence of the BEC transition. These may be mitigated by using additional coils to remove the magnetic field zero, but this is not always desirable. Similarly, all-optical techniques are not well mode-matched to an atomic cloud from a 3D-MOT, resulting in small atom number BECs. Here we

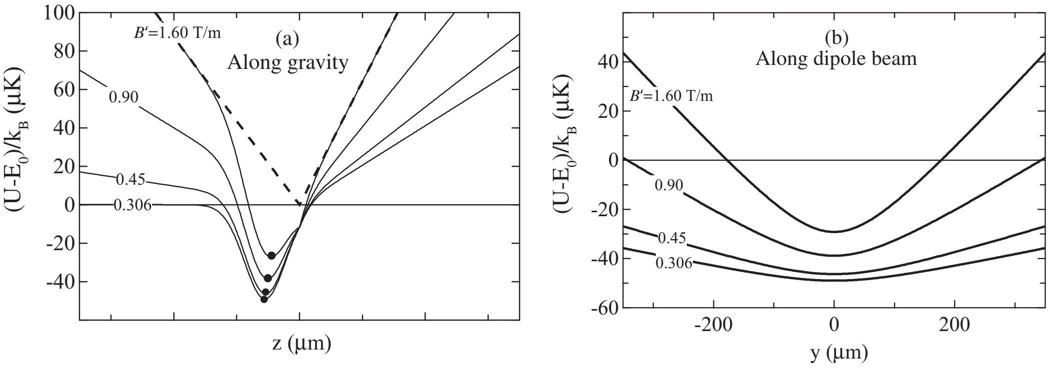

Figure 4.3.2: (a) Cross-section along gravity (axial direction of the quadrupole field) showing the potential minima as the field gradient is reduced below support at the field zero. Atoms may then fall into the hybrid trap and be removed from the zero point. (b) Cross section along the beam propagation axis. While confinement becomes weaker the residual field from the quadrupole potential remains creating an aspheric harmonic potential in which evaporative cooling may occur. Images taken from [127]

make use of a hybrid trap, using both optical and magnetic fields, to best prevent these issues.

A hybrid trap consists of an optical dipole trap, suspended below the trap zero of a quadrupole field. By using the increased phase-space density, of the microwave evaporated cloud cooled to the point where Majorana losses become significant, atoms can be efficiently transferred into the optical dipole trap. The transfer procedure requires the reduction of the magnetic field gradient until it no longer compensates for gravity; atoms may then fall into the dipole beam potential, Fig (4.3.2). The magnetic field remains on, at this lowered field gradient, such that an additional confinement of the atomic ensemble exists in the weak direction of the dipole trap. The beam is beneath the field zero such that Majorana losses are no longer present. Once atoms are loaded into this trap, evaporative cooling is done by lowering the optical trap power and allowing high energetic atoms to escape from the wings of the confining beam until a condensate is formed [127].

1064 nm Laser

The light for our optical dipole trap is supplied by a 20 W, 1064 nm, single-mode Keopsys Ytterbium fibre laser, with a 5 MHz line width. The output is fitted with an isolator, for protection against back reflections, and a collimator, providing a collimated $1/e^2 = 2.6$ mm diameter beam. Being 1064 nm, the light is far red-detuned from resonance for both ^{87}Rb and ^{41}K, forming an attractive, nearly conservative potential. After the fibre head the beam is quickly reduced to a collimated 1.3 mm diameter beam before being split into three separate beams, Fig (4.3.3). A zero-order 1064 nm half wave plate and polarising beam cube is placed directly after the fibre head to control the power.

Each beam passes through an AOM, and the diffracted order coupled into an optical fibre. The acoustic-optic modulators (Goouch and Housego 3110-197 110 MHz), have an active aperture of 1.25 mm diameter necessitating the reducing telescope. The AOMs are present in order to have variable control over the power entering the fibre and to create frequency gap between the beams. This is important to prevent optical interference between the beams. Currently, only the ODT1 beam, derived from the first beam, is used on the experiment. We take the -1 order of the AOM that diffracts with 85 % efficiency. The AOMs are controlled by a voltage controlled oscillator $\rightarrow$ mixer $\rightarrow$ RF switch $\rightarrow$ amplifier circuit. The RF switch enables acute toggling of the light, while the mixer is used as a controllable attenuator into the amplifier to change the diffraction efficiency of the AOM and thus power in to the ODT1 fibre. In particular, we make use of this circuit element to intensity stabilise the output power of ODT1. This is crucial, as optical dipole traps necessitate high powers, which actively drift as optical elements heat and change efficiency/focus etc. Before being brought over to the main experimental chamber, with the ODT1 fibre, the beam is passed through another telescope that expands the beam to 3.75 mm diameter. Once again, due to the large powers delivered, it is good practice to use high mean field diameter (MFD) fibres, here a Thorlabs 1064 nm, MFD= 7.7 μm PM fibre, to mode match and distribute the energy as best as possible. Failure to do so may result in damage to the fibre or reduction in coupling efficiency. This coupling has an efficiency of $\simeq 80$ % when well aligned.

Additionally, ODT2 is coupled to the main experimental region but not yet used on the experiment. The fibre that brings this beam over, is an in-house connectorised fibre with a double-clad core, (Nufern PLMAS-GDF-400).

Procedure and Performance

At the main experimental chamber the beam is focussed from the 3D-MOT chamber end to the science cell chamber by a 300 mm lens, down to a waist of $w_0 = 70$ μm, Fig (4.3.4). The focus is offset below the quadrupole zero, by $z_0 = 100$ μm. Further, it was found necessary to prevent any back reflections, of the 1064 nm beam, from overlapping the incident beam. We initially observed Raman transitions that depleted the hybrid trap and prevented achievement of BEC. To load the trap, after microwave evaporation, the quadrupole field is ramped from $B'_z = 160$ G cm^{-1} to 29 G cm^{-1} over 3 s. As the magnetic field no longer supports against gravity, atoms are able to move into the dipole trap. We have found that leaving the microwave radiation on,

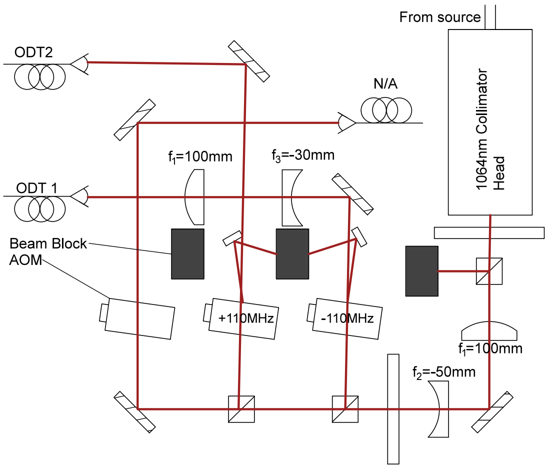

Figure 4.3.3: Schematic of the 1064 nm light apparatus. The light is split into three separate beams, two optical dipole trapping beams (ODT1 & ODT2) and a third, which may be used as a sheet beam. However currently this is not required and remains for future projects. ODT1 and ODT2 are shifted 220 MHz from another in order to prevent interference effects when overlapped.

while ramping the magnetic field down, and bring it 2 MHz towards resonance the optical dipole trap would load more efficiently. This microwave radiation is switched off after the magnetic field decompression. The dipole beam delivers $\simeq 2.8$ W to the cloud location, at a trap depth of 49 μK. The majority of this power is sent to a beam block at the back of the system while one percent of the light is sampled by a photodetector sending this level to the intensity lock. The signal from the photodetector is fed into a circuit which compares the light level to a user defined level. If there is a discrepancy the circuit will alter the input into the mixer of the AOM driving circuit. This will change the diffraction efficiency of the AOM until the signal levels are equal. This circuit is stable, keeping fluctuations to < 1 %. A complete description of this PID intensity stabilisation circuit is given in [178]. At the end of the transfer sequence $5 \rightarrow 10 \times 10^6$ atoms at 4(2) μK are transferred into the dipole trap.

4.4 Absorption imaging

The atomic ensemble, at each step in the sequence towards condensation, is directly observable through absorption imaging. Our experiment is equipped with three imaging pathways, including one high-resolution path in the vertical direction and two horizontal imaging beams in the experimental plane. A schematic of these horizontal beams is shown in Fig (4.4.1). The primary beam, through which all quantitative data in this thesis derives from, provides one-to-one imag-

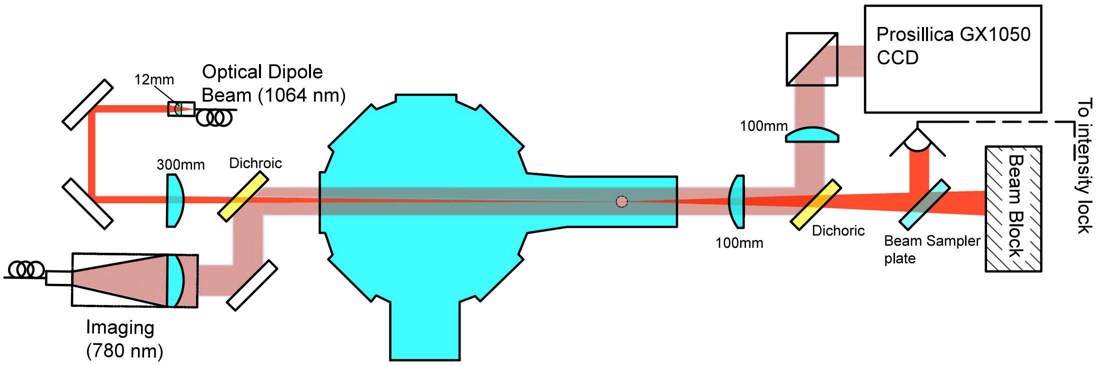

Figure 4.3.4: Laser schematic of the 1064 nm optical dipole trap producing a 70 μm waist beam focussed below the centre of the atomic cloud.

ing while the second has 2× magnification. Each beam is collimated to 25.4 mm diameter before being passed through the cell. The primary beam is able to image at any point in the sequence while the magnifying beam can only be used at the science cell location. Images are recorded by a Prosilica GX1050C CCD.

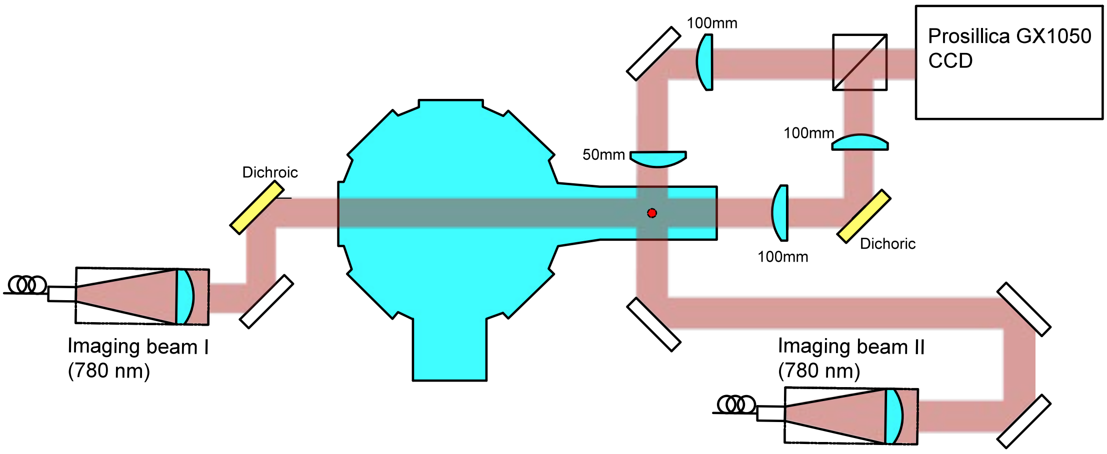

Figure 4.4.1: Schematic of the two horizontal imaging beams currently implemented on the system. Both are 4f relay systems, the first 1 : 1 and the second 2 : 1. Our primarily diagnostic beam is Imaging beam I, used for all quantitative analysis.

This CCD is a 1024×1024 array with each element measuring 5.5×5.5 μm. This is the colour version, consisting of a Bayer filter overlay on the CCD array, Fig. (4.4.2). This means that the spectral response of a block of 2×2 neighbouring pixels is different. In particular, a quarter of the pixels have a detection efficiency of less then 2 % at the imaging wavelength, 780 nm.

Fortunately, from a single image three colour layers are returned forming the RGB image. When a single layer is returned, pixels not overlaid with that spectral filter are interpolated and a more accurate image obtained. Given this, we elected to analyse images collected with the green array, as its sensors occupy 50 % of the array. This data is collected with 12 bit resolution, but noise means data is only meaningful to an optical density of ≈ 4.

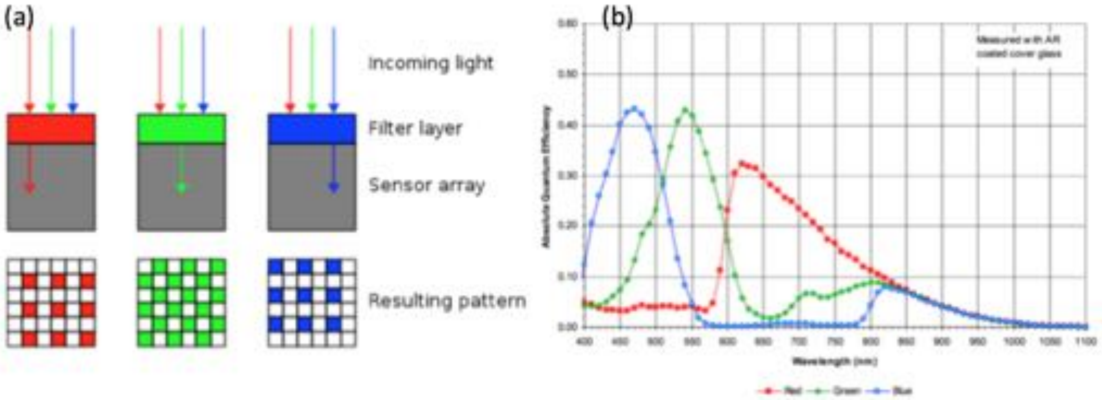

Figure 4.4.2: (a) Bayer filter layout on the Prosilica GX1050C CCD. Green pixels occupy 50 % of the real estate and therefore provide the best representation of an image taken with 780 nm light as determined by the efficiency of the sensor elements (b). Images from [192]

Described in section 2.8 are the requirements for extracting the optical density from absorption images and how this can be used to extract meaningful data. In particular, three images are required. These are an attenuated beam image, showing the shadow of the atom cloud, the imaging beam in absence of the atoms, and a background, or dark, image. Unfortunately, this process can introduce artefacts onto the optical density profile that reduce the accuracy of atom counts. In particular mechanical vibrations can cause fringing that degrade image quality. To minimise the effect of this, the time between the first two images must be as small as possible. Here we are able to produce crisp images of the cloud by simultaneously reading out an image taken by the Prosilica GX1050C while exposing it to the next image, with 100 μs between exposures.

To do this effectively, the precise, and synchronised timing of all imaging light elements is required, the timing diagram shown in Fig (4.4.3). Each image consists of a 50 ms exposure. However, the imaging beams are only present for 100 μs of this. The first image taken is that of the un-attenuated imaging beam. This is made possible by the fact that atoms, in the magnetic trap, reside in the $|1,-1\rangle$ sub level which is dark to the imaging beam, locked on the

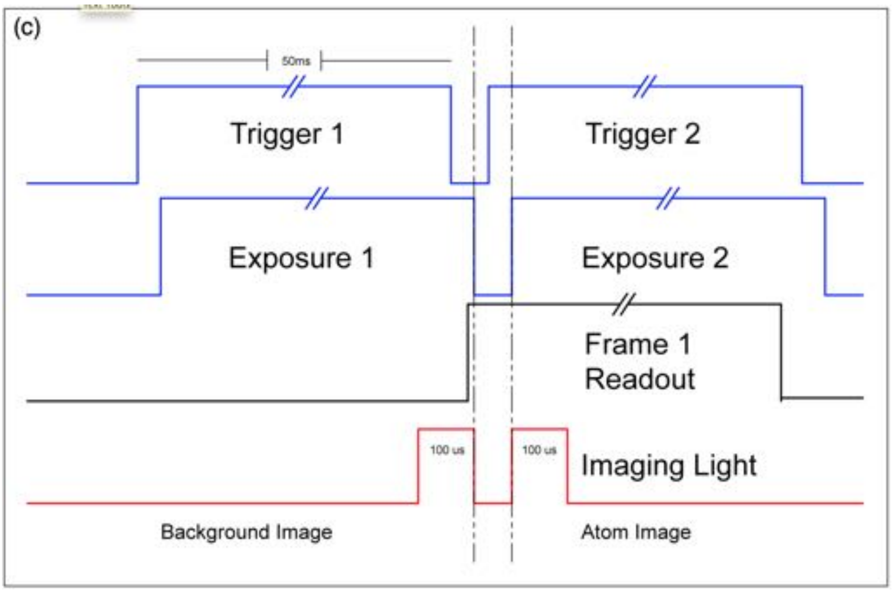

Figure 4.4.3: Timing diagram for back-to-back imaging with the GigE camera.

$|F=2\rangle \rightarrow |F'=3\rangle$ transition. As such an incident light level can be recorded. Once this beam is extinguished, the repump is switched on for 50 μs, during which the CCD is not recording. This pumps atoms in the $|F=2\rangle$ manifold, making them resonant with the imaging beam. Immediately afterwards this beam is extinguished and imaging light toggled for another 100 μs. This beam is now attenuated by the atomic cloud and can be used to calculate the optical density. A dark background image is taken with no light at the end of the second exposure for 50 ms. The timing of this is not crucial as the dark ground noise light level is almost negligible, under normal experimental circumstances. This is a key feature as to why this camera was chosen. Its high frame rates and ability for strobe imaging is ideal for the experiment.

Once images have been acquired they may be processed to extract meaningful data. We make use of MATLAB's image acquisition toolbox to communicate with the Prosilica camera and analyse the data. This is done at the end of each experimental run, and has the output shown in Fig (4.4.4). Pseudo code for the image processing code is,

1. First, the two-dimensional optical density profile is computed from the background, atom and dark images.
2. The centre of mass of the atomic cloud is found by creating a thresholded binary image and applying a median filter to remove noise. The first moment is found and used as the centre of the cloud. This step is only accurate for images with high to moderate SNR.

3. A thermal profile, $y = A\exp\left[\frac{(x-B)^2}{C^2}\right]$, is fit to an axial and radial slice which pass through the centre.
4. The atom number is calculated based on the optical density of the cloud and all the data is plotted, Fig (4.4.4).

4.5 High resolution imaging

State of the art in Bose-Einstein condensate experiments lays with the adaption and improvements in data acquisition capabilities, combined with the naturally large parameter space afforded by these systems. As discussed in Section 2.8 the adaptation of high-resolution absorption and fluorescence imaging systems have enabled in-situ knowledge on atom number distributions with high spatial resolution. In particular the parity measurements of the fluorescence scheme, Weitenberg et al [21], have shown single atom sensitivity with a resolution of $\simeq$ 700 nm when detecting rubidium atoms confined to a lattice. Similarly, the group of Markus Greiner constructed a solid immersion lens system (NA = 0.8) for imaging with a resolution down to $\simeq$ 600nm (FWHM) at 780 nm [19]

The difficulty with these designs is that they require specialised and custom optical equipment to be constructed, which is often costly or prohibitive in other areas of there experiment (limiting access or versatility). Here the vacuum apparatus design was influenced by the possibility of using commercially available microscope objectives. In particular, the all-glass BEC vacuum cell has a glass thickness equivalent to that of commercial liquid-crystal display technology. Being a lively industry, off-the-shelf microscope objectives with glass correction capabilities are readily available.

The science cell, a 12.5 × 46.25 × 22.5 mm Hellma analytics 101.150 QS cell, has an active imaging region of 10×45×20 mm with 1.25 mm thick quartz glass walls. This is well suited for use with our commercial microscope imaging objective, an Olympus LCPLN50xIR. This objective, Fig. (4.5.1), has a working distance of $\simeq$ 4.3 mm and a correction collar for aberrations, when imaging through a glass substrate. This can correct for 1.2 mm of glass, a bit less than the cell wall thickness, however the aberration should be negligible. A point to appreciate is that the atoms are transferred to the science cell its central axis and moved $\approx$ 100 μm down when transferred to the dipole trap. As a result, the ensemble resides $\approx$ 5 mm from the base of the science cell. This is outside the working distance of the LCPLN50xIR. In order to move the atoms into view,

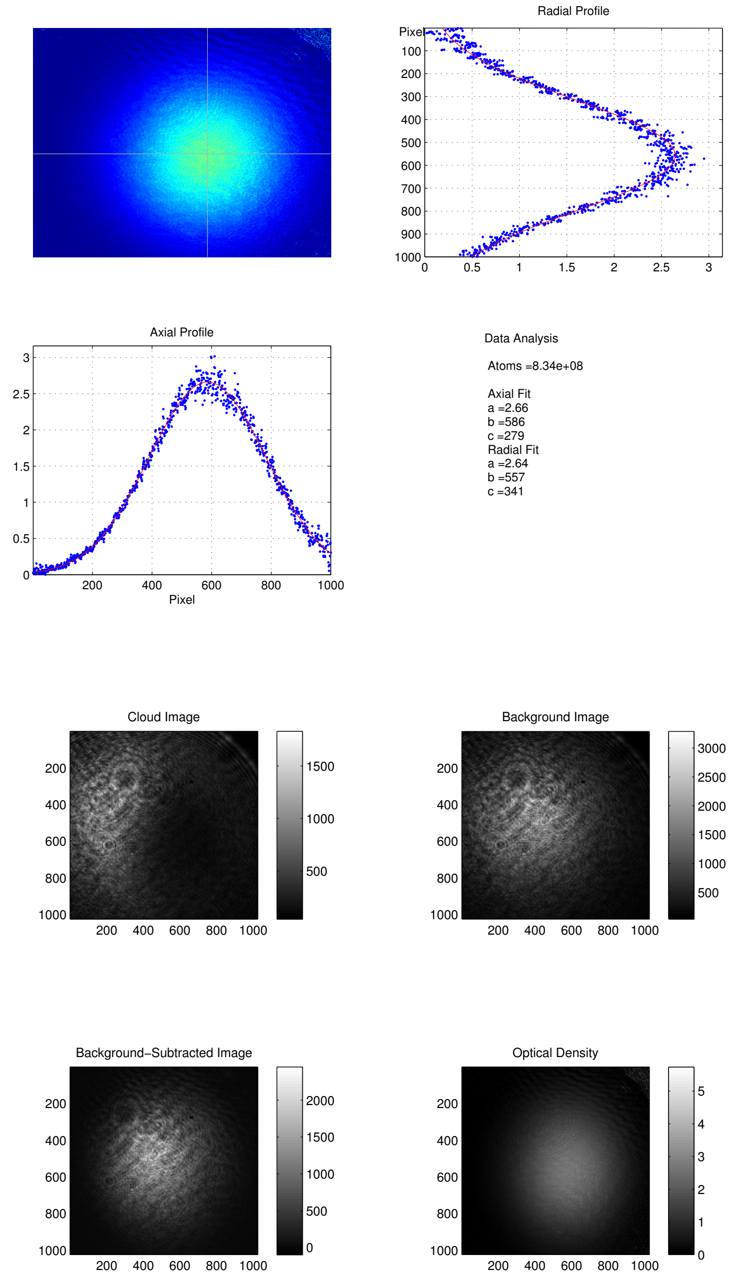

```
Data Analysis

Atoms =8.34e+08

Axial Fit
a =2.66
b =586
c =279
Radial Fit
a =2.64
b =557
c =341
```

Figure 4.4.4: Sample analysis window of the imaging software (left) showing the centre of the cloud, as calculated by the thresholded centroid method, and the fits through the slices. (right) The raw data and calculated optical density images.

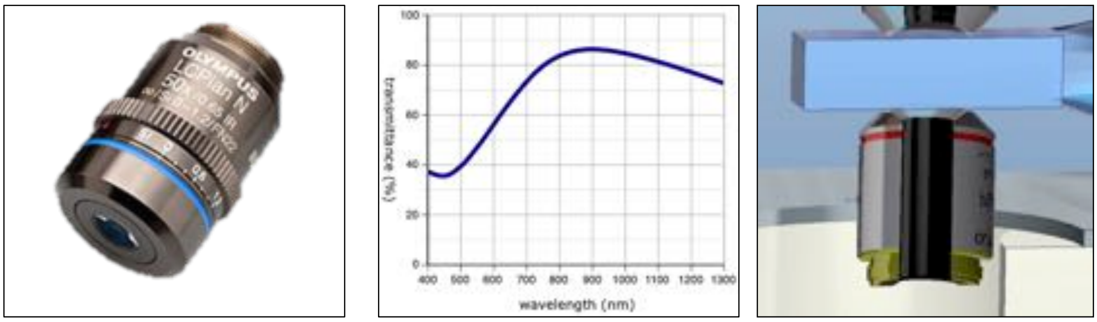

(a) (b) (c)

Figure 4.5.1: (a) A image of Olympus LCPLN50xIR microscope objective to be used for high resolution imaging on the apparatus, image from [195]. With an NA= 0.65 a resolution of 735 nm is possible with ^{87}Rb imaging light. The transmittance data through the objective is shown in (b). (c) Illustrates where the imaging objective is to be placed. As the glass is 1.25 mm thick and the working distance of the objective $\simeq$ 4.3 mm, the objective must be placed as close as possible to the cell as atoms will be trapped $\simeq$ 3 mm above the cell wall.

the quadrupole trapping field must be moved before loading into the hybrid trap, which can be achieved by reducing the current in the bottom coil. This vertical displacement of the atomic gas has yet to be completed as the focus of the work taken out in this thesis was to produce a condensate and not concerned with the high resolution imaging system. Additionally, a 0.4 NA, LCPLN-IR Series 20X is available. While having a reduced spatial resolution, it has a working distance of 8.3 mm and glass correction of 1.2 mm. This larger working distance means that it is not necessary to move the cloud for imaging.

The LCPLN-IR Series 20X objective has recently been placed onto the experiment, placed $\approx$ 3 mm from the bottom of the cell, Fig (4.5.2), by a custom designed hold. In order to precisely control and align the objectives this holder is mounted to a 3 axis close-loop NanoMax piezo stage. With the strain gauges displacement control down to 5 nm is available, with a travel of 20 μm.

The other elements of the high-resolution imaging system are the zoom lens and the CCD, arranged schematically in Fig (4.5.2) (Right). Once the imaging light is brought in from the top of the science cell, and the atoms interact, it is collected by the objective lens. This light is imaged with 20x magnification to the zoom lens which may be adjusted to whatever magnification is require before being image by the CCD. This CCD camera is a Princeton Instruments Pixis 1024 CCD. This device houses a 1024 × 1024 CCD with an optimised quantum efficiency in the UV and NIR range and zero etaloning. Each pixel is 13 × 13 μm. As a result the CCD

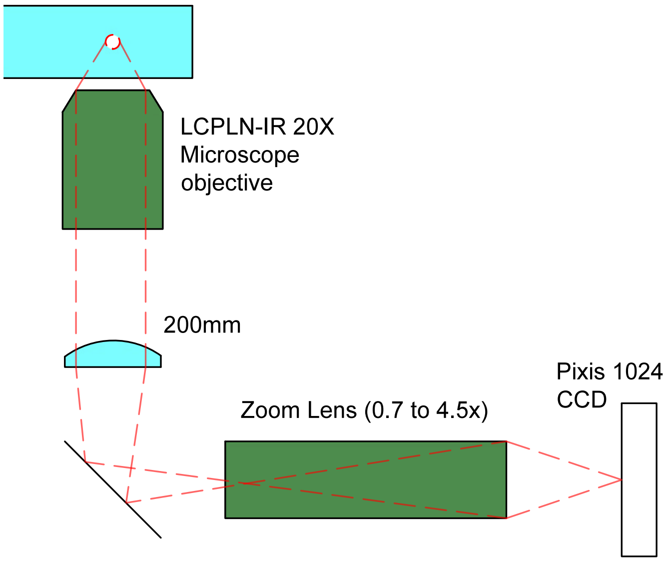

Figure 4.5.2: (Left) Image of the imaging objective mounted on the apparatus. The fine position of is controlled via a 3-axis piezo stage down to 5 nm. (Right) A schematic of the full high resolution imaging system.

images a ≈ 270 × 270 μm region at the trapping plane. While the microscope objective has not been implemented for imaging the atomic cloud, various side projects, mostly undertaken by Isaac Lenton, relating to the mechanical design and software control for doing so has been done in parallel to attaining a condensate. Upon completion of this thesis the objective had been mounted to the experiment and roughly aligned to the science cell. Preliminary testing of the imaging systems performance, and software interface, has it almost ready for use in imaging the cloud.

Initially this axis will perform absorption imaging in the same way as the horizontal imaging beams. However, in the future there is the intention to utilise dark-ground imaging techniques, new to Bose-Einstein condensates, to image condensates to very low atom numbers. Recently, numbers as low as 7 have been resolved [179], as well as in-situ imaging [180] using the dark-ground technique. By inserting a mask in front of a collecting lens only light scattering by atoms is collected and any background light does not reach the detector.

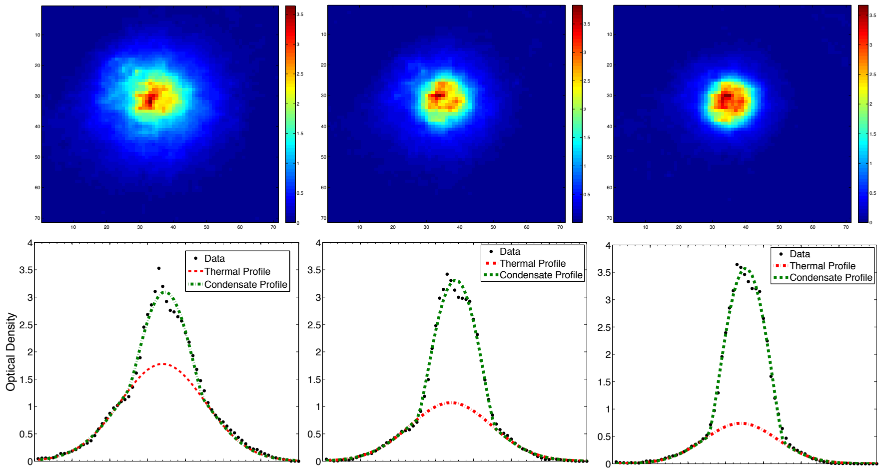

Figure 4.6.1: Evolution of the atomic profile as the ensemble moves across the BEC transition. It begins as a thermal cloud until the emergence of a peak arises and the condensate fraction increases as the optical power is reduced further.

4.6 Optical evaporation and condensation of ^{87}Rb

After atoms have been trapped in the 3D-MOT, put into a magnetic trap, transferred to the science cell, undergone microwave evaporation and loaded into the hybrid trap, they are ready to undergo a second evaporative cooling process to produce a BEC. However despite achieving an efficient and suitable loading of the hybrid trap, it was several weeks before a ^{87}Rb condensate was observed. Several systematic issues prevented it and had to be tracked down in order for proper operation of the system. Ground loops were present with the coil control circuits placing noise onto the magnetic quadrupole field and dipole beam stabilisation circuit. The NEG element of the ion pump on the 3D-MOT chamber side showed signs of saturation, and therefore decreased pumping speed. Further a persistent leak was present that may have interfered with the experiment. The main obstacle, however, was from back reflections of the 1064 nm dipole beam inducing presumed Raman transitions in the cloud that depleted the trap. By slightly angling this beam, such that the back reflection no longer overlapped the cloud of ^{87}Rb, the lifetime in the hybrid trap rose dramatically, from $\tau = 15$ s to $\simeq 40$ s, allowing time to perform optical evaporation ramps without competing against the atomic losses.

Optical evaporation of the cloud is performed by ramping down the power in the 1064 nm dipole beam exponentially via input to the intensity stabilisation circuit. In particular we reduce the 2.8 W of the dipole trap to some arbitrarily low value ($\simeq 600 \rightarrow 800$ mW) over 12 s until the characteristic bimodal distribution of a BEC is observed, Fig(4.6.1). By lowering the power further an almost pure condensate of $\approx 1.5 \times 10^5$ ^{87}Rb atoms is produced, with a lifetime of $\tau \simeq 5$ seconds, Fig (4.6.2).

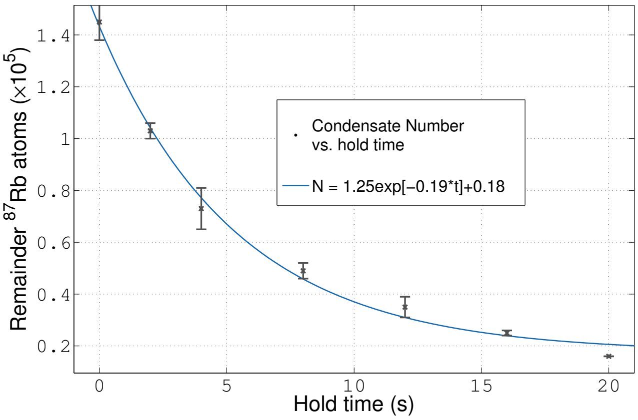

Figure 4.6.2: Experimental decay of atom number in the degenerate ^{87}Rb cloud. The lifetime of 5 seconds is sufficient but may indicate vacuum limited problems that restrict it from being up to several minutes long.

This represents the culmination of work up to the final month in the laboratory. In the short time remaining condensates were routinely, but not reliably, produced on a day-to-day basis. In particular it was found that BECs could be produced in the morning but would have poor reproducibility and reliability in the afternoon. This precluded extensive optimisation and investigations of the BEC but did aid in further improvements and decisions on the experiment. In particular it demonstrated the extent to which saturation of the NEG element, and subsequent vacuum limited losses, was detrimental and aided in discovering a small vacuum leak. Since my time in the laboratory, this information was used to make the decision to open the vacuum system to atmosphere and add a new ion pump to the 3D-MOT side and remove leaks.

4.7 Sequence Summary

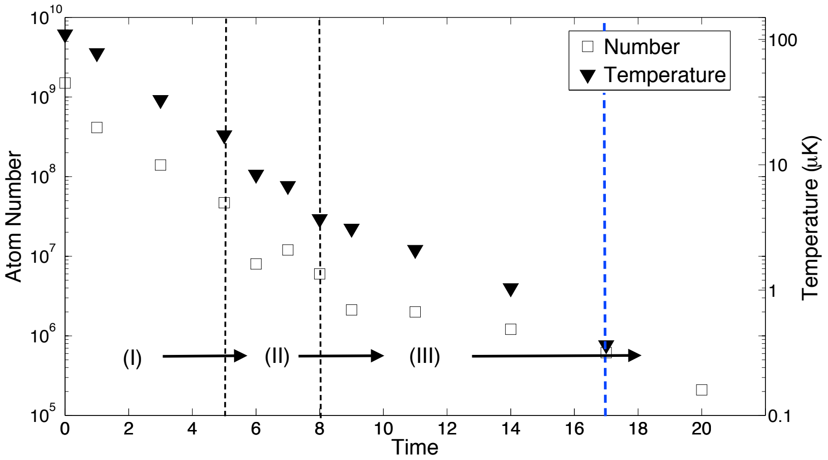

Figure 4.7.1: Production of a degenerate ^{87}Rb gas consisting of $N = 1.5 \times 10^5$ atoms from step (I) to (III). (I) Microwave evaporation of the compressed cloud in the quadrupole trap at the science cell (II) loading into the dipole trap and (III) optical evaporation in the dipole trap. Atom number N (open squares) and temperature T (solid triangles) versus BEC pathway time.

Fig (4.7.1) and Table (4.2) shows an overview of a typical experimental sequence for producing a condensed cloud of ^{87}Rb in the hybrid trap. The experimental sequence for producing ^{87}Rb condensates is as follow. First $2 \rightarrow 4 \times 10^9$ atoms are loaded into the 3D-MOT, fed by an atomic beam from the 2D-MOT. $50 \rightarrow 60$ % of these are loaded into a purely magnetic quadrupole trap with an axial gradient of $B'_z = 100$ G cm^{-1}. This ensemble is then transferred, from the 3D-MOT chamber, to the science cell by a magnetic hand-off procedure. Here, $\simeq 1 \times 10^9$ atoms, at 100 μK are evaporated, by microwaves, after the quadrupole field gradient is increased to $B'_z = 160$ G cm^{-1}. This is done until Majorana spin-flips become significant, typically leaving 50×10^6 atoms at 20 μK remaining. As the far red-detuned, and thus conservative, optical dipole trapping beam (1064 nm) is switched on, the gradient of the magnetic fields is lowered, just below that which supports atoms against gravity, allowing atoms to fall into the laser fields attractive potential. As a result $3 \rightarrow 10 \times 10^6$ atoms remain before a 12 s optical evaporation ramp produces a pure ^{87}Rb condensate of 1.5×10^5 atoms. A plot showing the atomic number and temperature during the entire BEC procedure is given in Fig (4.7.1).

#	Stage	Duration	N_{Rb}	T
1.	MOT	10 s	$3.0 \rightarrow 5.0 \times 10^9$	$\simeq 100\ \mu$K
2.	CMOT	50 ms	$\simeq 2.0 \rightarrow 3.0 \times 10^9$	-
3.	Depump	3 ms	$\simeq 2.0 \rightarrow 3.0 \times 10^9$	-
4.	Magnetic trap I	10 ms	1.0×10^9	100 μK
5.	Magnetic transfer	800 ms	1.0×10^9	100 μK
6.	Magnetic trap II	10 ms	1.0×10^9	150 μK
7.	Microwave Evaporation	5 s	5.0×10^7	20 μK
8.	Hybrid trap load	3 s	$\simeq 5.0 \times 10^6$	5 μK
9.	Optical evaporation	12 s	$\simeq 1.5 \times 10^5$	Condensate

Table 4.2: Summary of the main experimental steps in producing an ^{87}Rb condensate. This is shows the number of trapped atoms and the duration of each step.

Chapter 5

Outlook and Summary

The design, construction and testing of the apparatus, the supporting infrastructure and operation represents the main contributions of the author to the dual-species apparatus at UQ. This culminated with the observation, and preliminary characterisation of a ^{87}Rb condensate consisting of $\approx 1.5 \times 10^5$ atoms. However the scope of the experiment is to make use of the large optical, and close physical, access of the system for high resolution imaging in order to study non-equilibrium dynamics in a closed, interacting quantum system. Of particular interest, once a dual species condensate is available, is the study of universality of single-species domain formation following a system quench across the miscible to immiscible phase transition. Further, we wish to do so inside a flattened, homogenous box trap. In order to do so, the short-term goals of the experiment are:

1. Creation and optimisation of the ^{87}Rb and ^{41}K condensate.
2. Implementation of (dynamically) two-dimensional trapping infrastructure in order to have a spatially homogenous atomic mixture.
3. Implement the high resolution imaging optics in order to study domain formation when quenched across the miscible-immiscible phase transition.
4. The data should demonstrate some universality in its dynamics, well explained in [75].

Work towards these goals has been ongoing, in tandem, with the work presented in this thesis by the various members of the research group. Here a brief summary of their progress is presented.

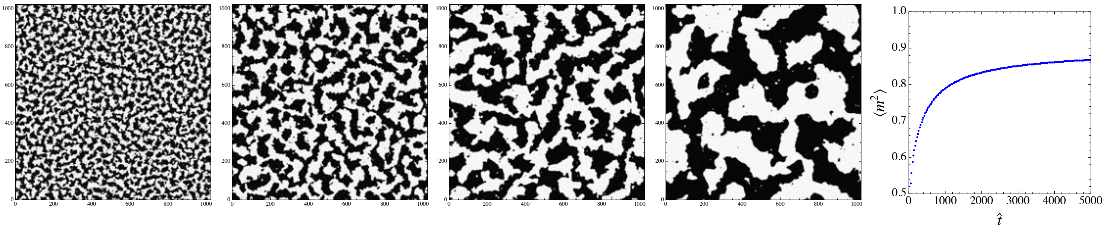

(a) $\hat{t} = 300$ (b) $\hat{t} = 1000$ (c) $\hat{t} = 2000$ (d) $\hat{t} = 5000$ (e)

Figure 5.0.1: Numerical simulation of the time evolution of a binary Bose condensate following a quench from the miscible to immiscible phase transition for various times $\hat{t}$, taken from [75]. Domains of positive (negative) magnetisation are shown in black (white). The sizes of these domains are anticipated to show self-similar coarsening evolution with a universal scaling law. (e) Shows how the average magnetisation (species domain) scales over time.

5.1 Towards a Flat Trap

As mentioned, we wish to study our system in a flattened pancake-esque trapping potential such that the motional dynamics in one direction are suppressed. In particular we wish to restrict the movement along the direction of gravity. Given highly anisotropic traps are regularly engineered to reach the quasi-2D and 1D regime, a flat trap is readily available to experiments. In general, this is achieved by increasing the trapping frequency along one direction until the condensate radius approaches the healing length associated with interatomic interactions. This may not always be sufficient, however, as atoms may literally squeeze into this third dimension if the density is too great [181]. In practice we only require the superfluid dynamics to be generally two-dimensional. In this regard we seek to produce a condensate which is fully 3D, but with tight confinement in one direction.

Experimentally we wish to suppress the axial direction, along gravity, by placing atoms in the nodal plane of a Hermite-Gaussian TEM$_{01}$ mode. To produce this light field, the output from a 532 nm Coherent Verdi laser will be passed through a phase plate. After focussing through a cylindrical lens the beam will emerge as an approximate TEM$_{01}$ mode that can suppress motion in the vertical direction. An optical schematic is presented in Fig (5.1.1).

An incident Gaussian beam, after passing through the phase plate and shaping optics, arrives at the image plane (the atom location) with an intensity pattern given by [182],

$$I(\mathbf{r}) = \frac{2P}{\pi w_x w_z} \mathrm{erf}^2\left(\frac{z}{\omega_z}\right) \exp\left[-\frac{2x^2}{w_x^2} - \frac{2z^2}{w_z^2}\right], \tag{5.1.1}$$

where P is the power in the beam, w_z and w_x are the beam waists in the axial (confining) and

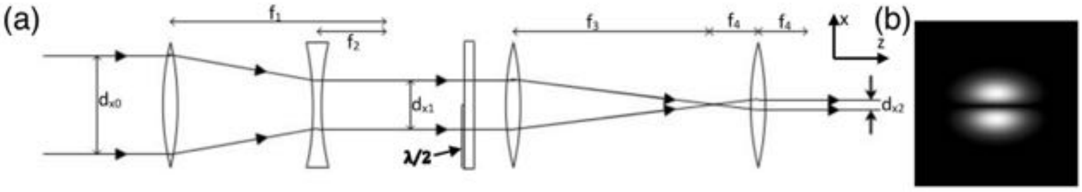

Figure 5.1.1: (a) Proposed schematic for producing the TEM$_{01}$ mode (b) in order to have a system with reduced dimensionality. The beam is shaped before being passed through a phase plate until it passes through a cylindrical lens to and collimated onto the cloud position.

transverse directions. Subsequently, the trapping frequency seen from atoms with mass m along the axial direction is then given by:

$$\omega_z = \sqrt{\frac{24Pc^2\Gamma}{\pi w_x w_z^3 \omega_0^3 m\Delta}}. \tag{5.1.2}$$

Here ω_0 is the frequency of the light, and Δ the detuning from the appropriate D$_2$ transition line. Several methods exist by which this trapping frequency can be increased, such as bringing the light close to resonance or increasing the power in the beam. The former is not feasible as having a near-resonant beam results in non-negligible scattering rates, which will deplete the number of trapped atoms. However, if the power is sufficiently high, then the trapping frequency is increased and the axial dynamics suppressed. Here we use a blue-detuned beam, where atoms will reside in the nodal plane. In this configuration, the confinement area is less affected by spurious intensity gradients or small length scale speckle on the intensity profile.

As the TEM$_{01}$ has a nodal plane, if atoms are loaded into the trap they are free to diffuse along the unconfined directions. As a result the ends of the nodal plane must be blocked such that atoms are trapped. This is to be done by projecting a pattern, along the axial (gravity's) direction from a spatial light modulator (SLM) to create a hard-walled potential. This is done through a SLM of the digital-micromirror device (DMD) variety.

5.2 Digital Micro-mirror Device

The digital micro-mirror device is an array of small and individually addressable micro-mirrors, capable of generating configurable binary potentials. These commercial products are often used in digital display devices such as projectors and holographic visualisation systems [183]. Recently, DMDs have emerged as a useful tool in academic and technical fields for aberration corrections [183, 184, 185] and optical tweezing. In ultra-cold atom experiments, given the high level of control, down to a single pixel elements, they may be used in conjunction with optical lattices to readily control atom distributions [21, 22]. The use of DMDs for generating the trapping potential itself has also begun to gain traction [186, 187]. We intend to use a DMD on our experiment in this way. In particular we intend to use the DMD as a binary amplitude SLM that will be projected, vertically, onto the atomic cloud to engineer arbitrary potentials while also confining the cloud to the nodal plane of the TEM01 sheet beam. The majority of this work has been carried out by the ever-enthusiastic Isaac Lenton.

5.2.1 Background Information

A DMD consist of two key elements, the micro-mirror array itself and the controller board, which interfaces, powers, and signals the pixel elements. On the DMD, several hundred thousand microscopic mirrors are arranged in a rectangular array. These mirrors are tiltable, to ±12 °, to an on or off state. The on state is a reflection in the intended propagation direction, which the off state is a reflection away. Tilt is provided by a yoke and hinge element that connects to a CMOS element that 'memorises' the mirror state, thereby latching it on or off as programmed, Fig. (5.2.1). The mirror array sits atop a random access memory cell array, which facilitates the communication between the controller board and mirror state. When correctly operated, the DMD may be used as a spatial light modulator, however several considerations are important in doing so.

The DMD may be used in two configurations. When placed at the Fourier plane in an imaging system, phase and amplitude control is afforded to the user. This is has shown to be a very powerful technique in creating a variety of patterned optical fields, with complex phase structures [188]. However such a method has low power efficiency in terms of power remaining at the imaging plane due to low diffraction efficiency. If phase control is sacrificed, an increase in efficiency is gained when the DMD is placed at an object plane. This provides binary amplitude modulation of an incident beam, with good transfer efficiency, when phase modulation is not required. This is the method that is to be employed on the experimental set up.

5.2.2 DMD Imaging Considerations

A key consideration in using DMDs as amplitude masks is that they are binary SLMs. This is a direct consequence of the micro-mirror operation, being either off or on. Given this devices

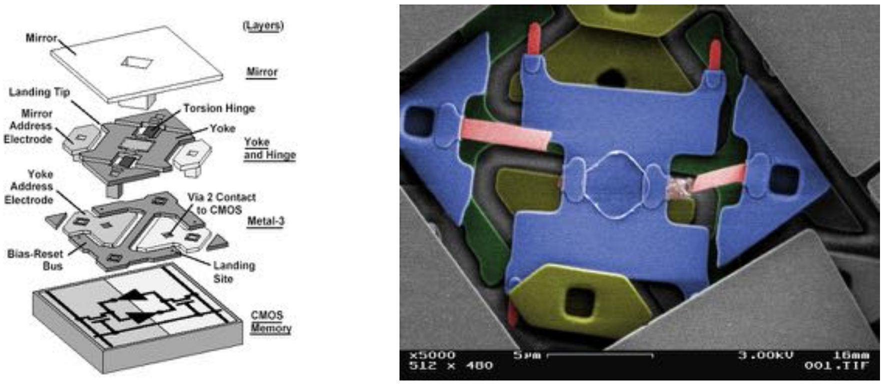

Figure 5.2.1: (Left) Schematic of a single mirror element of a DMD array. The mirror connects to the yoke and hinge which enables of tilt ±12° which constitutes the on or off state of each element, image from [193]. CMOS memory enables latching capability. (Right) Coloured electron microscope image of a small section of a DMD array, image from [194]. A mirror has been removed showing the yoke and hinge assembly below.

are popular elements for projective devices, they are able to cycle through patterns at a rate faster than perceptible by the human eye, which means mirror can be switch on or off at a rapid rate. This is the basis of grayscale imaging with binary amplitude SLMs. The DMD used here has a 22 kHz switching capability. When run with 3-bit grayscale depth capability the 'average' resolution, per 3-bit image, is 2.75 kHz. Given atoms are normally confined to potentials with trapping frequencies of this order, the atoms may not 'see' the discrete amplitude changes but rather experience the average of many frames. As such intricate knowledge of the data transfer process is important to determine the frame rate as the atoms will experience. Another consideration, is that, for trapping purposes it is important to consider how the amplitude mask will translate to the trapping plane of the atoms. The size of the DMD array, consisting of thousands of micro-mirrors, is a 10.8 μm square. The size of a BEC in a cross dipole trap, however, is typically on the order of a few μm. Therefore any trapping potential generated by the DMD must be minified at the trapping plane in order to be useful, just as a dipole beam is focussed for the dipole trap. This imaging system therefore projects the image formed by the DMD into the trapping plane of the atoms. If the resolution of this projecting system is higher than the mirror spacing, then the DMD is perfectly mapped to the trapping plane and the binary pattern is perfectly imaged. This means only binary patterns are available to the user. Thus any grayscale imaging would require the cycling of the DMD pattern, which may not be desirable. Another method for creating smooth varying intensity images is having a finite resolution system that cannot resolve single mirrors. As a result, any single resolution element of the imaged DMD would consist of several contributing elements defined by the point-spread function, Fig (5.2.2) (right). Thus the power incident on the image plane is averaged over several mirrors, making gradients in intensity possible. This is the method to be employed in our laboratory.

5.2.3 DMD and the Imaging System

Based on these considerations the most effective DMD was one which maximised frame rate and had high array resolution and decent diffraction efficiency. This search resulted in purchasing a Visitech Luxbeam 4600 DLP controller board with a WUXGA 2xLVDS DMD array, Fig (5.2.2) (left). This array consists of 1920×1200 pixels with maximum update frequency of 20.5 kHz. Each micro-mirror measures 10.8×10.8 μm with the on-board memory allowing storage of up to $\simeq 15000$ DMD patterns. This latter capability is useful when trying to utilise the maximum frame rate of the DMD device for slowly time-varying potentials.

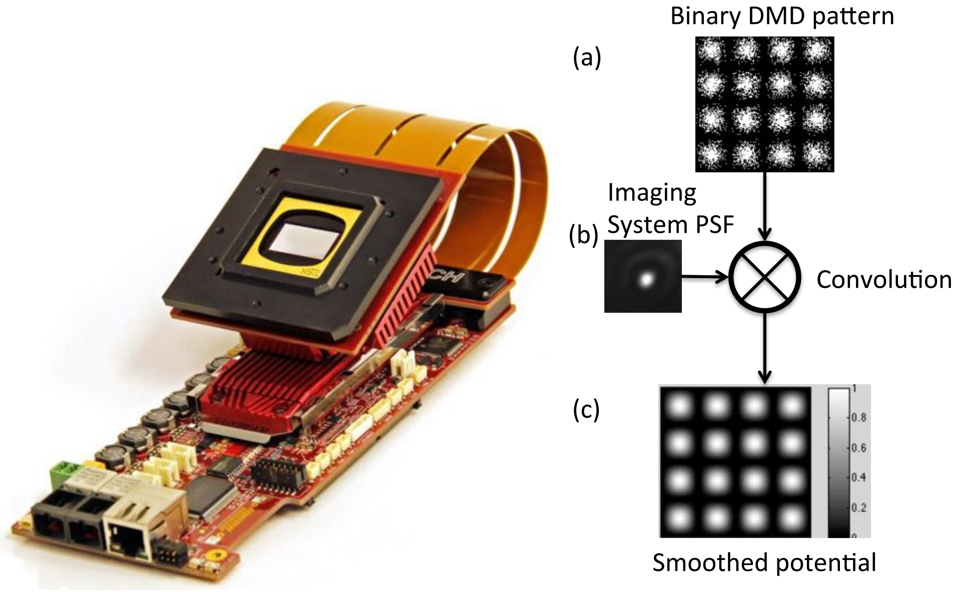

Figure 5.2.2: (Left) Visitech Luxbeam 4600 DLP controller and WUXGA DMD array, image from [196]. This DMD has 1920×1200 pixels for use on our system. The DMD is physically separable from the board however adequate heat sinking is important. (Right) Illustration of how a binary pattern from a DMD may be convolved with the finite point spread function to produce a smoothened potential.

The first use of the DMD will be to create a confining potential in combination with the sheet beam. This is to be done by using blue-detuned light, which caps the nodal plane of the sheet such that atoms reside in the intensity minima in the middle. Ideally we wish to create a homogenous trap but this is complicated by the harmonic intensity profile of the sheet-producing beam where intensity correction is not readily available. The DMD is used as a binary amplitude SLM with the beam project orthogonally to that of the sheet beam. In practice it is implemented to be imaged vertically through the aperture in the Macor coil hold above the science cell, Fig (5.2.3).

Collimated 532 nm light is projected on the DMD, which acts as an amplitude mask in the image plane. A 4f imaging system, consisting of a 500 mm lens and microscope objective, may then minify the pattern to the imaging plane. The microscope objective is a Nikon L Plan 20X/0.45 resulting in a total minification of $50X$, at the final imaging (or trapping) plane. Each resolution element consists of 6×6 micro-mirrors.

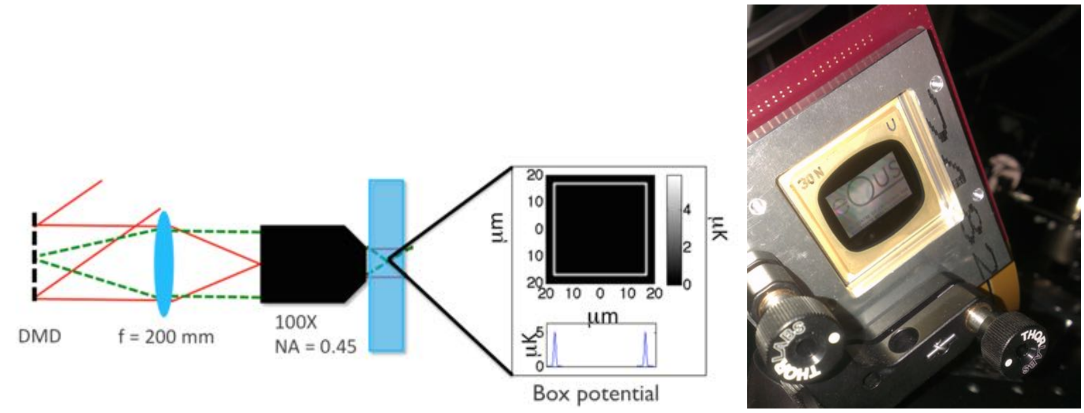

Figure 5.2.3: Left - Schematic of the DMD device projecting a box trap into the trapping plane to cap off the sheet beam and create a homogenous trap. The total magnification and finite resolution of the system means that smooth potentials may be generated as multiple mirrors contribute to a single resolution element in the trapping plane. Right - A photo of the DMD mounted with mirror displaying the EQUS logo.

Physically these elements have been implemented onto the system, an image of the DMD shown in Fig (5.2.3) (right). This required careful and precise alignment due to short working distances and depth of field of the microscope objectives. Shown in Fig (5.2.4) is experimental data that demonstrates the performance of the DMD and high-resolution imaging system. A square lattice, with 1.3 μm spacing between sites, has been imaged. The performance is promising and illustrates the ability to create potentials that have a varying intensity profile, not limited by the binary mode of operation. The ability to produce this spacing is also beneficial as neighbouring lattice sites are close enough spaced that significant tunnelling is expected for ^{87}Rb and ^{41}K. A test 'box' potential has also been created which may be used for studies on coarsening dynamics. A stirring beam, which may be moved at the DMD frequency, can be used to create a turbulent initial state as well. These are patterns are well resolvable by the vertical imaging system that shows a resolution of $\simeq$ 650 nm full-width half maximum at 532 nm.

The initial testing of DMD has shown great promise and is a testament to the work carried out by the occupants of the lab. In complicated patterns, optimal half-toning, the process by

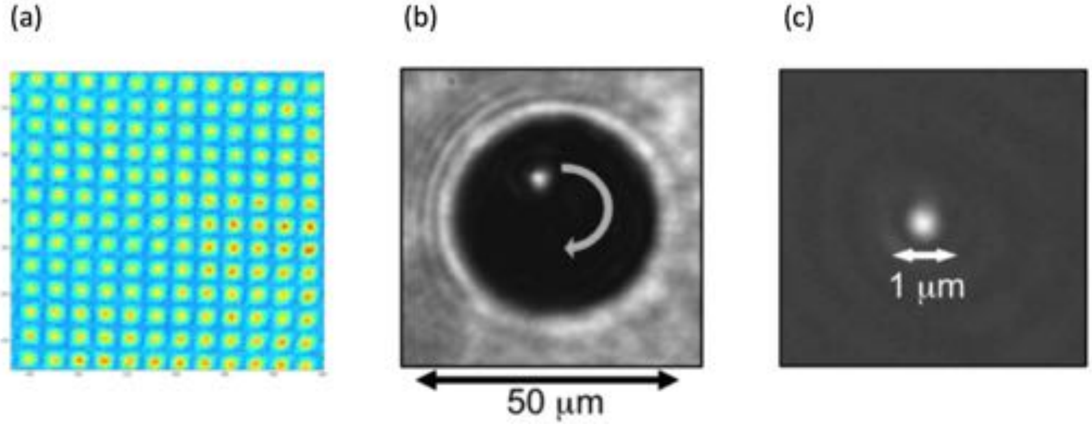

Figure 5.2.4: Images of patterns generated by the DMD array and imaging system. A square lattice with $\simeq 1.3$ μm lattice spacing (a), a circular box with stirring beam to study turbulent flow (b) and single 'on' mirror characterising the resolution of the system ($\simeq$ 650 nm at 532 nm)

which finite resolution is used to create the varying intensity patterns, is an iterative optimisation problem. This may be done in-situ by reimaging the trapping potential and feeding this back to an iterative optimisation algorithm that attempts to match the output image to the target function, aiming for a RMS less than 1%. This has involved the constant investigation and testing of a variety of algorithms including binarization and random dither methods [189].

5.3 Conclusion

It is hoped that this thesis provides the relevant and useful information regarding the design, construction, performance, status, and progress of the dual species ^{87}Rb and ^{41}K Bose-Einstein condensate apparatus. During design and construction, we endeavoured to build a versatile and robust experiment that offered a great range of flexibility for future opportunities, without compromising on performance. Aspects of the flexibility include close physical and high optical access about the science chamber and implementation of magnetic and optical trapping potentials. Additionally, the presence of potassium sources and capability of changing the wavelength of the potassium laser could enable switching to a Fermi-Bose or different Bose-Bose mixture if desired. It is also hoped that this thesis aids future students entering the laboratory to reduce the learning time required to use the apparatus.

Over the course of my postgraduate time within the laboratory the vacuum, laser and magnetic field systems were designed, erected and tested. These were then used to produce dual species 3D MOTs of ^{87}Rb and ^{41}K. The magnetic trapping and transfer chain, consisting of a novel coil and cooling design were similarly designed, constructed and tested. This was able to transfer $50 \rightarrow 60\%$ (1×10^9 atoms) of MOT-cooled rubidium atoms, with negligible atom losses or heating of the sample. These atoms were then subjected to microwave evaporation to create a much cooler, and dense, atomic cloud that was well matched to load into a 1064 nm dipole trap. Loading of the dipole trap, to form the hybrid trap, resulted in 5.0×10^7 atoms, which can be optically evaporated to produce a Bose-Einstein condensate. In the waning months of my laboratory time, a ^{87}Rb condensate of $\approx 1.5 \times 10^5$ atoms was observed, with much delight, representing the culmination of the work undertaken for this thesis.

A great deal of work lies ahead, before first experiments into non-equilibrium dynamics begin, but the performance shown by the DMD and the high-resolution imaging system demonstrate that the apparatus is more than capable. Several unknowns exist and need to be explored before this becomes reality, however. First ^{41}K must be incorporated and optimised alongside the established ^{87}Rb condensate. Alignment, loading and optimisation of atoms into a trap configured by the DMD also needs to be carried out. Lastly, depending on this transfer step additional evaporative cooling may be required in the box if loading the trap is not efficient. This previously unexplored territory has recently been studied [190, 191].

All in all, this experiment promises to add to the field of degenerate quantum gases as it combines the rich topology of condensate mixtures and the high resolution imaging capabilities of state of the art experiments with the flexibility of digital micro-mirror derived potentials.

Bibliography

[1] JF Allen and AD Misener. Flow of liquid helium II. *Nature*, 141(3558):75, 1938.

[2] JF Allen and H Jones. New phenomena connected with heat flow in helium II. *Nature*, 141(3562):243–244, 1938.

[3] R Balili, V Hartwell, D Snoke, L Pfeiffer, and K West. Bose-Einstein condensation of microcavity polaritons in a trap. *Science*, 316(5827):1007–1010, 2007.

[4] Mike H Anderson, Jason R Ensher, Michael R Matthews, Carl E Wieman, and Eric A Cornell. Observation of Bose-Einstein condensation in a dilute atomic vapor. *Science*, 269(5221):198–201, 1995.

[5] Kendall B Davis, M-O Mewes, MR van Andrews, NJ Van Druten, DS Durfee, DM Kurn, and Wolfgang Ketterle. Bose-Einstein condensation in a gas of sodium atoms. *Physical Review Letters*, 75(22):3969, 1995.

[6] Eric A Cornell and Carl E Wieman. Nobel lecture: Bose-Einstein condensation in a dilute gas, the first 70 years and some recent experiments. *Reviews of Modern Physics*, 74(3):875, 2002.

[7] Wolfgang Ketterle. Nobel lecture: When atoms behave as waves: Bose-Einstein condensation and the atom laser. *Reviews of Modern Physics*, 74(4):1131–1151, 2002.

[8] MR Andrews, CG Townsend, H-J Miesner, DS Durfee, DM Kurn, and W Ketterle. Observation of interference between two Bose condensates. *Science*, 275(5300):637–641, 1997.

[9] I Bloch, Th W Hänsch, and T Esslinger. Measurement of the spatial coherence of a trapped Bose gas at the phase transition. *Nature*, 403(6766):166–170, 2000.

[10] MR Matthews, BP Anderson, PC Haljan, DS Hall, CE Wieman, and EA Cornell. Vortices in a Bose-Einstein condensate. *Physical Review Letters*, 83(13):2498, 1999.

[11] T Schumm, S Hofferberth, L Mauritz Andersson, S Wildermuth, S Groth, I Bar-Joseph, J Schmiedmayer, and P Krüger. Matter-wave interferometry in a double well on an atom chip. *Nature Physics*, 1(1):57–62, 2005.

[12] MJ Snadden, JM McGuirk, P Bouyer, KG Haritos, and MA Kasevich. Measurement of the earth's gravity gradient with an atom interferometer-based gravity gradiometer. *Physical Review Letters*, 81(5):971, 1998.

[13] Achim Peters, Keng Yeow Chung, and Steven Chu. High-precision gravity measurements using atom interferometry. *Metrologia*, 38(1):25, 2001.

[14] R Wynands and S Weyers. Atomic fountain clocks. *Metrologia*, 42(3):S64, 2005.

[15] Wolfgang Müssel, H Strobel, D Linnemann, DB Hume, and MK Oberthaler. Scalable spin squeezing for quantum-enhanced magnetometry with Bose-Einstein condensates. *Physical Review Letters*, 113(10):103004, 2014.

[16] Simon A Haine, Stuart S Szigeti, Matthias D Lang, and Carlton M Caves. Waste not, want not: Heisenberg-limited metrology with information recycling. *arXiv:1411.5111*, 2014.

[17] V. Ahufinger M. Lewenstein, A. Sanpera. *Ultracold Atoms in Optical Lattices: Simulating quantum many-body systems.* Oxford University Press, 2012.

[18] Peter Würtz, Tim Langen, Tatjana Gericke, Andreas Koglbauer, and Herwig Ott. Experimental demonstration of single-site addressability in a two-dimensional optical lattice. *Physical Review Letters*, 103(8):080404, 2009.

[19] Waseem S Bakr, Jonathon I Gillen, Amy Peng, Simon Fölling, and Markus Greiner. A quantum gas microscope for detecting single atoms in a hubbard-regime optical lattice. *Nature*, 462(7269):74–77, 2009.

[20] Wolfgang Muessel, Helmut Strobel, Maxime Joos, Eike Nicklas, Ion Stroescu, Jiří Tomkovič, David B Hume, and Markus K Oberthaler. Optimized absorption imaging of mesoscopic atomic clouds. *Applied Physics B*, 113(1):69–73, 2013.

[21] Christof Weitenberg, Manuel Endres, Jacob F Sherson, Marc Cheneau, Peter Schauß, Takeshi Fukuhara, Immanuel Bloch, and Stefan Kuhr. Single-spin addressing in an atomic mott insulator. *Nature*, 471(7338):319–324, 2011.

[22] Takeshi Fukuhara, Adrian Kantian, Manuel Endres, Marc Cheneau, Peter Schauß, Sebastian Hild, David Bellem, Ulrich Schollwöck, Thierry Giamarchi, Christian Gross, et al. Quantum dynamics of a single, mobile spin impurity. *arXiv preprint arXiv:1209.6468*, 2012.

[23] Takeshi Fukuhara, Peter Schauß, Manuel Endres, Sebastian Hild, Marc Cheneau, Immanuel Bloch, and Christian Gross. Microscopic observation of magnon bound states and their dynamics. *Nature*, 502(7469):76–79, 2013.

[24] Hans Bethe. Zur theorie der metalle. *Zeitschrift für Physik*, 71(3-4):205–226, 1931.

[25] Jonathan Simon, Waseem S Bakr, Ruichao Ma, M Eric Tai, Philipp M Preiss, and Markus Greiner. Quantum simulation of antiferromagnetic spin chains in an optical lattice. *Nature*, 472(7343):307–312, 2011.

[26] M Endres, M Cheneau, T Fukuhara, C Weitenberg, P Schauß, C Gross, L Mazza, MC Banuls, L Pollet, Immanuel Bloch, et al. Observation of correlated particle-hole pairs and string order in low-dimensional mott insulators. *Science*, 334(6053):200–203, 2011.

[27] Anders S Sørensen, Eugene Demler, and Mikhail D Lukin. Fractional quantum hall states of atoms in optical lattices. *Physical Review Letters*, 94(8):086803, 2005.

[28] Jean Dalibard, Fabrice Gerbier, Gediminas Juzeliūnas, and Patrik Öhberg. Colloquium: Artificial gauge potentials for neutral atoms. *Reviews of Modern Physics*, 83(4):1523, 2011.

[29] BT Seaman, M Krämer, DZ Anderson, and MJ Holland. Atomtronics: Ultracold-atom analogs of electronic devices. *Physical Review A*, 75(2):023615, 2007.

[30] Miroslav Gajdacz, Tomáš Opatrnỳ, and Kunal K Das. An atomtronics transistor for quantum gates. *arXiv:1207.3108*, 2012.

[31] Seth C Caliga, Cameron JE Straatsma, Alex A Zozulya, and Dana Z Anderson. A matter-wave transistor oscillator. *arXiv:1208.3109*, 2012.

[32] MA Cazalilla. Bosonizing one-dimensional cold atomic gases. *Journal of Physics B: Atomic, Molecular and Optical Physics*, 37(7):S1, 2004.

[33] Toshiya Kinoshita, Trevor Wenger, and David S Weiss. A quantum newton's cradle. *Nature*, 440(7086):900–903, 2006.

[34] Corinna Kollath, Andreas M Läuchli, and Ehud Altman. Quench dynamics and nonequilibrium phase diagram of the Bose-Hubbard model. *Physical Review Letters*, 98(18):180601, 2007.

[35] Immanuel Bloch, Jean Dalibard, and Sylvain Nascimbène. Quantum simulations with ultracold quantum gases. *Nature Physics*, 8(4):267–276, 2012.

[36] Giacomo Roati, Chiara D'Errico, Leonardo Fallani, Marco Fattori, Chiara Fort, Matteo Zaccanti, Giovanni Modugno, Michele Modugno, and Massimo Inguscio. Anderson localization of a non-interacting Bose–Einstein condensate. *Nature*, 453(7197):895–898, 2008.

[37] Martin Stoll and Thorsten Köhler. Production of three-body efimov molecules in an optical lattice. *Physical Review A*, 72(2):022714, 2005.

[38] Anatoli Polkovnikov, Krishnendu Sengupta, Alessandro Silva, and Mukund Vengalattore. Colloquium: Nonequilibrium dynamics of closed interacting quantum systems. *Reviews of Modern Physics*, 83(3):863, 2011.

[39] Lev Kofman, Andrei Linde, and Alexei A Starobinsky. Reheating after inflation. *Physical Review Letters*, 73(24):3195, 1994.

[40] Dmitry Podolsky, Gary N Felder, Lev Kofman, and Marco Peloso. Equation of state and beginning of thermalization after preheating. *Physical Review D*, 73(2):023501, 2006.

[41] Ryan Barnett, Anatoli Polkovnikov, and Mukund Vengalattore. Prethermalization in quenched spinor condensates. *Physical Review A*, 84(2):023606, 2011.

[42] Harold J Metcalf and Peter Van der Straten. *Laser cooling and trapping*. Springer, 1999.

[43] Christopher Pethick and Henrik Smith. *Bose-Einstein condensation in dilute gases*. Cambridge University Press, 2002.

[44] TP Meyrath, F Schreck, JL Hanssen, C-S Chuu, and MG Raizen. Bose-Einstein condensate in a box. *Physical Review A*, 71(4):041604, 2005.

[45] Igor Gotlibovych, Tobias F Schmidutz, Alexander L Gaunt, Nir Navon, Robert P Smith, and Zoran Hadzibabic.Dirac Observing properties of an interacting homogeneous Bose-Einstein condensate: Heisenberg-limited momentum spread, interaction energy, and free-expansion dynamics. *Physical Review A*, 89(6):061604, 2014.

[46] A Turpin, J Polo, Yu V Loiko, J Küber, F Schmaltz, TK Kalkandjiev, V Ahufinger, G Birkl, and J Mompart. Blue-detuned optical ring trap for Bose-Einstein condensates based on conical refraction. *arXiv:1411.1587*, 2014.

[47] Bogdan Opanchuk, Rodney Polkinghorne, Oleksandr Fialko, Joachim Brand, and Peter D Drummond. Quantum simulations of the early universe. *Annalen der Physik*, 525(10-11):866–876, 2013.

[48] Ron Folman, Peter Krüger, Donatella Cassettari, Björn Hessmo, Thomas Maier, and Jörg Schmiedmayer. Controlling cold atoms using nanofabricated surfaces: atom chips. *Physical Review Letters*, 84(20):4749, 2000.

[49] Immanuel Bloch. Ultracold quantum gases in optical lattices. *Nature Physics*, 1(1):23–30, 2005.

[50] C Becker, P Soltan-Panahi, J Kronjäger, S Dörscher, K Bongs, and K Sengstock. Ultracold quantum gases in triangular optical lattices. *New Journal of Physics*, 12(6):065025, 2010.

[51] Jennifer Sebby-Strabley, Marco Anderlini, PS Jessen, and JV Porto. Lattice of double wells for manipulating pairs of cold atoms. *Physical Review A*, 73(3):033605, 2006.

[52] Leticia Tarruell, Daniel Greif, Thomas Uehlinger, Gregor Jotzu, and Tilman Esslinger. Creating, moving and merging Dirac points with a Fermi gas in a tunable honeycomb lattice. *Nature*, 483(7389):302–305, 2012.

[53] Gyu-Boong Jo, Jennie Guzman, Claire K Thomas, Pavan Hosur, Ashvin Vishwanath, and Dan M Stamper-Kurn. Ultracold atoms in a tunable optical kagome lattice. *Physical Review Letters*, 108(4):045305, 2012.

[54] Alexander L Gaunt and Zoran Hadzibabic. Robust digital holography for ultracold atom trapping. *Scientific Reports*, 2, 2012.

[55] Florence Nogrette, Henning Labuhn, Sylvain Ravets, Daniel Barredo, Lucas Béguin, Aline Vernier, Thierry Lahaye, and Antoine Browaeys. Single-atom trapping in holographic 2d arrays of microtraps with arbitrary geometries. *Physical Review X*, 4(2):021034, 2014.

[56] Tim Langen, Remi Geiger, and Jörg Schmiedmayer. Ultracold atoms out of equilibrium. *arXiv:1408.6377*, 2014.

[57] Markus Greiner, Olaf Mandel, Tilman Esslinger, Theodor W Hänsch, and Immanuel Bloch. Quantum phase transition from a superfluid to a mott insulator in a gas of ultracold atoms. *Nature*, 415(6867):39–44, 2002.

[58] Chad N Weiler, Tyler W Neely, David R Scherer, Ashton S Bradley, Matthew J Davis, and Brian P Anderson. Spontaneous vortices in the formation of Bose–Einstein condensates. *Nature*, 455(7215):948–951, 2008.

[59] Giacomo Lamporesi, Simone Donadello, Simone Serafini, Franco Dalfovo, and Gabriele Ferrari. Spontaneous creation of Kibble-Zurek solitons in a Bose-Einstein condensate. *Nature Physics*, 9(10):656–660, 2013.

[60] Sebastian Hild, Takeshi Fukuhara, Peter Schauß, Johannes Zeiher, Michael Knap, Eugene Demler, Immanuel Bloch, and Christian Gross. Far-from-equilibrium spin transport in Heisenberg quantum magnets. *Physical Review Letters*, 113(14):147205, 2014.

[61] Marc Cheneau, Peter Barmettler, Dario Poletti, Manuel Endres, Peter Schauß, Takeshi Fukuhara, Christian Gross, Immanuel Bloch, Corinna Kollath, and Stefan Kuhr. Light-cone-like spreading of correlations in a quantum many-body system. *Nature*, 481(7382):484–487, 2012.

[62] S Braun, M Friesdorf, SS Hodgman, M Schreiber, JP Ronzheimer, A Riera, M del Rey, I Bloch, J Eisert, and U Schneider. Emergence of coherence and the dynamics of quantum phase transitions. *arXiv:1403.7199*, 2014.

[63] Cheng Chin, Rudolf Grimm, Paul Julienne, and Eite Tiesinga. Feshbach resonances in ultracold gases. *Reviews of Modern Physics*, 82(2):1225, 2010.

[64] Florian Meinert, Manfred J Mark, Emil Kirilov, Katharina Lauber, Philipp Weinmann, Andrew J Daley, and H-C Nägerl. Quantum quench in an atomic one-dimensional ising chain. *Physical Review Letters*, 111(5):053003, 2013.

[65] Alexander L Gaunt, Richard J Fletcher, Robert P Smith, and Zoran Hadzibabic. A superheated Bose-condensed gas. *Nature Physics*, 9(5):271–274, 2013.

[66] Paul Anthony Altin. *The role of interactions in atom interferometry with Bose-condensed atoms.* PhD thesis, Australian National University, Canberra, 2012.

[67] Fei Zhan, Jacopo Sabbatini, Matthew J. Davis, and Ian P. McCulloch. Miscible-immiscible quantum phase transition in coupled two-component Bose-Einstein condensates in one-dimensional optical lattices. *Phys. Rev. A*, 90:023630, Aug 2014.

[68] G Modugno, M Modugno, F Riboli, G Roati, and M Inguscio. Two atomic species superfluid. *Physical Review Letters*, 89(19):190404, 2002.

[69] Jacopo Catani. A new apparatus for ultracold K-Rb Bose-Bose atomic mixtures, 2006.

[70] Takeshi Fukuhara, Seiji Sugawa, Yosuke Takasu, and Yoshiro Takahashi. All-optical formation of quantum degenerate mixtures. *Physical Review A*, 79(2):021601, 2009.

[71] CCN Kuhn, GD McDonald, KS Hardman, S Bennetts, PJ Everitt, PA Altin, JE Debs, JD Close, and NP Robins. A Bose-condensed, simultaneous dual-species mach–zehnder atom interferometer. *New Journal of Physics*, 16(7):073035, 2014.

[72] Yijun Tang, Nathaniel Q Burdick, Kristian Baumann, and Benjamin L Lev. Bose-Einstein condensation of ^{162}Dy and ^{160}Dy. *arXiv:1411.3069*, 2014.

[73] P Ao and ST Chui. Two stages in the evolution of binary alkali Bose-Einstein condensate mixtures towards phase segregation. *Journal of Physics B: Atomic, Molecular and Optical Physics*, 33(3):535, 2000.

[74] Thomas WB Kibble. Topology of cosmic domains and strings. *Journal of Physics A: Mathematical and General*, 9(8):1387, 1976.

[75] Johannes Hofmann, Stefan S Natu, and S Das Sarma. Coarsening dynamics of binary Bose condensates. *arXiv preprint arXiv:1403.1284*, 2014.

[76] Markus Karl, Boris Nowak, and Thomas Gasenzer. Universal scaling at nonthermal fixed points of a two-component Bose gas. *Physical Review A*, 88(6):063615, 2013.

[77] RS Williamson and T Walker. Magneto-optical trapping and ultracold collisions of potassium atoms. *JOSA B*, 12(8):1393–1397, 1995.

[78] MS Santos, A Antunes, P Nussenzveig, J Flemming, SC Zilio, and VS Bagnato. Intensity dependence of the collisional loss rate for potassium-39 atoms in a vapor cell mot. *Laser Physics*, 8:880–884, 1998.

[79] L De Sarlo, P Maioli, G Barontini, J Catani, F Minardi, and M Inguscio. Collisional properties of sympathetically cooled ^{39}K. *Physical Review A*, 75(2):022715, 2007.

[80] Naaman Tammuz. Thermodynamics of ultracold ^{39}K atomic Bose gases with tuneable interactions, 2011.

[81] S Chu, C Cohen-Tannoudji, and WD Phillips. Nobel lectures in physics 1997. *Rev. Mod. Phys*, 70(3):685–741, 1998.

[82] Claude Cohen-Tannoudji. Manipulating atoms with photons. *Physica Scripta*, 1998(T76):33, 1998.

[83] Steven Chu. The manipulation of neutral particles. *Reviews of Modern Physics*, 70(3):685–706, 1998.

[84] J. Kepler. *De Cometis libelli tres... Autore Iohanne Keplero... (Carmen J. Tanckii)*. Typis Andreae Apergeri, 1619.

[85] A Bartoli. Sopra i movimenti prodotti dalla luce e dal calore. *Le Monnier, Firenze*, 1876.

[86] Adolfo Bartoli. Il calorico raggiante e il secondo principio di termodinamica. *Il Nuovo Cimento Series 3*, 15(1):193–202, 1884.

[87] P Lebedev. The experimental study of the pressure of the light. *Ann. Phys*, 6:433, 1901.

[88] E. Nichols and G. Hull. A preliminary communication on the pressure of heat and light radiation. *Phys. Rev. (Series I)*, 13:307–320, Nov 1901.

[89] EF Nichols and GF Hull. The pressure due to radiation.(second paper.). *Physical Review (Series I)*, 17(1):26, 1903.

[90] Albert Einstein. On the development of our views concerning the nature and constitution of radiation. *Phys. Z*, 10:817, 1909.

[91] Albert Einstein et al. On the electrodynamics of moving bodies. *Annalen der Physik*, 17(891):50, 1905.

[92] Louis de Broglie. Xxxv. a tentative theory of light quanta. *Philosophical Magazine Series 6*, 47(278):446–458, 1924.

[93] Theodor W Hänsch and Arthur L Schawlow. Cooling of gases by laser radiation. *Optics Communications*, 13(1):68–69, 1975.

[94] H Dehmelt. Proposed 1o nu greater than nu laser fluorescence spectroscopy on t1+ mono-ion oscillator ii. In *Bulletin of the American Physical Society*, volume 20, pages 60–60. Amer. Inst. Physics Circulation Fulfillment 11797-2999, 1975.

[95] William D Phillips and Harold Metcalf. Laser deceleration of an atomic beam. *Physical Review Letters*, 48(9):596, 1982.

[96] CJ Foot. Laser cooling and trapping of atoms. *Contemporary Physics*, 32(6):369–381, 1991.

[97] Steven Chu, JE Bjorkholm, A Ashkin, and Alex Cable. Experimental observation of optically trapped atoms. *Physical Review Letters*, 57(3):314, 1986.

[98] JP Gordon and A Ashkin. Motion of atoms in a radiation trap. *Physical Review A*, 21(5):1606, 1980.

[99] Arthur Ashkin and James P Gordon. Stability of radiation-pressure particle traps: an optical Earnshaw theorem. *Optics Letters*, 8(10):511–513, 1983.

[100] William T Scott. Who was Earnshaw? *American Journal of Physics*, 27(6):418–419, 1959.

[101] Paul D Lett, Richard N Watts, Christoph I Westbrook, William D Phillips, Phillip L Gould, and Harold J Metcalf. Observation of atoms laser cooled below the Doppler limit. *Physical Review Letters*, 61(2):169, 1988.

[102] Jean Dalibard and Claude Cohen-Tannoudji. Laser cooling below the Doppler limit by polarization gradients: simple theoretical models. *JOSA B*, 6(11):2023–2045, 1989.

[103] P Jeffery Ungar, David S Weiss, Erling Riis, and Steven Chu. Optical molasses and multilevel atoms: theory. *JOSA B*, 6(11):2058–2071, 1989.

[104] EL Raab, M Prentiss, Alex Cable, Steven Chu, and D E Pritchard. Trapping of neutral sodium atoms with radiation pressure. *Physical Review Letters*, 59(23):2631, 1987.

[105] Paul JJ Tol, Norbert Herschbach, Eric A Hessels, Wim Hogervorst, and Wim Vassen. Large numbers of cold metastable helium atoms in a magneto-optical trap. *Physical Review A*, 60(2):R761, 1999.

[106] Mike H Anderson, Jason R Ensher, Michael R Matthews, Carl E Wieman, and Eric A Cornell. Observation of Bose-Einstein condensation in a dilute atomic vapor. *science*, 269(5221):198–201, 1995.

[107] J Schoser, A Batär, R Löw, V Schweikhard, A Grabowski, Yu B Ovchinnikov, and T Pfau. Intense source of cold rb atoms from a pure two-dimensional magneto-optical trap. *Physical Review A*, 66(2):023410, 2002.

[108] Daniel A Steck. Rubidium 87 d line data, 2001. URL http://steck.us/alkalidata/.

[109] R Williamson. Magneto-optical trapping of potassium isotopes, Diss. University of Wisconsin1997.

[110] Arturo Bambini and Alessandro Agresti. Radiative cooling force in atoms with multiplet structure. *Physical Review A*, 56(4):3040, 1997.

[111] Xinye Xu, Thomas H Loftus, Josh W Dunn, Chris H Greene, John L Hall, Alan Gallagher, and Jun Ye. Single-stage sub-Doppler cooling of alkaline earth atoms. *Physical Review Letters*, 90(19):193002, 2003.

[112] Xinye Xu, Thomas H Loftus, John L Hall, Alan Gallagher, and Jun Ye. Cooling and trapping of atomic strontium. *JOSA B*, 20(5):968–976, 2003.

[113] Vandna Gokhroo, G Rajalakshmi, R Kollengode Easwaran, and CS Unnikrishnan. Sub-Doppler deep-cooled bosonic and fermionic isotopes of potassium in a compact 2D^{+}-3D mot set-up. *Journal of Physics B: Atomic, Molecular and Optical Physics*, 44(11):115307, 2011.

[114] M Landini, S Roy, L Carcagní, D Trypogeorgos, M Fattori, M Inguscio, and G Modugno. Sub-Doppler laser cooling of potassium atoms. *Physical Review A*, 84(4):043432, 2011.

[115] Gregory Breit and II Rabi. Measurement of nuclear spin. *Physical Review*, 38(11):2082, 1931.

[116] Thomas Andrew Bell. Design, construction and characterisation of a versatile high atom number BEC apparatus, *Honours thesis, University of Queensland* 2014.

[117] Wolfgang Petrich, Michael H Anderson, Jason R Ensher, and Eric A Cornell. Stable, tightly confining magnetic trap for evaporative cooling of neutral atoms. *Physical Review Letters*, 74(17):3352, 1995.

[118] Wolfgang Ketterle and NJ Van Druten. Evaporative cooling of trapped atoms. *Advances in atomic, molecular, and optical physics*, 37:181–236, 1996.

[119] Charles S Adams, Heun Jin Lee, Nir Davidson, Mark Kasevich, and Steven Chu. Evaporative cooling in a crossed dipole trap. *Physical Review Letters*, 74(18):3577, 1995.

[120] Ettore Majorana. Atomi orientati in campo magnetico variabile. *Il Nuovo Cimento (1924-1942)*, 9(2):43–50, 1932.

[121] TH Bergeman, Patrick McNicholl, Jan Kycia, Harold Metcalf, and NL Balazs. Quantized motion of atoms in a quadrupole magnetostatic trap. *JOSA B*, 6(11):2249–2256, 1989.

[122] U Ernst, A Marte, F Schreck, J Schuster, and G Rempe. Bose-Einstein condensation in a pure Ioffe-Pritchard field configuration. *EPL (Europhysics Letters)*, 41(1):1, 1998.

[123] Piet O Schmidt, Sven Hensler, Jörg Werner, Thomas Binhammer, Axel Görlitz, and Tilman Pfau. Continuous loading of cold atoms into a Ioffe-Pritchard magnetic trap. *Journal of Optics B: Quantum and Semiclassical Optics*, 5(2):S170, 2003.

[124] DJ Han, RH Wynar, Ph Courteille, and DJ Heinzen. Bose-Einstein condensation of large numbers of atoms in a magnetic time-averaged orbiting potential trap. *Physical Review A*, 57(6):R4114, 1998.

[125] Robert Horne and Charles Sackett. Magnetic waveguide for atom interferometry and inertial navigation applications. *Bulletin of the American Physical Society*, 59, 2014.

[126] Toshiya Kinoshita, Trevor Wenger, and David S Weiss. All-optical Bose-Einstein condensation using a compressible crossed dipole trap. *Physical Review A*, 71(1):011602, 2005.

[127] Y-J Lin, AR Perry, RL Compton, IB Spielman, and JV Porto. Rapid production of ^{87}Rb Bose-Einstein condensates in a combined magnetic and optical potential. *Physical Review A*, 79(6):063631, 2009.

[128] DJ McCarron, HW Cho, DL Jenkin, MP Köppinger, and SL Cornish. Dual-species Bose-Einstein condensate of ^{87}Rb and ^{133}Cs. *Physical Review A*, 84(1):011603, 2011.

[129] Myoung-Sun Heo, Jae-yoon Choi, and Yong-il Shin. Fast production of large ^{23}Na Bose-Einstein condensates in an optically plugged magnetic quadrupole trap. *Physical Review A*, 83(1):013622, 2011.

[130] L. Humbert. All-optical Bose-Einstein condensate apparatus: Construction and operation, *Ph.D thesis, University of Queensland* 2012.

[131] Harald F Hess. Evaporative cooling of magnetically trapped and compressed spin-polarized hydrogen. *Physical Review B*, 34(5):3476, 1986.

[132] Immanuel Bloch, Jean Dalibard, and Wilhelm Zwerger. Many-body physics with ultracold gases. *Reviews of Modern Physics*, 80(3):885, 2008.

[133] W Ketterle, DS Durfee, and DM Stamper-Kurn. Making, probing and understanding Bose-Einstein condensates in Bose-Einstein condensation in atomic gases *pp. 67-176; cond-mat/9904034*, 1999.

[134] Satyendra Nath Bose. Plancks gesetz und lichtquantenhypothese. *Z. phys*, 26(3):178, 1924.

[135] Albert Einstein. *Quantentheorie des einatomigen idealen Gases.* Akademie der Wissenshaften, in Kommission bei W. de Gruyter, 1924.

[136] KM Mertes, JW Merrill, R Carretero-González, DJ Frantzeskakis, PG Kevrekidis, and DS Hall. Nonequilibrium dynamics and superfluid ring excitations in binary Bose-Einstein condensates. *Physical Review Letters*, 99(19):190402, 2007.

[137] DS Hall, MR Matthews, JR Ensher, CE Wieman, and EA Cornell. Dynamics of component separation in a binary mixture of Bose-Einstein condensates. *Physical Review Letters*, 81(8):1539, 1998.

[138] CJ Myatt, EA Burt, RW Ghrist, EA Cornell, and CE Wieman. Production of two overlapping Bose-Einstein condensates by sympathetic cooling. *Physical Review Letters*, 78(4):586, 1997.

[139] J Williams, R Walser, J Cooper, E Cornell, and M Holland. Nonlinear Josephson-type oscillations of a driven, two-component Bose-Einstein condensate. *Physical Review A*, 59(1):R31, 1999.

[140] David DeMille. Quantum computation with trapped polar molecules. *Physical Review Letters*, 88(6):067901, 2002.

[141] Hung-Wen Cho, Daniel J McCarron, Michael P Köppinger, Daniel L Jenkin, Kirsteen L Butler, Paul S Julienne, Caroline L Blackley, C Ruth Le Sueur, Jeremy M Hutson, and Simon L Cornish. Feshbach spectroscopy of an ultracold mixture of ^{85}Rb and ^{133}Cs. *Physical Review A*, 87(1):010703, 2013.

[142] Nicolas Schlosser, Georges Reymond, Igor Protsenko, and Philippe Grangier. Sub-poissonian loading of single atoms in a microscopic dipole trap. *Nature*, 411(6841):1024–1027, 2001.

[143] R Scheunemann, FS Cataliotti, TW Hänsch, and M Weitz. Resolving and addressing atoms in individual sites of a CO_2-laser optical lattice. *Physical Review A*, 62(5):051801, 2000.

[144] Jacob F Sherson, Christof Weitenberg, Manuel Endres, Marc Cheneau, Immanuel Bloch, and Stefan Kuhr. Single-atom-resolved fluorescence imaging of an atomic mott insulator. *Nature*, 467(7311):68–72, 2010.

[145] M Karski, L Förster, JM Choi, W Alt, A Widera, and D Meschede. Nearest-neighbor detection of atoms in a 1d optical lattice by fluorescence imaging. *Physical Review Letters*, 102(5):053001, 2009.

[146] CS Adams, M Sigel, and J Mlynek. Atom optics *Phys. Rep.*, 240:143, 1994.

[147] RJ Thompson, G Rempe, and HJ Kimble. Observation of normal-mode splitting for an atom in an optical cavity. *Physical Review Letters*, 68(8):1132, 1992.

[148] Paul D Lett, Richard N Watts, Christoph I Westbrook, William D Phillips, Phillip L Gould, and Harold J Metcalf. Observation of atoms laser cooled below the Doppler limit. *Physical Review Letters*, 61(2):169, 1988.

[149] ZT Lu, KL Corwin, MJ Renn, MH Anderson, EA Cornell, and CE Wieman. Low-velocity intense source of atoms from a magneto-optical trap. *Physical Review Letters*, 77(16):3331, 1996.

[150] K Dieckmann, RJC Spreeuw, M Weidemüller, and JTM Walraven. Two-dimensional magneto-optical trap as a source of slow atoms. *Physical Review A*, 58(5):3891, 1998.

[151] Matthew T Hummon, Mark Yeo, Benjamin K Stuhl, Alejandra L Collopy, Yong Xia, and Jun Ye. 2d magneto-optical trapping of diatomic molecules. *Physical Review Letters*, 110(14):143001, 2013.

[152] P Berthoud, E Fretel, and P Thomann. Bright, slow, and continuous beam of laser-cooled cesium atoms. *Physical Review A*, 60(6):R4241, 1999.

[153] Kai Dieckmann. Bose-Einstein condensation with high atom number in a deep magnetic trap, *Ph.D Thesis Van Der Waals-Zeeman Institute*, 2001.

[154] Harshit Lakhotia and Chiranjit Mitra. Saturated absorption spectroscopy. *Experiment University of Florida*

[155] Daryl W Preston, Carl E Wieman, and Kai M Siegbahn. Doppler free-saturated absorption spectroscopy: Laser spectroscopy. *Am. J. Phys*, 64(11):1432–1436, 1996.

[156] Robert Lorne Dugald Campbell. Thermodynamic properties of a Bose gas with tuneable interactions, 2011.

[157] LP Maguire, S Szilagyi, and RE Scholten. High performance laser shutter using a hard disk drive voice-coil actuator. *Review of scientific instruments*, 75(9):3077–3079, 2004.

[158] Nicholas McKay Parry, Mark Baker, Tyler Neely, Thomas Carey, Thomas Bell, and Halina Rubinsztein-Dunlop. Note: High turn density magnetic coils with improved low pressure water cooling for use in atom optics. *Review of Scientific Instruments*, 85(8):086103, 2014.

[159] T Bergeman, Gidon Erez, and Harold J Metcalf. Magnetostatic trapping fields for neutral atoms. *Physical Review A*, 35(4):1535, 1987.

[160] K Bessho, S Yamada, M Kooto, M Masahashi, and M Nakano. Characteristics of a multilayer eddy-current-type ac magnetic coil with a cooling system. *Journal of Applied Physics*, 64(10):6020–6022, 1988.

[161] J Leggett, S Crozier, and RW Bowtell. Actively shielded multi-layer gradient coil designs with improved cooling properties. *Journal of Magnetic Resonance*, 165(2):196–207, 2003.

[162] Lewis F Moody. Friction factors for pipe flow. *Trans. Asme*, 66(8):671–684, 1944.

[163] Leonardo Ricci, Luca Matteo Martini, Matteo Franchi, and Andrea Bertoldi. A current-carrying coil design with improved liquid cooling arrangement. *Review of Scientific Instruments*, 84(6):065115, 2013.

[164] Dylan O Sabulsky, Colin V Parker, Nathan D Gemelke, and Cheng Chin. Efficient continuous-duty bitter-type electromagnets for cold atom experiments. *Review of Scientific Instruments*, 84(10):104706, 2013.

[165] Markus Greiner, Immanuel Bloch, Theodor W Hänsch, and Tilman Esslinger. Magnetic transport of trapped cold atoms over a large distance. *Physical Review A*, 63(3):031401, 2001.

[166] A. Sharpe. *Transporting atoms using a magnetic coil transfer system.* PhD thesis, University of Colorado, Boulder, 2012.

[167] W Hänsel, J Reichel, P Hommelhoff, and TW Hänsch. Magnetic conveyor belt for transporting and merging trapped atom clouds. *Physical Review Letters*, 86(4):608, 2001.

[168] LLC Allegro MicroSystems. A primer on essentials of output voltage limitations. URL http://www.allegromicro.com/ /media/Files/Technical-Documents/an295011-Primer-On-Essentials-Of-Output-Voltage-Limitations.ashx?la=en

[169] Alex. Arduino Watchdog Circuit. URL http://www.playwitharduino.com/?p=291, 2011.

[170] Kurt E Gibble, Steven Kasapi, and Steven Chu. Improved magneto-optic trapping in a vapor cell. *Optics Letters*, 17(7):526–528, 1992.

[171] Wolfgang Petrich, Michael H Anderson, Jason R Ensher, and Eric A Cornell. Behavior of atoms in a compressed magneto-optical trap. *JOSA B*, 11(8):1332–1335, 1994.

[172] TL Gustavson, AP Chikkatur, AE Leanhardt, A Görlitz, Subhadeep Gupta, DE Pritchard, and Wolfgang Ketterle. Transport of Bose-Einstein condensates with optical tweezers. *Physical Review Letters*, 88(2):020401, 2001.

[173] Bruno Zimmermann, Torben Mueller, Jakob Meineke, Tilman Esslinger, and Henning Moritz. High-resolution imaging of ultracold Fermions in microscopically tailored optical potentials. *New Journal of Physics*, 13(4):043007, 2011.

[174] Heather J Lewandowski, DM Harber, Dwight L Whitaker, and EA Cornell. Simplified system for creating a Bose–Einstein condensate. *Journal of low temperature physics*, 132(5-6):309–367, 2003.

[175] C Klempt, T Henninger, O Topic, J Will, St Falke, W Ertmer, and J Arlt. Transport of a quantum degenerate heteronuclear Bose-Fermi mixture in a harmonic trap. *The European Physical Journal D-Atomic, Molecular, Optical and Plasma Physics*, 48(1):121–126, 2008.

[176] M. R. White. *Ultracold atoms in a disordered optical lattice.* PhD thesis, University of Illinois at Urbana-Champaign, 2009.

[177] Benjamin Sheard. *Magnetic transport and Bose-Einstein Condensation of Rubidium Atoms.* PhD thesis, University of Oxford, 2010.

[178] Kristina Meyer. An optical dipole trap for a two-species quantum degenerate gas, Ph.D Thesis Physikalisches Institut, Ruprecht-Karls-Universitat Heidelberg, 2010.

[179] M Pappa, PC Condylis, GO Konstantinidis, V Bolpasi, A Lazoudis, O Morizot, D Sahagun, M Baker, and W Von Klitzing. Ultra-sensitive atom imaging for matter-wave optics. *New Journal of Physics*, 13(11):115012, 2011.

[180] Kali E Wilson, Zachary L Newman, Joseph D Lowney, and Brian P Anderson. In situ imaging of vortices in Bose-Einstein condensates. *arXiv:1405.7745*, 2014.

[181] T Meyrath, F Schreck, J Hanssen, C Chuu, and M Raizen. A high frequency optical trap for atoms using hermite-gaussian beams. *Optics Express*, 13(8):2843–2851, 2005.

[182] NL Smith, WH Heathcote, G Hechenblaikner, E Nugent, and CJ Foot. Quasi-2d confinement of a bec in a combined optical and magnetic potential. *Journal of Physics B: Atomic, Molecular and Optical Physics*, 38(3):223, 2005.

[183] P Zupancic. *Dynamic Holography and Beamshaping using Digital Micromirror Devices.* PhD thesis, Master's thesis Ludwig-Maximilians-Universitat Munchen, 2013.

[184] Jinyang Liang, Rudolph N Kohn, Michael F Becker, and Daniel J Heinzen. Homogeneous one-dimensional optical lattice generation using a digital micromirror device-based high-precision beam shaper. *Journal of Micro/Nanolithography, MEMS, and MOEMS*, 11(2):023002–1, 2012.

[185] Jinyang Liang. High-precision laser beam shaping and image projection. Ph.D Thesis University of Texas 2012.

[186] Tiffany Harte, Graham D Bruce, Jonathan Keeling, and Donatella Cassettari. Conjugate gradient minimisation approach to generating holographic traps for ultracold atoms. *Optics express*, 22(22):26548–26558, 2014.

[187] Philipp M Preiss, Ruichao Ma, M Eric Tai, Alexander Lukin, Matthew Rispoli, Philip Zupancic, Yoav Lahini, Rajibul Islam, and Markus Greiner. Strongly correlated quantum walks in optical lattices. *arXiv:1409.3100*, 2014.

[188] Mark R Dennis, Robert P King, Barry Jack, Kevin O'Holleran, and Miles J Padgett. Isolated optical vortex knots. *Nature Physics*, 6(2):118–121, 2010.

[189] Ruichao Ma. Engineered potentials and dynamics of ultracold quantum gases under the micrscope, *Doctoral Dissertation, Harvard University*, 2014.

[190] Alexander L Gaunt, Tobias F Schmidutz, Igor Gotlibovych, Robert P Smith, and Zoran Hadzibabic. Bose-Einstein condensation of atoms in a uniform potential. *Physical Review Letters*, 110(20):200406, 2013.

[191] Tobias F Schmidutz, Igor Gotlibovych, Alexander L Gaunt, Robert P Smith, Nir Navon, and Zoran Hadzibabic. Quantum Joule-Thomson effect in a saturated homogeneous Bose gas. *Physical Review Letters*, 112(4):040403, 2014.

[192] AVT Cameras. *Prosilica GX-Series*, Retrieved from: `http://www.adept.net.au/cameras/avt/pdf/prosilicaGX1050-1050C.pdf`

[193] Texas instruments DMD 101: Introduction to digital Micromirror Device (DMD)

[194] Sumita Pennathur. *The MEMS Class. Introduction to MEMS and MEMS Design.* Retrieved from: `http://www.engr.ucsb.edu/~sumita/courses/Courses/ME141B/ME141B_lecture_9_F10.pdf`

[195] Olympus *Industrial Microscope - LMPLN-IR/LCPLN-IR*, Retrieved from: `http://www.olympus-ims.com/en/microscope/lmlcpln-ir/#!cms[tab]2Fmicroscope%2Flmlcpln-ir%2F50x`

[196] Texas Instruments *LUXBEAM 4600 DLP Driver Board*, Retrieved from : `http://www.ti.com/devnet/docs/catalog/endequipmentproductfolder.tsp?actionPerformed=productFolder&productId=16540`